

Martinos Center Summer Symposium Abstracts

GROUP 1 – Alzheimer's Disease



Reporting amyloid beta levels via bioluminescence imaging with amyloid reservoirs

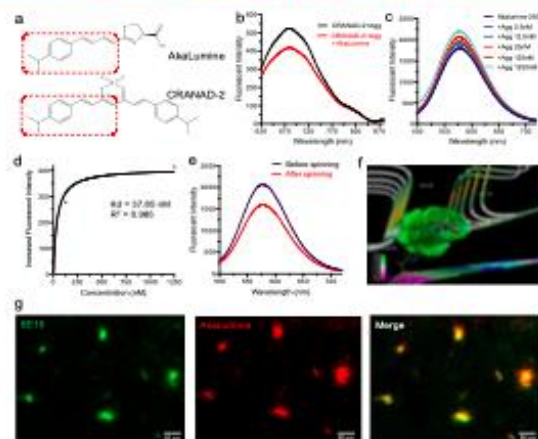
Jing Yang¹, Biyue Zhu¹, Weihua Ding², Shiqian Shen^{2*} and Chongzhao Ran^{1*}

¹Martinos Center for Biomedical Imaging, Massachusetts General Hospital and Harvard Medical School, Boston

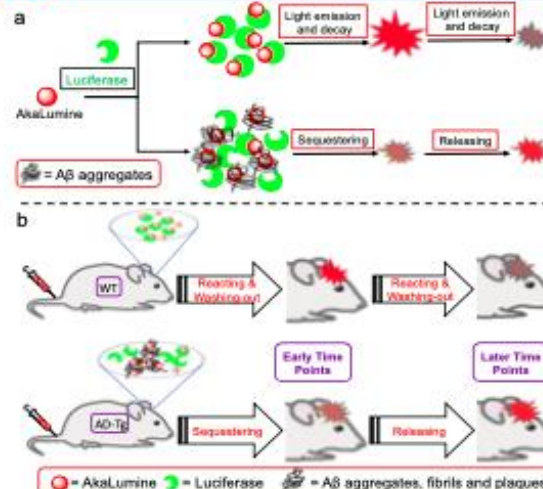
²MGH Center for Translational Pain Research, Massachusetts General Hospital and Harvard Medical School, Boston,

Background and Significance: Bioluminescence imaging has changed daily practice in preclinical research of cancers and other diseases in the last decades; however, it has been rarely applied in preclinical research of Alzheimer's disease (AD). In this report, we demonstrated that bioluminescence imaging could be used to report the levels of amyloid beta (Ab) species *in vivo*. We hypothesized that AkaLumine, a newly discovered substrate for luciferase, could bind to Ab aggregates and plaques. We further speculated that the Ab species have the reservoir capacity to sequester and release AkaLumine to control the bioluminescence intensity, which could be used to report the levels of Abs. Our hypotheses have been validated *via in vitro* tests, mimic phantom imaging, and *in vivo* imaging using transgenic AD mice that were virally transduced with aka Luciferase (AkaLuc). As expected, compared to the control group, we observed that the Ab group showed lower bioluminescence intensity due to AkaLumine sequestering at early time points, while higher intensity due to AkaLumine releasing at later time points.

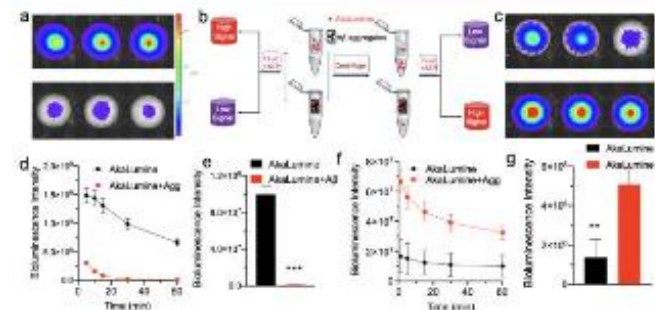
AkaLumine binds to Aβ aggregates and plaques



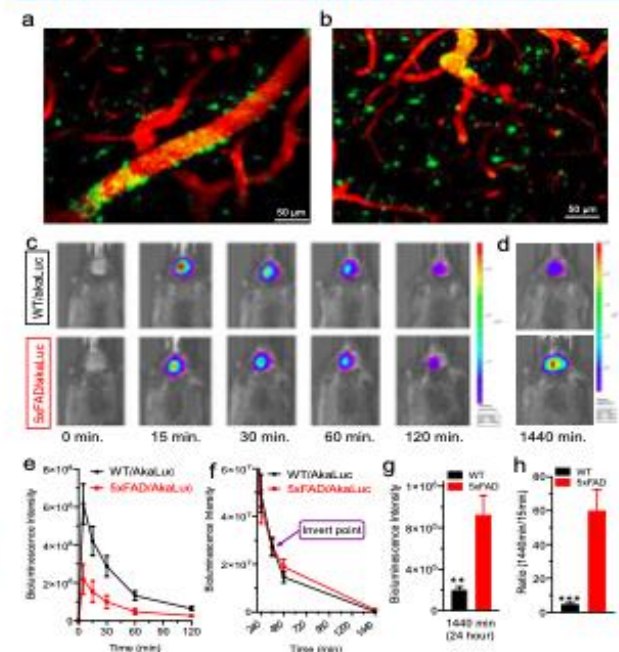
Principle of bioluminescence imaging with amyloid reservoir (BLIAR)



Validation of Aβ aggregates as reservoirs to sequester and release AkaLumine in solutions



In vivo two-photon microscopic fluorescence imaging and *in vivo* bioluminescence imaging with AkaLumine



Conclusion: In summary, we demonstrated the feasibility of bioluminescence imaging of Ab species *in vivo*. Our method can be easily adapted by regular biology laboratories. We believe that this method has the potential to change the daily practice of preclinical AD research and will greatly assist AD drug discovery and development.

Acknowledgment: This work was supported by NIH R01AG055413, and R21AG059134 awards (C.R.).



Monthly computerized at-home assessments to detect cognitive change in preclinical Alzheimer's disease



RJ Jutten, RE Amariglio, MJ Properzi, RF Buckley, P Maruff, CE Stark, MA Yassa, KA Johnson, RA Sperling, DM Rentz, KV Papp

Departments of Neurology and Radiology, Massachusetts General Hospital, Brigham and Women's Hospital, Harvard Medical School, Boston, MA, USA;
University of Melbourne, Australia; Cogstate Ltd, Australia; University of California, Irvine, CA, USA.

Introduction

Alongside the increased focus on characterizing Alzheimer's disease (AD) in the earliest, preclinical stage, there is a need to more rapidly detect and track the cognitive changes that may emerge during this stage. Computerized cognitive testing has the potential to achieve this by enabling standardized administration and data analyses allowing for remote, unsupervised, and more frequent assessments. Furthermore, the higher frequency assessments enable the study of practice effects (PE) that can occur with repeated assessments in older adults, and which previously has been shown to provide a meaningful cognitive marker in preclinical AD.^{1,2}

Study Aim

To investigate whether changes in performance over monthly cognitive assessments using an at-home administered computerized cognitive composite (C3) could aid in the detection of early AD-related cognitive changes in cognitively unimpaired (CU) individuals.

Methods

Participants

- N=114 CU individuals (age 77.1±4.9, 61% female, MMSE 29±1.3) from the Harvard Aging Brain Study (HABS) completed the self-administered C3 monthly at-home on an iPad for up to one year (11.7±2.8 months follow-up).
- All baseline participants had undergone PIB-PET imaging (1.25±1.05 years within at-home baseline) and Flortaucipir PET imaging (n=109, 0.56±0.4 years within at-home baseline) and in-clinic Preclinical Alzheimer's Cognitive Composite (PACC) testing.
- A subsample (n=72, age 78.1±5.2, 59% female, MMSE 29±1.3) also had one year follow-up in-clinic PACC testing available.

Computerized Cognitive Composite (C3)

- C3 includes the Face Name Associative Memory Exam (FNAME), the Behavioral Pattern Separation Task-Object version (BPSO), and the Cogstate Brief Battery including the One Card Learning (OCL).^{3,4}
- The FNAME, BPSO and OCL accuracy scores can be combined into a C3 memory composite.⁴

Statistical analyses

- Linear mixed models (LMM) to investigate C3 performance over time (months) adjusting for age, sex, and years of education, and to extract individual covariate-adjusted C3 slopes over first 3 months.
- Correlations to investigate associations between 3-month C3 slopes and 1) global amyloid burden (DVR); (2) tau deposition in the entorhinal cortex (SUVR, partial-volume corrected); and 3) change on the PACC over one year.
- Receiver Operating Curve (ROC) analyses to examine how accurately monthly C3 slopes could identify individuals who would show more than 0.10 standard deviation (SD) annual decline on the PACC.⁵

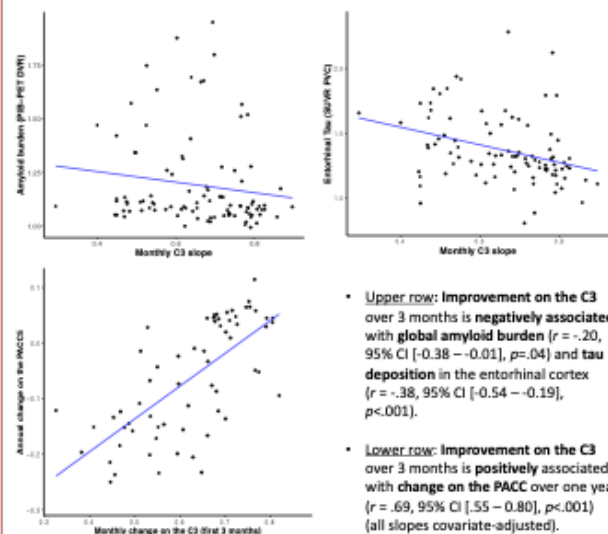
A. Individuals showed improved performance on all C3 measures. In general, slopes over 3 months were steeper than slopes over 1 year, suggesting stronger practice over initial repeated exposures.

TABLE 1. STANDARDIZED TIME ESTIMATES (SLOPES) OBTAINED FROM LMM

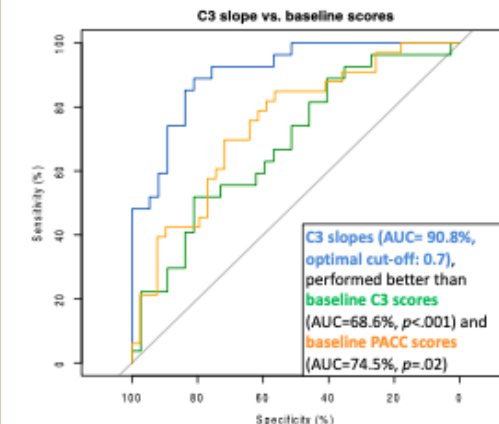
	Monthly change over 12 months			Monthly change over first 3 months		
	Time	95% CI	P-Value	Time	95%CI	P-Value
C3	0.226	0.207 – 0.245	<0.001	0.665	0.566 – 0.763	<0.001
BPSO	0.073	0.061 – 0.085	<0.001	0.21	0.148 – 0.271	<0.001
FNAME	0.098	0.088 – 0.108	<0.001	0.378	0.328 – 0.429	<0.001
OCL	0.051	0.041 – 0.060	<0.001	0.074	0.021 – 0.127	0.006

*Time estimates obtained from LMM adjusting for age, sex and years of education. All scores are z-transformed to facilitate comparisons across measures and follow-up durations. C3 = memory composite z-score combining BPSO + FNAME + OCL scores.

B. Less improvement over 3 months is associated with greater AD biomarker burden and annual decline on the PACC.



C. 3-month C3 slopes show good discriminative ability to identify > 0.10 SD annual decline on the PACC.



Conclusions

- Overall, CU adults show practice effects (PE) on monthly repeated computerized testing, and PE seemed stronger over initial repeated exposures (i.e., over the first 3 months).
- However, diminished PE over 3 months are associated with greater AD biomarker burden and cognitive decline over one year.
- Characterizing PE on the C3 over 3 months could provide a valuable marker to identify individuals who will show more than 0.10 SD annual decline on the PACC.

Our findings imply that unsupervised computerized testing using monthly retest paradigms may provide an examination of lack of practice as a more nuanced way of assessing cognitive change. This could aid in more rapid detection of individuals at risk for cognitive decline, which may facilitate AD secondary prevention trials.

References

- Jutten et al. Alzheimer's & Dementia: DADM, 12 (1) (2020).
- Samaroo et al. Alzheimer's and Dementia: DADM, 12 (1) (2021).
- Rentz et al. The Journal of Prevention of Alzheimer's Disease, 3(1), 8–12 (2016).
- Papp et al. The Journal of Prevention of Alzheimer's Disease, 8, 59–67 (2021).
- Petersen et al. Annals of Neurology, 89 (6), 1145–1156 (2021).

Contact: rjutten@mgh.harvard.edu | @RoosJutten



Extraneous neuroimaging factors do not explain sex differences in flortaucipir-PET signal: examination of skull binding and partial volume effects

N C Edwards*, M R Scott*, M J Properzi, H L Jacobs, J C Price, L K Manning, D V Mayblum, Z B Rubinstein, D M Rentz, K A Johnson, R A Sperling, A P Schultz, R F Buckley

Departments of Neurology and Radiology, Massachusetts General Hospital, Harvard Medical School, Brigham and Women's Hospital, Boston, MA, USA



Introduction

Clinically normal (CN) females exhibit greater ¹⁸F-flortaucipir (FTP) PET signal than males in both temporal and neocortices^{1,2}. It remains unclear whether sex differences across the neocortex are primarily explained by PET-related technical variability. We aimed to investigate the contribution of signal spillover/off-target skull binding³ to sex differences in FTP-PET. Next, we explored partial volume effects (PVE) by simulating sex differences in smoothed FTP-PET signal⁴. Discerning sex differences in tau signal versus noise is pivotal to understanding sex differences in the pathology of Alzheimer's disease and associated tauopathies.

Methods

Participants: 398 older adults (CN=343; mild cognitive impairment=55) from the Harvard Aging Brain Study (HABS; n=251) and Alzheimer's Disease Neuroimaging Initiative (ADNI; n=147).

PET: Tau accumulation was measured using FTP-PET imaging. FTP-PET was expressed using standardized uptake value ratios (SUVrs) using a cerebellar grey reference region. ROIs were defined as bilateral averages using FreeSurfer v6.0. PET data were non-partial volume corrected (PVC). Skull analyses utilized 28 cortical ROIs, and PVE analyses utilized 45 cortical and subcortical ROIs.

Skull Segmentation:

- For each participant, a skull mask was created using FreeSurfer-defined 'skull' and 'head extracerebral' regions.
- For each skull voxel, all the gray matter voxels were found within a 12mm radius.
- Skull tau ROIs values were created by calculating mean FTP signal of voxels within this radius across each proximal FreeSurfer ROI.

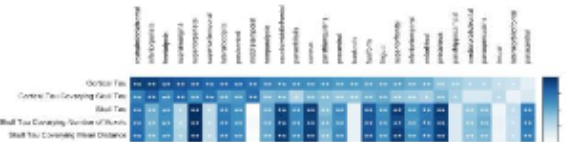
PVE:

- Extract bilateral SUVrs for each image and calculate group-level means for each region.
- Assign group-level regional means to each participant's FreeSurfer segmentation.
- Convolve each image with a 6x6x6 mm Gaussian kernel.
- Recalculate SUVrs across ROIs.

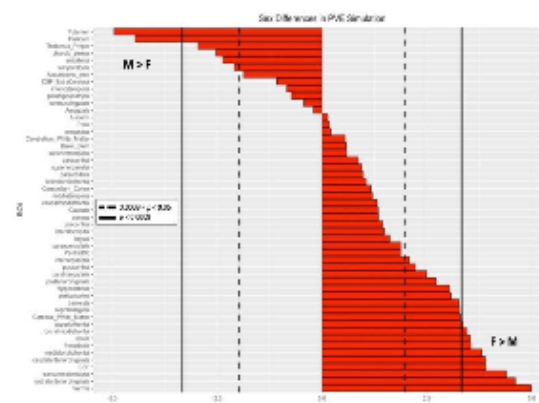
Statistical analyses: Linear regression models were used to examine sex differences across ROIs, while adjusting for age and cohort. Correction for multiple comparisons was implemented using Bonferroni correction.

Sex differences exist in skull FTP-PET signal, but do not impact cortical findings

(Row 1) Effects of sex on cortical tau. (Row 2) Effects of sex on cortical tau, covarying skull tau. (Row 3) Effects of sex on skull tau. (Row 4) Effects of sex on skull tau, covarying number of voxels. (Row 5) Effects of sex on skull tau, covarying mean gray matter-to-skull distance. (All) T-values of sex effects are reported, and elements are coded by significance. Positive t-values indicate higher FTP signal in females than males. STS = superior temporal sulcus.



Simulated FTP-PET partial volume effects tend to be female-directed



T-values from regressions of the form $PVE = \text{sex} + \text{covariates}$. Dotted lines indicate thresholds of uncorrected $p=0.05$ and solid lines indicate Bonferroni corrected thresholds of $p=0.0009$. Positive t-values indicate higher FTP signal in females than males.

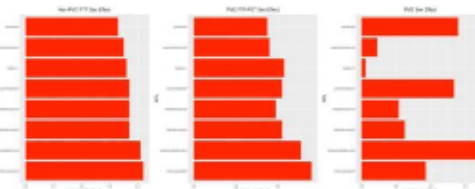
	M	F	Tau Statistic	p
N (% subjects)	220	178		
ΔPVE: 1-4 Isolines	58 (26.4)	37 (20.8)	$\chi^2 = 1.68$	0.19
ΔPVE: 4-4 Isolines	6 (2.7)	8 (4.5)	$\chi^2 = 0.91$	0.34
High ΔPVE	74 (33.6)	55 (19.5)	$\chi^2 = 0.34$	0.56
Global CDR 0.5	31 (14.1)	49 (22.5)	$\chi^2 = 4.72$	0.03*
Mean (SD)				
Age at FTP-PET image (years)	73.8 (6.7)	73.7 (6.8)	$t(346) = -3.19$	0.002*
PICC (score)	0.41 (0.7)	0.18 (0.7)	$t(346) = 3.39$	0.0008*
Education (years)	15.9 (2.8)	16.5 (2.9)	$t(346) = -2.12$	0.03*

Demographic Information

Group comparisons of the sexes were conducted using two-sample *t*-tests and chi-squared test. **p* < .05

Sex-specific partial volume effects do not systematically impact sex differences in cortical FTP-PET signal

Standardized betas of sex effects in cortical FTP-PET relative to the estimated sex-specific PVE. Regions showed exhibited the eight strongest sex differences in cortical FTP-PET. Positive betas indicate higher FTP-PET signal in females than males. For instance, where PVC inflates the sex difference in FTP-PET signal in a region (e.g., inferior parietal), this is not systematically impacted by PVEs.



Conclusions

Our findings suggest that sex differences in FTP-PET are largely not attributed to skull 'clouding' or sex-specific partial volume effects. There is growing support for a biological sex effect contributing to sex differences in tau-PET signal. While we found evidence of potential methodological bias that could explain some sex effects, there remains female-directed tau-PET differences. Studies now need to further examine the biological mechanisms that may explain female vulnerability to tauopathy.

Investigations of sex differences in longitudinal tau accumulation, (a few preliminary reports already suggest faster rates in females) will add further support to the argument that noise properties inherent in FTP-PET do not significantly contribute to sex differences in cortical tau signal.

References:

- [1] Buckley et al., JAMA Neurology. 2019.
 - [2] Buckley et al., Annals of Neurology. 2020.
 - [3] Scott et al., Neurology: Clinical. 2021.
 - [4] Gross et al., NeuroImage. 2016.
- Funding:** Dr. Buckley is funded by an NIH grant (K99AG061238) and the Women's Brain Initiative Pilot Project. Funding from the Brigham and Women's Hospital. This work also was supported with funding from the National Institute of Health, including P01AG056643 (Sperling), P01AG056643 (Sperling), P01AG056643 (Sperling), P01AG056643 (Sperling), P01AG056643 (Sperling). This work was carried out in part at the Alzheimer's A. Martinez Center for Functional Imaging at the Massachusetts General Hospital, using resources provided by the Center for Functional Neuroimaging Technologies, P41NS045996, a P41 Biotechnology Resource Grant supported by the National Institute of Biomedical Imaging and Bioengineering (NIBIB), National Institutes of Health. This work also involved the use of instrumentation supported by the NIH Shared Instrumentation Grant Program and/or High-End Instrumentation Grant Program; specifically, grant numbers S10RR021110, S10RR023400, and S10RR023043.
- Results:** M R Scott rcs02@bwh.harvard.edu; R F Buckley rfbuckley@bgh.harvard.edu; N C Edwards ncwoods@bgh.harvard.edu

3D MR Spectroscopic Imaging Reveals Links Between Brain Metabolites and Multidimensional Pain Features in Fibromyalgia Patients

Jeungchan Lee (JLEE196@mgh.harvard.edu),¹ Ovidiu C. Andronesi,¹ Angel Torrado-Carvajal,^{1,2} Eva-Maria Ratai,¹ Marco L. Loggia,¹ Akila Weerasekera,¹ Michael P. Berry,¹ Laura Isaro,³ Asimina Lazaridou,³ Myrella Paschali,³ Arvina Grahl,¹ Ajay D. Wasan,⁴ Robert R. Edwards,³ Vitaly Napadow^{1,3}

¹ Department of Radiology, Athinoula A. Martinos Center for Biomedical Imaging, Massachusetts General Hospital, Harvard Medical School, Charlestown, MA, USA

² Medical Image Analysis and Biometry Laboratory, Universidad Rey Juan Carlos, Madrid, Spain

³ Department of Anesthesiology, Perioperative and Pain Medicine, Brigham and Women's Hospital, Harvard Medical School, Boston, MA, USA

⁴ Department of Anesthesiology and Perioperative Medicine, Center for Innovation in Pain Care, University of Pittsburgh, Pittsburgh, PA, USA



INTRODUCTION

- Fibromyalgia is a multidimensional chronic pain syndrome.
- The mechanism of the central nervous system dysfunction is not fully understood.
- Voxel-wise 3D MR Spectroscopic Imaging (MRSI) was applied to investigate the relationship between brain metabolite levels and multidimensional clinical/behavioral variables (e.g., pain catastrophizing, clinical pain severity, evoked pain sensitivity).

METHODS

Patients

- 87 female FM patients (40.7 ± 12.2 years)

Clinical/behavioral variables

- Pain Catastrophizing Scale (PCS): a measure of negative cognitive/affective responses to pain
- Brief Pain Inventory (BPI, severity): clinical pain intensity
- Cuff P40 pressure (mmHg, 40/100 pain intensity, 0=no pain, 100=worst pain): evoked pain sensitivity

MRSI data acquisition

- 3.0 T scanner (Skyra, Siemens) with 32-channel head coil
- custom-developed pulse sequence¹ using localized adiabatic spin-echo refocusing (LASER) excitation and spiral encoding (TR/TE = 1500/30 ms, FOV = 240 × 240, reconstructed voxel size = 7.5 mm isotropic, spectral window = 1250 Hz, number of average = 2, acquisition time = 3:42)
- volume of interest (VOI) covers bilateral insula, cingulate cortex, and thalamus

Data processing and analysis

- estimation of metabolite concentration: LCModel (version 6.3-1L)
 - total Cr (tCr, combined creatine and phosphocreatine) for normalization, Glx (combined glutamate and glutamine), mIino (myo-inositol), and total NAA (tNAA, combined N-acetylaspartate and N-acetylaspartylglutamate)

'adequate'- vs 'low'-quality data voxel

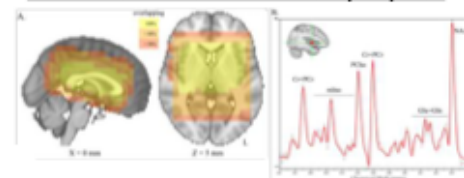
- signal-to-noise ratio (SNR), full width at half maximum (FWHM), Cramer-Rao lower bounds (CRLB)
 - SNR ≥ 5 , FWHM < 0.1 ppm, and CRLB $< 20\%$: 'adequate'-quality
 - SNR < 5 , FWHM ≥ 0.1 ppm, or CRLB $\geq 20\%$: 'low'-quality → data restoration using inpainting²

Group analysis: voxel-wise multiple linear regression

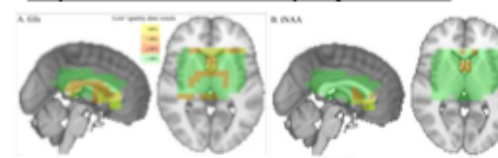
- co-registration of normalized, inpainted metabolite maps to MNI (7.5 mm isotropic) space (FNIRT, FSL)
- linear regression analysis between metabolites (Glx, mIino, and tNAA) and clinical/behavioral variables
 - controlled: age, medication (gabapentin/pregabalin), average tCr level (correlated with PCS and BPI)
- mixed effect model with Ordinary Least Square (OLS, FEAT, FSL)
- 3 criteria for significance (each voxel):
 - absolute Z ≥ 2.3 ,
 - percentage of inpainted data (patient) $< 60\%$,
 - P < 0.05 for correlation only using 'adequate'-quality data

RESULTS

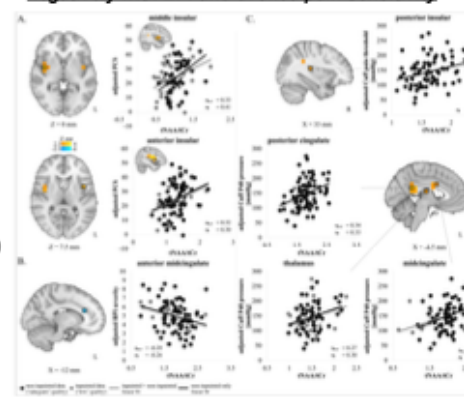
1. MRSI data collection: VOI and sample spectra



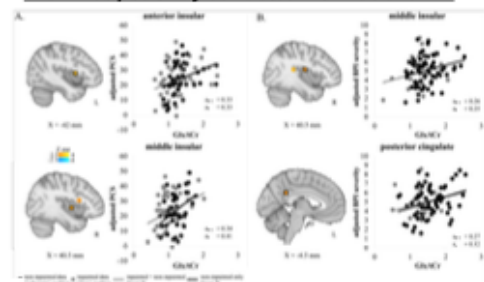
2. Spatial distribution of 'low'-quality data voxels



4. tNAA was positively correlated with PCS, and negatively with BPI and evoked pain sensitivity



3. Glx was positively correlated with PCS and BPI



CONCLUSIONS

- These findings support single-voxel placement targeting nociceptive processing area in previous ¹H-MRS studies.
- Results also highlight the role of PCC, self-referential cognitive processing area³, as important for chronic pain pathophysiology.
- 3D MRSI could reduce the burden of lengthy scan time for clinical research.

REFERENCE

- Andronesi et al. Neurologic 3d mr spectroscopic imaging with low-power adiabatic pulses and fast spiral acquisition. Radiology 2012;262:647-61.
- Torrado-Carvajal et al. Inpainting as a technique for estimation of missing voxels in brain imaging. Ann Biomed Eng 2020.
- Lee et al. Encoding of self-referential pain catastrophizing in the posterior cingulate cortex in fibromyalgia. Arthritis Rheumatol 2018;70:1308-18.

Research funding: This work was funded by the NIH (R01-AK084387, R01-AK050505, R01-MH123-AT000206, P30-NS045093, P41-MH015013, R01-MH022170, R01-MH022045). Development of MRSI pulse sequence and processing was funded by NIH/NICHD (R01-HD070308, R01-HD070309).

Conflict of interest: none

Use of dual PET-MR neuroimaging to study potentially overlapping mechanisms in Long-COVID and ME/CFS

Hannah Bues¹, Eva Ratai², Donna Felsenstein³, Darin Dougherty¹, Michael VanElzakker¹

¹Division of Neurotherapeutics, Martinos Center for Biomedical Imaging, Massachusetts General Hospital at Charlestown

² Department of Radiology, Martinos Center for Biomedical Imaging, Massachusetts General Hospital at Charlestown

³ Department of Infectious Diseases, Massachusetts General Hospital

Background

- A subset of acute infectious illness patients will develop long-term symptoms. Diagnoses are either
 - Infection-based: "post-Ebola syndrome," and "post-Zika syndrome" (1).
 - Symptom-based: myalgic encephalomyelitis/chronic fatigue syndrome (ME/CFS)
- As a result of the pandemic, a new patient group with long-term symptoms has emerged: Long-COVID or PASC patients**

Peripheral inflammation due to acute infection leads to proinflammatory cytokines being

- Actively transported across the blood brain barrier
- Passively diffused through the blood brain barrier
- Detected by chemoreceptors in the afferent vagus nerve
 - "Sickness Response" and "Mirror Response"

→ Possible mechanism of long-term symptoms: Dysregulation in peripheral immune system to nervous system inflammation pathways (2)

- Long-COVID symptoms overlap significantly with ME/CFS (3).
- As ME/CFS researchers, we have added Long-COVID recruitment to our existing ME/CFS neuroinflammation study.

Figure 1: Symptom Categories of the International Consensus Criteria (ICC), the diagnostic criteria for ME/CFS

ICC Symptom Categories	
Post exertional neuroimmune exhaustion	physical or cognitive fatigability, post-exertional symptom exacerbation, post-exertional exhaustion, prolonged recovery periods from exertion, lack of stamina
Neurological impairments	neurocognitive impairments, pain, sleep disturbance, neurosensory, perceptual, and motor disturbances
Immune, gastro-intestinal and genitourinary impairments	flu-like symptoms, susceptibility to viral infections, GI tract disturbances, genitourinary disturbances, sensitivities
Energy production/ transportation impairments	cardiovascular symptoms, respiratory symptoms, endocrine symptoms

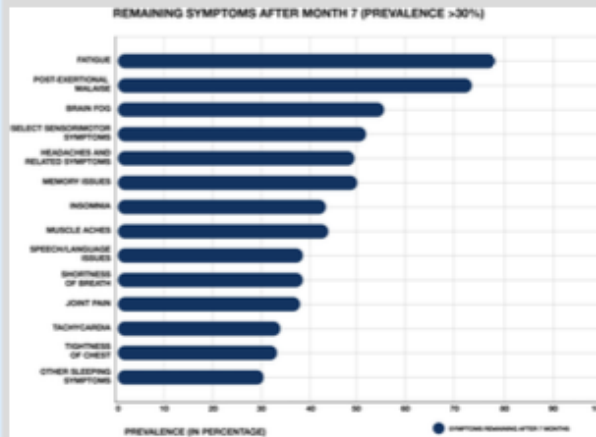


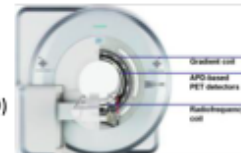
Figure 2: Most common symptoms remaining after 7 months in 966 respondents from a cohort of suspected and confirmed COVID-19 cases obtained via an international web-based survey. (In Proal & VanElzakker 2021 (1), adapted from Davis et al. 2020 (4))

Methods

For this study, we are using a dual PET-MR scanner. Dual PET-MR scanning affords the ability to take advantage of the PET and MR techniques' complementary qualities.

PET

- Radioligand: PBR28
 - Binds to translocator protein (TSPO) which is upregulated during microglial activation, and thus utilized as a dependent measure in neuroinflammation studies
- Biologically sensitive
 - Specific to the biological process of interest, in this case TSPO upregulation



MRI - Magnetic Resonance Spectroscopy (MRS)

Simultaneous to the PET scanning, we also acquire MR data, including magnetic resonance spectroscopy (MRS).

- Spatial resolution
- Chemical changes beyond microglial activation

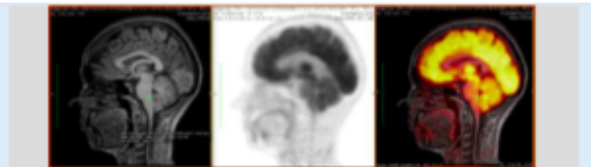


Figure 3: Pilot data from a FDG PET study conducted by our group.

Hypotheses

Long-COVID and ME/CFS patients:

- Will share pathophysiological mechanisms and biomarkers.
- Will show increased PBR28 uptake in the central nervous system relative to controls, particularly in structures associated with the subjective sickness response such as dorsal brainstem, caudate nucleus, insular cortex, and dorsal anterior cingulate cortex.
- Will show altered MRS signal for metabolites related to microglia activation and metabolic dysfunction relative to controls.

Conclusion

- Altered PET and MRS signal could serve as evidence to support the presence of neuroinflammation in these illnesses.
- Adding Long-COVID recruitment to our existing ME/CFS neuroinflammation study will serve to better understand the mechanisms behind the development of long-term symptoms after acute infectious illness.

Future Directions

- The Multisource Interference Task (MSIT)
 - Disruption of the dorsal anterior cingulate cortex (dACC) could be a mechanism of ME/CFS patients' "brain fog" symptoms
 - We expect to see increased BOLD response and PBR28 uptake in the dACC in ME/CFS patients vs. controls.
 - Considering that brain fog is a common symptom of Long-COVID as well, we could expect to see increased BOLD response and PBR28 uptake in this patient group as well.
- Validation of MRS by PET would allow greater use of the more broadly available MRS technique in these conditions.

Citations

- Proal AD & VanElzakker MB (2021) Long COVID or Post-acute Sequela of COVID-19 (PASC): An Overview of Biological Factors That May Contribute to Persistent Symptoms. *Front. Microbiol.* 12:659269.
- VanElzakker MB, Brantley-Sieden L & Lane ME (2019) Neuroinflammation and Cytokines in Myalgic Encephalomyelitis/Chronic Fatigue Syndrome (ME/CFS): A Critical Review of Research Methods. *Front. Neurol.* 9:3832.
- Komaroff AL & Balkem L (2021) How COVID-19 Lead to Myalgic Encephalomyelitis/Chronic Fatigue Syndrome? *Front. Med.* 7:698524.
- Ozovo, H. C. et al. (2020) Characterizing long COVID in an international cohort: 7 months of symptoms and their impact. *medRxiv*(Preprint)

Altered post-meal resting-state functional brain connectivity between nucleus tractus solitarii and cortical networks in functional dyspepsia is linked to antral motility

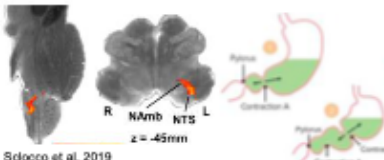
Harrison Fisher¹, Roberta Scicco^{1,2}, Rowan Staley^{1,2}, Kyungsun Han³, April Mendez², Christopher Nguyen^{4,5}, Braden Kuo², Vitaly Napadow¹

¹Department of Radiology, Athinoula A. Martinos Center for Biomedical Imaging, Massachusetts General Hospital, Harvard Medical School, Charlestown, MA, USA. ²Department of Gastroenterology and Center for Neurointestinal Health, General Hospital, Harvard Medical School, Boston, MA, USA. ³Korean Institute of Oriental Medicine, Daejeon, Korea. ⁴Cardiovascular Research Center, Massachusetts General Hospital, Charlestown, MA, USA. ⁵Department of Medicine, Harvard Medical School, Charlestown, MA, USA



INTRODUCTION

- Functional dyspepsia (FD) patients experience upper gastrointestinal (GI) symptoms possibly related to gastric motor or sensory dysfunction
- Gastric rhythmic contraction (peristalsis) is modulated by the vagus nerve
- Afferent mechanosensor signals from the GI tract are conducted by the vagus nerve and can directly modulate feeding behaviors
- The nucleus tractus solitarii (NTS) afference from the stomach, projects to higher brainstem and cortical/subcortical regions
- Cortico-brainstem processing of GI mechanical sensations may be important for functional GI disorders



METHODS: Study Design

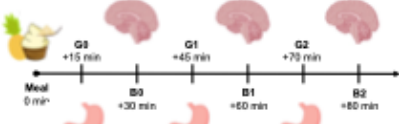
Subjects

- FD patients enrolled based on ROME IV diagnostic criteria
- Healthy controls (HC) without gastric issues

Group	N	N Female	Age	BMI
FD	15	13	29.1 +/- 13.2 yrs	24.0 +/- 3.9 kg/m ²
HC	14	9	31.3 +/- 8.1 yrs	24.8 +/- 3.6 kg/m ²

Experimental Protocol

- Subjects consume their max tolerable amount of a 470ml pineapple pudding meal (which provides contrast agent)
- Stomach scans collected +15, +45, +70 minutes post meal
- Brain scans collected +30, +60, +80 minutes post meal



METHODS: Brain Data

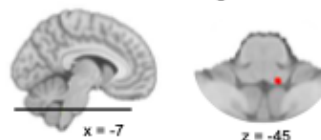
- 3T Siemens Trio scanner with a 64-channel head coil
- Anatomical volume (multi-echo MPRAGE, 1mm³ voxels)
 - 6-minutes of BOLD fMRI data (SMS, acceleration = 5, TR/TE = 1270/33ms, 2.04 x 2.04 x 2.00mm, 288 vols)

BOLD Data Processing

- Preprocessing: RETROICOR, fMRIprep, skull stripping
- Denoise (afni 3dTproject): Realignment pars, high motion timepoints (FD > 0.5mm), aCompCor, RVHCorr, high pass filter [0.008 Hz], 5mm FWHM smoothing

Seed - Whole Brain Functional Connectivity (FC) Maps

- Left NTS used as seed region for all subjects

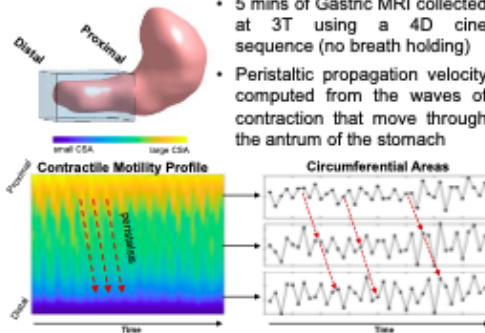


Statistical Analysis

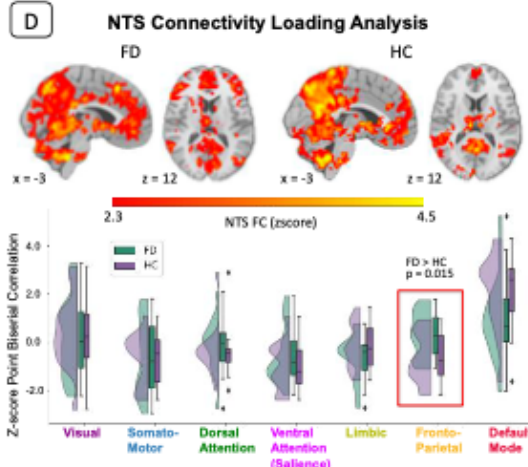
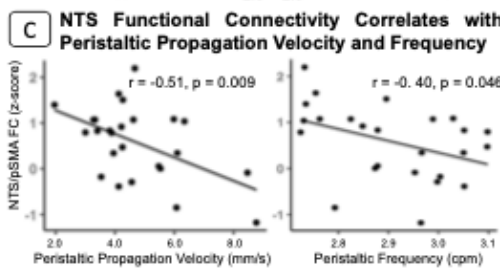
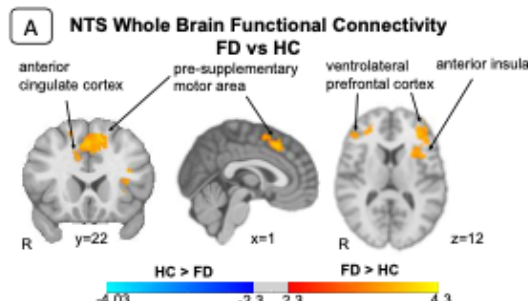
- FC maps combined across scans for each subject
- subject level maps assessed with point biserial correlations for similarity to Resting State Networks (Yeo et al, 2011)
- FD vs HC functional connectivity maps thresholded
 - (z > 2.3, cluster corrected p-FWE < 0.05)

METHODS: Stomach Data

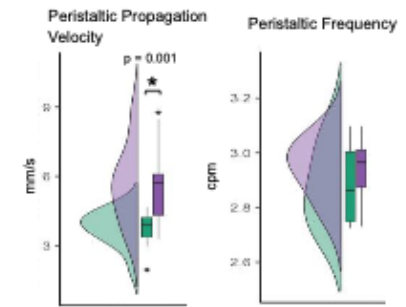
Scicco et al, 2021



RESULTS



B FD Patients Show Lower Average Peristaltic Propagation Velocity



DISCUSSION

- Compared to HCs, FD patients display higher functional connectivity of the NTS (A) and lower peristaltic propagation velocity (B).
- Peristaltic propagation velocity and frequency are correlated with NTS functional connectivity (C)
- NTS FC pattern (D) loads onto the default mode network predominantly in both groups, but the loading onto the frontoparietal network is significantly greater in FD patients
- thus, differences in brain functional connectivity may be related to visceral mechanoreceptor signaling from altered gastric functional properties in FD patients

References

- Bai L, Mungarndale S, Ramesh KS, Haig EL, Liu Y, Gray LA, Miller T, Chen Y, Miller J, Jones RS, Madlener L, Zeng H, Kwanewell MA, Krueger ZA (2019) Gastroesophageal Motility in Visceral Sensory Neurons That Control Feeding. *J Neurosci* 39:1123-1143.
- Scicco R, Garcia RA, Radl, Kaderlik NW, Isenburg K, Fisher H, Hubbard CS, Ay I, Peltzman JR, Grishman J, Makris N, Teicher N, Barber R, Napadow V (2019) The influence of respiration on brainstem and corticovagal responses to auricular vagus nerve stimulation: A multimodal ultra-high-field (7T) fMRI study. *Brain Stimul* 12: 911-919.
- Scicco R, Nguyen C, Staley R, Fisher H, Mendez A, Velas C, Kaderlik NW, Haig E, Miller J, Jones RS, Madlener L, Zeng H, Kwanewell MA, Krueger ZA (2019) Gastroesophageal Motility in Visceral Sensory Neurons That Control Feeding. *J Neurosci* 39:1123-1143.
- Yeo BT, Krienen FM, Sepulcre J, Sabuncu MR, Lusk J, Lee JJ, Reissland N, Reissland JL, Sneller JW, Zolle L, Peltzman JR, Fisher H, Liu H, Buckner RL (2011) The organization of the human cerebral cortex estimated by intrinsic functional connectivity. *Journal of neurophysiology* 105:1125-1195.
- Funding: NIH R01-GM123867, NIH R21-OK119029, NIH R21-EB024701

Linking day-to-day fluctuations in chronic pain to neural correlates of pain anticipation and clinical outcomes of cognitive behavioral therapy

M. Barton-Zuckerman¹, A. Grahl¹, A. Lazaridou², M. Paschali², J. Lee¹, M. Berry¹, L. Isaro¹, A. Anzolin¹, K. Isenburg¹, R. Edwards^{2,*}, V. Napadow^{1,2,*}

¹Martinos Center for Biomedical Imaging, Massachusetts General Hospital, Charlestown, MA, USA. ²Department of Anesthesiology, Brigham and Women's Hospital, Boston, MA, USA.



Background

- Greater day-to-day variability in clinical pain predicts better outcomes following treatment interventions
- Prior studies found that patients reporting greater fluctuations in pain at baseline experienced greater placebo effects^{1,2} and were more likely to be considered responders in drug trials³
- Characterization of baseline chronic pain is necessary to evaluate these potential influences on clinical outcomes
- Cognitive behavioral therapy (CBT) targets pain catastrophizing, a common feature in chronic pain that has been associated with increased pain severity and disability
- Aim:** Identify associations between clinical outcomes & neural nociceptive processing in fibromyalgia patients completing a CBT vs. pain education (EDU) Intervention, focusing on the influence of day-to-day pain variability

Methods

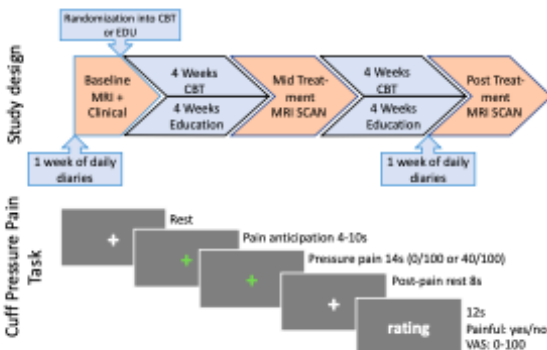
N=78 female fibromyalgia (FM) patients, mean age ($\pm SD$) 41.27 ± 12.54
Daily Diaries: Daily questionnaire assessing average FM pain intensity [0-100 scale] → min. 5/7 baseline daily diaries completed before scan

Clinical Outcome Measures: Pain Catastrophizing Scale (PCS) & Brief Pain Inventory (BPI) with severity (BPI-S) and interference subscales (BPI-I)

Cuff Pressure Pain Task (left leg): two intensities individually calibrated (3 trials each), non-painful (0/100) and moderately painful (40/100)

Cuff pain fMRI: 3.0 T Siemens Skyra: SMS MB (acc. factor 5, TR=1250 ms, TE=33 ms, 2 mm³, 98x98x75, 284 vol)

Analysis: RETROICOR using AFNI 3dretroicor, motion correction (MCFLIRT), fieldmap, smoothing (5mm FWHM) & high-pass temporal filtering (90s), EPI-T1-MNI152 registration (FSL-BBR register, FSL-FLIRT, FSL-FNIRT), → GLM pain anticipation: FSL-FLAME1+2 cluster corr., p<0.05, z>2.3, motion parameters, log SD average daily pain rating as covariate (pain day-to-day variability)

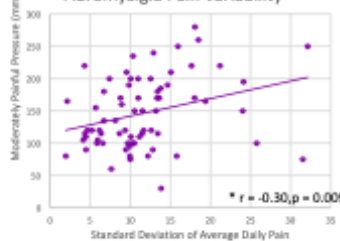


Results: Pain Variability & Experimental Pain

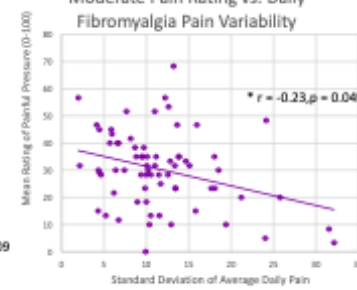
N = 70

- Mean of Average Daily Pain over 5-7 days: (mean \pm SD, 0-100 NRS) 65.35 ± 14.16
- Standard Deviation of Average Daily Pain over 5-7 days: (mean \pm SD) 11.60 ± 6.15
- Moderately painful cuff pressure: (mean \pm SD) $146.9 \text{ mmHg} \pm 55.05 \text{ mmHg}$
- Mean Rating of moderately painful cuff pressure: (mean \pm SD) 30.29 ± 13.89
- 8 subjects excluded due to missing or low-quality pressure pain task fMRI data

Moderately Painful Cuff Pressure (40/100 pain) vs. Daily Fibromyalgia Pain Variability

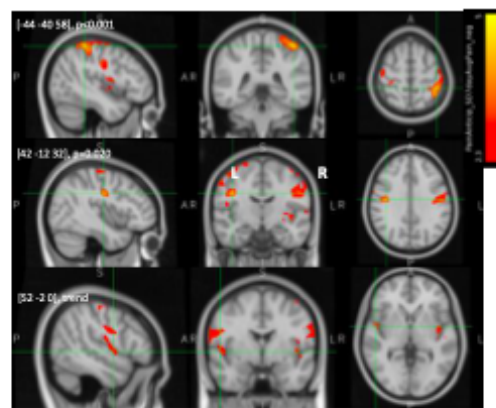


Moderate Pain Rating vs. Daily Fibromyalgia Pain Variability



Results: fMRI (exploratory)

Negative correlation of baseline day-to-day variability & fMRI response to cuff pain anticipation



Higher day-to-day FM pain fluctuations over 7 days prior to scan associated with lower BOLD fMRI response during pain anticipation in nociception-processing areas

Summary

- Greater day-to-day variability in baseline fibromyalgia pain was associated with greater post-therapy improvement in pain catastrophizing after CBT but not EDU
- Greater day-to-day variability in baseline pain was also associated with reduced hyperalgesia (i.e. lower evoked pressure pain ratings)
- Lower mean baseline pain levels were associated with decreased improvement on BPI after treatment
- In an exploratory BOLD fMRI analysis, higher day-to-day FM baseline pain variability was related to lower fMRI activation in nociception-processing brain regions during pressure pain anticipation → higher baseline pain fluctuation beneficial for neural response to pain cues

References:

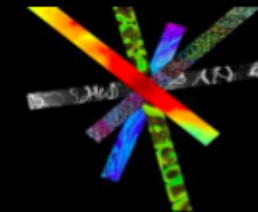
- Kaptchuk, T.J., Harmond, C. C., & Miller, T. G. (2020). Placebos in chronic pain: Evidence, theory, and use in clinical practice. *The BMJ*, 370. <https://doi.org/10.1136/bmj.m1668>
- Harris, R. E., Williams, D. A., McLean, S. A., Sen, A., Helford, M., Gentile, R. M., Gracely, R. H., & Clewett, D. J. (2005). Characterization and consequences of pain variability in individuals with fibromyalgia. *Arthritis and Rheumatism*, 52(11), 3670-3674. <https://doi.org/10.1002/art.23407>

Characterization of Demyelinating Lesions in Multiple Sclerosis Using Highly Accelerated 3D Wave-CAIPI Susceptibility-Weighted Imaging and FLAIR

Nicole Grinspan; Augusto Lio M Goncalves Filho, MD^{1,2}; Azadeh Tabari, MD^{1,2}; Chanon Ngamsombat²; Ilona George, MD³; Stephen F Cauley, PhD^{1,2}; Wei Liu, PhD⁴; Daniel N Splithoff, PhD⁵; Wei-Ching Lo⁶, PhD; Pamela W Schaefer, MD¹; Otto Rapalino, MD¹; Eric C Klawitter, MD²; John Conklin, MD^{1,2}; Susie Y Huang, MD, PhD^{1,2}

1. Department of Radiology, Massachusetts General Hospital (MGH), Boston, MA, United States
2. Athinoula A. Martinos Center for Biomedical Imaging, Charlestown, MA, United States
3. Department of Neurology, Massachusetts General Hospital (MGH), Boston, MA, United States

4. Siemens Shenzhen Magnetic Resonance Ltd., Shenzhen, China
5. Siemens Healthineers, Erlangen, Germany
6. Siemens Medical Solutions Inc., Boston, MA, United States



Athenaia A.
Martinos
Center
for Biomedical Imaging
MASSACHUSETTS
GENERAL HOSPITAL
HARVARD
MEDICAL SCHOOL
MIT
Massachusetts
Institute of
Technology

Introduction

Magnetic resonance imaging (MRI) is widely used to characterize demyelinating lesions in the brain and establish an earlier diagnosis of multiple sclerosis (MS). Previous studies have suggested that the central vein sign (CVS) is specific for multiple sclerosis (MS) and that paramagnetic rims seen in chronic active MS plaques are associated with more aggressive disease. A major barrier to the more widespread use and assessment of these imaging signs is the long acquisition time associated with the high-resolution FLAIR and susceptibility-based MRI sequences used to identify the CVS and paramagnetic rim sign. The goal of this study was to assess the frequency of paramagnetic rims and CVS using highly accelerated 3D Wave-CAIPI susceptibility-weighted imaging (Wave-SWI) and FLAIR (Wave-FLAIR) sequences for the adjunct characterization of demyelinating lesions in MS within clinically feasible scan times.

Methods

This study was approved by the IRB and was HIPAA compliant. 78 consecutive patients undergoing brain MRI for the clinical evaluation of demyelinating disease from June–October 2020 were scanned on 3T MRI systems (MAGNETOM Prisma and Vida, Siemens Healthcare, Erlangen, Germany). The imaging protocol included accelerated prototype 3D Wave-SWI (acceleration factor [R]=6, acquisition time [TA]=1:58min, 0.8x0.8x1.8mm) and 3D Wave-FLAIR (R=4, TA=2:30min, 1x1x1mm) sequences. Taken together with other sequences used in the protocol (Table 1), the Wave-FLAIR and Wave-SWI sequences helped to shorten the clinical MS protocol from 30 min to <20 min. Each patient's Wave-FLAIR and Wave-SWI images were co-registered using built-in 3D registration software within the PACS (Visage). Two neuroradiologists (9 and 13 years of experience) blinded to clinical diagnosis independently reviewed the co-registered image series and determined the number of lesions with paramagnetic rims and/or CVS. Discrepancies between raters were discussed, and consensus was reached on the number of lesions with paramagnetic rims and CVS per case. We calculated the proportion of confirmed MS or clinically isolated syndrome (CIS) patients with paramagnetic rim lesions and/or CVS. We also assessed the agreement between raters in their independent review.

Results

Of the 78 patients evaluated, 55 patients (71%) had confirmed MS by the 2017 McDonald criteria, 9 had clinically isolated syndrome (CIS) (12%), and the remaining 14 had a non-MS diagnosis (18%). Of the 64 patients with MS or CIS, paramagnetic rims were identified in 27 cases (42%) (Fig.1). 47 cases had at least one lesion with CVS (73%). There was substantial agreement between raters in the visualization of paramagnetic rims before consensus (91.03% - Cohen k = 0.79, p < 0.01). No paramagnetic rims or CVS were identified in non-MS patients (Fig.2).

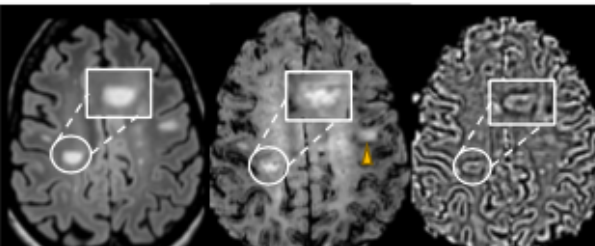


Fig.1. Axial Wave-SPACE-FLAIR (left), Wave-SWI (middle), and phase images (right) in a patient with confirmed MS showing the presence of paramagnetic rims corresponding to lesions visible on FLAIR (highlighted). A lesion with a central vein sign can be seen in the same Wave-SWI sequence (arrowhead).

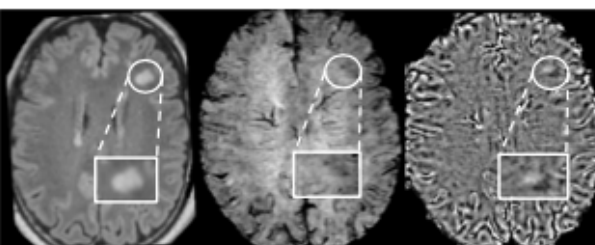


Fig.2. Axial Wave-SPACE-FLAIR (left), Wave-SWI (middle), and phase images (right) in a patient with confirmed anti-MOG disease with no visible paramagnetic rim around the lesion visible on FLAIR (highlighted). No lesions with a central vein sign were identified on Wave-FLAIR and Wave-SWI.

Discussion

The frequencies of paramagnetic rims and CVS identified on highly accelerated 3D Wave-SWI and Wave-FLAIR sequences in our cohort were comparable to those reported by other groups using longer sequences with standard image encoding techniques. MRI-pathologic correlation studies have reported that paramagnetic rims on susceptibility-based MRI identify a subset of MS lesions with compartmentalized inflammation at the lesion boundary and associated failure of remyelination. Considering that T2/FLAIR images alone are unable to separate chronic active lesions from inactive stable demyelination, SWI may help in distinguishing them. Moreover, the paramagnetic rims that are seen in chronic active MS plaques are associated with more aggressive disease and can aid in the identification of persistent perilesional inflammation. Our findings suggest that it is feasible to implement a clinical MS MRI protocol with Wave-SWI and Wave-FLAIR sequences to provide additional information in the characterization of demyelinating lesions, thereby improving confidence in the diagnosis of MS and assessment of disease progression. The use of Wave-CAIPI accelerated images enable a more comprehensive protocol to be performed within 20 minutes of total acquisition time, without compromising exam throughput and patient comfort. The future adoption of susceptibility-weighted imaging in MS protocols may also prove to be a promising tool for more detailed assessment of disease activity and stratification of patients for neuroprotective therapy.

Table 1. Optimized MRI protocol with Wave-CAIPI

Sequence	Slice Thick	Accel. Factor (R)	Acquisition Time (TA)
Pre-contrast Wave-T1 MPAGE	1.0 mm	R = 4	2:20 min
Wave-SWI	1.8 mm	R = 6	1:49 min
Diffusion Weighted Imaging (DWI)	5.0 mm	R = 2	1:00 min
Wave-T2 SPACE	1.0 mm	R = 6	1:46 min
Wave-SPACE FLAIR	1.0 mm	R = 4	2:30 min
Post-contrast Wave-T1 MPAGE	1.0 mm	R = 4	2:20 min
		Total	10:53 min

Table 2. Demographic distribution

Sex (Female / male)	54 / 24
Mean Age ± SD (yr.)	41 ± 15
Clinical Diagnosis (%)	
Multiple Sclerosis (MS)	55 (71%)
Clinically Isolated Syndrome	9 (12%)
Non-MS	14 (18%)

References:

- Clarke MA, et al. AJNR. 2020;41(6):1001-1008.
Absinta M, et al. JAMA Neurol. 2019;76(12):1474-1483.

Acknowledgment: Supported by a research grant from Siemens Healthineers

GROUP 3 – Behavioral/Cognitive Testing



Intimate-Partner Violence Related Brain Injury Among Colombian Women

Nathalia Quiroga², María Camila Navarro², Carlos José De los Reyes³, Annie-Lori Joseph & Eve Valera^{3,4,5}
Universidad De La Costa¹; Universidad Del Sisú²; Universidad Del Norte³; Department of Psychiatry, Massachusetts General Hospital, Boston, MA⁴
Department of Psychiatry, Harvard Medical School, Boston, MA⁵



Introduction

Intimate partner violence (IPV) has been defined as any type of behavior within an intimate relationship that results in physical, psychological, or sexual harm to one of its members.¹

Many studies have shown that IPV negatively impacts women survivor's health, and additionally when compared to women who have not experienced partner abuse, female survivors present with lower performance across domains of memory and learning, attention, inhibitory control, working memory, executive functioning language, and overall cognitive functioning²⁻⁶.

Researchers have suggested that many of the difficulties that survivors report may be due to brain injuries (BI) sustained during partner abuse.

Unfortunately, information on IPV-related BI and its associated sequelae outside of North America is scant.

Aim

To assess the prevalence of IPV-related BI in a sample of Colombian women who have experienced IPV and examine the relationship between BI and cognitive performance and psychological symptoms.

Methods

- Seventy women from the city of Barranquilla, Colombia who suffered any form of intimate-partner violence

Instruments

Computerized EMBRACED neuropsychological battery

- Learning, working and long-term memory, cognitive flexibility, and processing speed

Brain Injury Severity Assessment (BISA)

 - A semi-structured interview that examines history of any partner- or non-partner-related alteration in consciousness. For example: "After anything that your partner has ever done to you, have you ever lost consciousness or blacked out?" [If Yes] Can you please describe what happened?

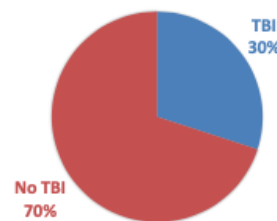
Patient Health Questionnaire-9

- To assess depressive symptoms
 - Generalized Anxiety Disorder-7**
 - To assess symptoms of anxiety
 - PTSD Checklist-5**
 - To assess posttraumatic stress symptoms

- Spearman's rank correlations were performed to examine the relationship between BI and cognitive variables and psychological symptoms.
 - Bivariate partial correlations were performed to control severity of violence and posttraumatic stress symptoms

Results

Prevalence of TBI



BI was negatively associated with measures of long-term memory, working memory, and cognitive flexibility

The relationship between BI with long-term memory and working memory remained when controlling for abuse severity

The relationship between BI and long-term memory was only slightly attenuated when controlling for posttraumatic stress and remained with working memory.

Discussion

- Nearly one out of every three women interviewed sustained a partner-related BI
 - Higher brain injury scores were associated with poorer long-term memory, working memory, and cognitive flexibility.
 - BI scores were not associated with our measures of psychopathology with the exception of a relationship trend with depression that was attenuated when controlling for partner abuse severity.

References

- ## References

Investigating the impact of the Coronavirus Pandemic in Children with PANS/PANDAS

Julia Zagaroli, Kyle Williams MD, PhD., Saffron Homayoun Mirza, MBChB., Sarah O'Dor, PhD

Background

- Pediatric Autoimmune Neuropsychiatric Disorders Associated with Streptococcal Infections (PANDAS) and Pediatric Autoimmune Neuropsychiatric Syndrome (PANS) refer to the acute presentation of neuropsychiatric syndrome in children, including obsessive-compulsive disorders (OCD)
- OCD symptoms in adults and children have worsened as an effect of the novel coronavirus (COVID-19) pandemic^{1,2}, as well as worsening anxiety and depression symptoms in children.²
- The aim of this study was to assess the impact of the pandemic on
 - the severity of PANS/PANDAS symptoms
 - the ability to access care for PANS/PANDAS symptoms
 - the level of perceived stress on children with PANS/PANDAS and their families
- Hypothesis: Parents will report increased severity of PANDAS/PANS symptoms during the pandemic, as well as increased family stress and caregiver burden.

Methods

- Recruitment: PANDAS Network and patients of the Pediatric Neuropsychiatry and Immunology Program
- Inclusion Criteria: parents/caregivers who self-endorsed as having a child with suspected/diagnosed PANS/PANDAS
- N = 221 surveys
- Caregiver demographics: 20-67 years old ($M=45.89, SD=7.25$)
- Patient demographics: 3-17 years ($M=11.69 SD=3.43$); 131 (59%) Male, 87 (39%) female, and 3 (2%) transgender/fluid
- Patient diagnoses: PANS (N = 125); PANDAS (N = 176)
- Measures:
 - COVID Questionnaire (QC)* - assessed families direct contact with coronavirus, changes in symptoms, treatment accessibility, and perceived stress and distress related to the pandemic
 - Children's Yale-Brown Obsessive Compulsive Scale (CY-BOCS-PR)*
 - Caregiver Burden Inventory (CBI)*

Table 1. PANS/PANDAS Symptoms During Pandemic

	N (%)
Patient experienced PANS/PANDAS symptoms	198 (89.6%)
Average PANS/PANDAS symptom severity	
Mild	90 (45%)
Moderate	80 (36.9%)
Severe	9 (2.1%)
Patients with suspected/diagnosed COVID-19	45 (20.4%)
Exacerbated following COVID-19 infection:	
Obsessive-Compulsive symptoms	17 (37.8%)
Tic symptoms	12 (26.7%)
Anxiety symptoms	22 (48.9%)
Depression symptoms	10 (22.2%)
"Pandemic had negative effects on PANS/PANDAS"	100 (45.7%)
"More stressful atmosphere at home than average"	179 (81.8%)
Pandemic Negatively Affected:	
Patient's relationship with friends	134 (61.5%)
Patient's participation in hobbies	150 (68.5%)
Patient's academic skills	107 (48.6%)
Treatment during pandemic	
Received care for PANS/PANDAS	155 (70.5%)
Telemedicine care for PANS/PANDAS	129 (83%)
Preferred in person to telemedicine	95 (44.2%)
Telehealth allowed easier access to care	105 (81.4%)

Table 2. Standardized Questionnaires

Questionnaire	M (SD)	Description
Patient OCD Severity (CY-BOCS-PR)	16.9 (SD= 8.6)	Moderate
Caregiver Burden (CBI)	29.56 (SD=20.2)	Moderate

For more information, contact Julia Zagaroli (JZagaroli@mgh.harvard.edu)

Behav2. Zagaroli

Table 3. Outlook on COVID-19 Vaccine for Patient

Vaccine status	N (%)
Plan to vaccinate for covid	69 (30.4%)
Do not plan to vaccinate for covid	58 (25.6%)
Unsure	94 (43.7%)

Discussion

- Children with PANS/PANDAS continue to experience symptoms during the pandemic, with over a third experiencing moderate to severe symptoms.
- Caregivers endorsed children had overall better access to care due to the offering of telehealth; however, many still preferred in-person visits
- The apprehension to vaccinate this population is important for providers to acknowledge and address during treatment, as this could have implications on public health.
- Children who had a COVID infection reported symptom exacerbations following their infection. This is important given the hypothesis that further inflammation related to autoimmune reactions will exacerbate symptoms of PANS/PANDAS.
- Our findings are consistent with literature in other neuropsychiatric disorders suggesting during the pandemic, symptoms of PANS/PANDAS were increased along with overall stress within the family.
- Our hypotheses proved correct; child distress, relationships, and symptoms of PANS/PANDAS were negatively impacted, and family stress and burden increased
- Further research could examine factors that mitigate pandemic related stress, and whether this impacts PANS/PANDAS symptoms. Additionally, the relationships between symptom exacerbation and vaccines could be examined further to alleviate caregiver uncertainty of vaccination.

References

- Tanir, Y. et al. Exacerbation of obsessive compulsive disorder symptoms in children and adolescents during COVID-19 pandemic. *Psychiatry Res.* **293**, 113363 (2020).
- Nissen, J. B., Holgaard, D. & Thomsen, P. H. The immediate effect of COVID-19 pandemic on children and adolescents with obsessive compulsive disorder. *BMC Psychiatry* **20**, 1–10 (2020).



Fine Motor Weaknesses in Children with PANDAS

Massachusetts General Hospital: Pediatric Neuropsychiatry and Immunology Program
Mary A Hamel, Sarah O'Dor, PhD, Kyle Williams, MD, PhD

MASSACHUSETTS GENERAL HOSPITAL
HARVARD MEDICAL SCHOOL
MIT Massachusetts Institute of Technology

Background

- Pediatric Autoimmune Neuropsychiatric Disorder Associated with Streptococcal infections (PANDAS): rapid onset of Obsessive-Compulsive Disorder (OCD) and/or tics in children after a Group A Streptococcal infection
 - hypothesized to result from an autoimmune reaction in which anti-streptococcal antibodies attack the basal ganglia, leading to inflammation
- Fine motor weakness (handwriting deterioration) has been reported in 36% to 73% of children with PANDAS^{1,2}
- Fine motor weakness can manifest as difficulty with handwriting, personal grooming, and body control. This can negatively affect scholastic performance and activities of daily life, leading to lower self-esteem^{3,4}
- Objective: to evaluate the frequency and severity of fine motor deficiencies in children with PANDAS



Figure 1: The left picture was drawn by a 7-year-old male diagnosed with PANDAS one week prior to symptom onset; the right, 2 months after symptom onset.

Methods

- Eighty-nine children who presented for initial evaluations at the Massachusetts General Hospital Pediatric Neuropsychiatry and Immunology program and met criteria for PANDAS were evaluated for fine motor dexterity using the Grooved Pegboard Test
- The test involved inserting 25 grooved pegs into randomly-oriented notched holes on a board. Participants completed the test with both their dominant and non-dominant hands
- Raw times were converted to z-scores using norms developed by Wang et al. (2011). There are norms for dominant and non-dominant hands in different age brackets⁵

Results

- The mean z-scores for children with PANDAS on the Grooved Pegboard Test were -0.803 ($SD=1.32$) and -0.7040 ($SD=1.38$) for dominant ($n=89$) and non-dominant ($n=86$) hands, respectively. Both means are significantly lower than the age norms (dominant hand: $t(88)=-5.715$, $p=0.00$; non-dominant hand: $t(85)=-4.721$, $p=0.00$).

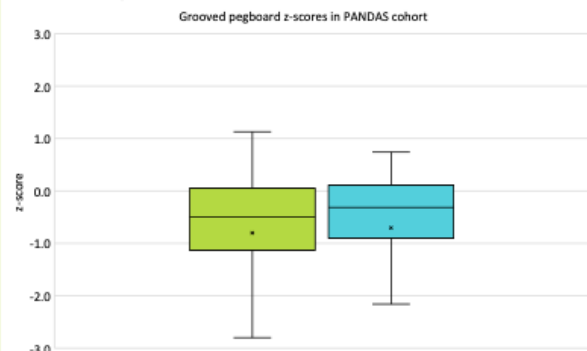


Figure 2: Z-scores for dominant (green) and non-dominant (blue) hands of the PANDAS cohort on the Grooved Pegboard Test. The X's denote the mean scores.

Discussion

- Children with PANDAS performed poorly on the Grooved Pegboard Test, scoring, on average, nearly 1 deviation below the general population for both dominant and non-dominant hands. This suggests prevalent and severe fine motor weaknesses in the PANDAS population
- It is difficult to quantitatively evaluate whether children experienced motor deterioration after PANDAS symptom onset or, rather, had longstanding motor challenges
- Further research must evaluate whether the fine motor weaknesses observed in children with PANDAS are specific to the PANDAS presentation or indicative of ASD, ADHD, or another commonly comorbid disorder. Alternately, there may be common mechanisms underlying PANDAS and other neuropsychiatric disorders, leading to similar symptom presentations
- Further research should evaluate whether motor weakness extends to gross motor skills

Conclusion

- Fine motor weakness can affect children's performance in academic and everyday activities. Children with PANDAS should be screened for motor disorders so that they may receive any necessary therapy.

References

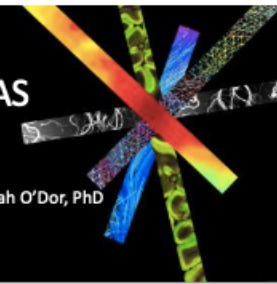
- ¹Swedo, S. E., Leonard, H. L., Garvey, M., Mittleman, B., Allen, A. J., Perlmutter, S., Lougee, L., Dow, S., Zamkoff, J., & Dubbert, B. K. (1998). Pediatric autoimmune neuropsychiatric disorders associated with streptococcal infections: clinical description of the first 50 cases. *The American journal of psychiatry*, 155(2), 264–271. <https://doi.org/10.1176/jnp.155.2.264>
- ²Calaprice, D., Tora, J., Parker-Athill, E. C., & Murphy, T. K. (2017). A Survey of Pediatric Acute-Onset Neuropsychiatric Syndrome Characteristics and Course. *Journal of child and adolescent psychopharmacology*, 27(7), 607–618. <https://doi.org/10.1089/jcap.2016.0105>
- ³Wang, T. N., Tseng, M. H., Wilson, B. N., & Hu, F. C. (2009). Functional performance of children with developmental coordination disorder at home and at school. *Developmental medicine and child neurology*, 51(10), 817–825. <https://doi.org/10.1111/j.1469-8749.2009.03271.x>
- ⁴Miller, L. T., Missiuna, C. A., Macnab, J. J., Malloy-Miller, T., & Polatajko, H. J. (2001). Clinical description of children with developmental coordination disorder. *Canadian journal of occupational therapy*. *Revue canadienne d'ergothérapie*, 68(1), 5–15. <https://doi.org/10.1177/000841740106800101>
- ⁵Wang, Y. C., Magasi, S. R., Bohannon, R. W., Reuben, D. B., McCreat, H. E., Bubela, D. I., Gershon, R. C., & Rymar, W. Z. (2011). Assessing dexterity function: a comparison of two alternatives for the NIH Toolbox. *Journal of hand therapy: official journal of the American Society of Hand Therapists*, 24(4), 313–321. <https://doi.org/10.1016/j.jht.2011.05.001>

For more information, please contact Mary (Maggie) Hamel at mahamel@mgh.harvard.edu

Vaccine Hesitancy in Caregivers of Children with PANS/PANDAS

Massachusetts General Hospital: Pediatric Neuropsychiatry and Immunology Program

Rebecca Belisle, Julia S Zagaroli, BA, Olivia M Downer, BS, Mary A Hamel, Saffron Homayoun, MBChB, Kyle Williams, MD, PhD, Sarah O'Dor, PhD



Athena A.
Martinos
Center
For Biomedical Imaging

MASSACHUSETTS
GENERAL HOSPITAL

HARVARD
MEDICAL SCHOOL

MIT
Massachusetts Institute of
Technology

Background

- Pediatric Acute-onset Neuropsychiatric Syndrome (PANS):
 - the acute onset of either Obsessive-Compulsive Disorder (OCD) or avoidant restrictive food intake disorder (ARFID) with accompanying cognitive, behavioral, or neurological symptoms
- Pediatric Autoimmune Neuropsychiatric Disorder Associated with Streptococcal Infections (PANDAS):
 - an acute and dramatic onset of OCD or tic symptoms following a Group A Streptococcal
- ~75-90% of the population needs to be vaccinated against COVID-19 to achieve herd immunity¹
- Vaccine hesitancy has been shown to be related to age, political affiliation, and general immunization status^{2,3,4}
- Underlying anxiety-related & neurodevelopmental disorders are associated with an increased risk of hospitalization for pediatric COVID-19⁵
- Study Objectives:
 - Examine vaccine hesitancy among a vulnerable pediatric population
 - Generate a predictive model for vaccine hesitancy

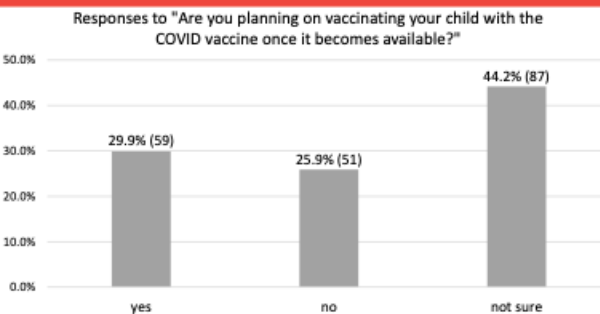
Methods

- Recruitment: PANDAS network and patients of the Pediatric Neuropsychiatry and Immunology Program at MGH who had expressed interest in research
- REDCap survey from March to June 2021 of 254 individuals who self-identified as primary caregivers of children with suspected/diagnosed PANS/PANDAS
- N = 81 for the binary logistic regression
- Included demographic, pandemic-related, and vaccine-related questions
- Used SPSS forced-entry binary logistic regression to generate models of vaccine hesitancy
 - Continuous IVs: age of respondent, presidential voting outcomes for 2020 election within respondent's zip code/county
 - Categorical IV: child's immunization status (up to date/not up to date)
 - DV: planning to vaccinate child against COVID-19 (predicting likelihood of NOT planning to vaccinate)

References

- Chevallier, C., Hacquin, A.-S., & Mercier, H. (2021). COVID-19 vaccine hesitancy: Shortening the last mile. *Trends in Cognitive Sciences*, 25(5), 331–333. <https://doi.org/10.1016/j.tics.2021.02.002>
- Fridman, A., Gershon, R., & Gneezy, A. (2021). COVID-19 and vaccine Hesitancy: A longitudinal study. *PLOS ONE*, 16(4). <https://doi.org/10.1371/journal.pone.0250123>
- KFF covid-19 vaccine monitor dashboard. Kaiser Family Foundation. (2021, July 13). <https://www.kff.org/coronavirus-covid-19/dashboard/kff-covid-19-vaccine-monitor-dashboard/>.
- Shih, S.-F., Wagner, A. L., Masters, N. B., Prosser, L. A., Lu, Y., & Zikmund-Fisher, B. J. (2021). Vaccine hesitancy and rejection of a vaccine for the novel coronavirus in the United States. *Frontiers in Immunology*, 12. <https://doi.org/10.3389/fimmu.2021.558270>
- Kompaniets, L., Agathis, N. T., Nelson, J. M., et al. (2021). Underlying medical conditions associated with severe COVID-19 illness among children. *JAMA Network Open*, 4(6), 1-14. <https://doi.org/10.1001/jamanetworkopen.2021.11182>

Figure 1. Responses to COVID-19 vaccine question



Overall Model Statistics

- Accuracy: 75.3%
- Pseudo R² (Nagelkerke): 0.332
- Omnibus Tests of Model Coefficients:
 - $\chi^2 = 22.797$
 - df = 3
 - p = 0.000045

Table 1. Odds Ratios & p-values for IVs

Table 1. Odds Ratios and p-values for the Independent Variables in a Logistic Regression Model for COVID-19 Vaccine Hesitancy among Caregivers of Children with PANS/PANDAS

Independent Variable	Odds ratio	p-value
Age of respondent	0.927	0.0819
Presidential voting pattern by zip code/county	25.350	0.0374
Child up to date on immunizations	0.117	0.0007

- An odds ratio greater than 1 indicates the variable is a positive predictor of unwillingness to vaccinate against COVID-19.
- An odds ratio less than 1 indicates the variable is a negative predictor of unwillingness to vaccinate against COVID-19.

Results

- 25.9% of primary caregivers of children with PANS/PANDAS said they are not planning to vaccinate their child against COVID-19
- The logistic regression overall performed significantly better than the null model ($p < 0.05$)
- Caregivers of children with PANS/PANDAS were more likely to say that they would not vaccinate their child again COVID-19 once a vaccine became available if:
 - They resided in an area with a greater proportion of people who voted Republican in the '20 presidential election AND
 - Their child was not up-to-date on immunizations
- Age of the respondent was not a significant predictor in this model

Discussion

- This model can inform which segments of the population are not planning to vaccinate their children again COVID-19 once it becomes available.
- The model suggests that general vaccine hesitancy may underlie COVID-19 vaccine hesitancy in some cases, suggesting there may still be a misinformation issue regarding vaccine safety.
- This information can be used to direct vaccination campaigns to specific populations.
- Further research should evaluate reasons for vaccine hesitancy in caregivers of PANS/PANDAS as well as the safety of the COVID-19 vaccine in the PANS/PANDAS population.

Contact

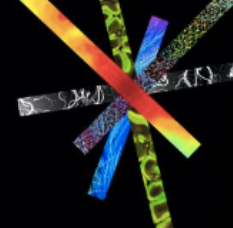
For more information, contact Becky Belisle at rbelisle@mgh.harvard.edu



PIMI
PRECISION INTERVENTIONAL AND MEDICAL
IMAGING RESEARCH GROUP

An Interpretable Machine Learning-based Risk Model of Contrast-Induced Nephropathy in Patients Undergoing Lower Extremity Endovascular Interventions

Meredith Cox, Nicholas Reid, J.C. Panagides, Jayashree Kalpathy-Cramer, Dania Daye
Department of Radiology, Massachusetts General Hospital



Annex A
Martinos Center
for Biomedical Imaging
MASSACHUSETTS GENERAL HOSPITAL
HARVARD MEDICAL SCHOOL
MIT Massachusetts Institute of Technology

Background

Contrast-induced nephropathy (CIN) is a postprocedural complication that may prolong hospital stay and contribute to increased morbidity and mortality.¹ Identification of patient cohorts at higher risk of contrast-induced nephropathy may allow targeted interventions to reduce the incidence of renal injury. We aimed to develop an interpretable machine learning model to stratify risk for acute renal failure in patients undergoing lower extremity endovascular interventions for peripheral artery disease (PAD).

Dataset

Using the American College of Surgeons National Surgical Quality Improvement Program Database (ACS-NSQIP), we extracted 14,444 patients who underwent lower extremity endovascular procedures for PAD between 2011 and 2018.

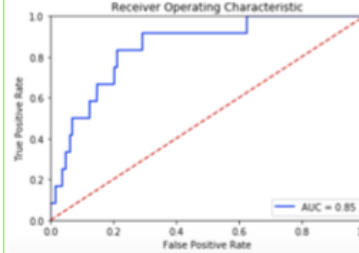
Feature	LEE Dataset
Age (mean(SD))	69.1 (11.4)
Male (%)	59
Female (%)	41
ASA > 3 (%)	89.5
Diabetes (%)	53.3

Methods

- Extract lower extremity endovascular cases from ACS-NSQIP database
- ↓
- Impute missing values using Optimal Imputation²
- ↓
- Select features with Minimum Redundancy Maximum Relevance (mRMR). Outcome of interest: 30-day renal failure.
- ↓
- Split data into training (2011–2017) and independent validation (2018) sets
- ↓
- Oversample the training set to balance positive and negative cases
- ↓
- Train and validate a random forest model

Results

The random forest model achieved an **AUC of 0.846** and **accuracy of 0.828**

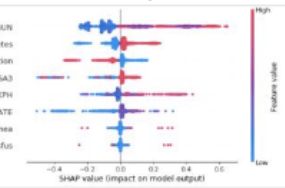


Predictive Features

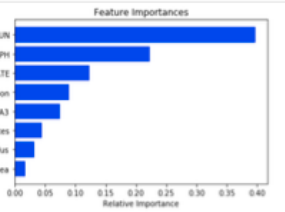
- Preoperative BUN
- Preoperative Alkaline Phosphatase
- Claudication
- ASA > 3
- Preoperative platelet count
- Preop Transfusion of ≥ 1 unit of whole/packed RBCs in 72 hours prior to surgery
- Diabetes mellitus with oral agents or insulin
- Dyspnea

Model Interpretation

We determined the contributions of each predictor to model outcomes. SHapley Additive exPlanations summary plot showing feature contributions to final prediction:



Feature importance based on mean decrease in impurity:



References

1. Rudnick, M., & Feldman, H. (2008). Contrast-induced nephropathy: what are the true clinical consequences? *Clinical Journal of the American Society of Nephrology: CJASN*, 3(1), 263–272.
2. Bertsimas, D., Pawlowski, C., & Zhuo, Y. D. (2018). From Predictive Methods to Missing Data Imputation: An Optimization Approach. *Journal of Machine Learning Research: JMLR*, 18(196), 1–39.

Conclusion

We provide a proof-of-concept machine learning model that effectively stratifies 30-day renal failure risk in PAD patients undergoing lower extremity endovascular procedures. Such a model has the potential to inform preoperative optimization strategies to mitigate this risk and reduce the incidence of CIN in patients undergoing lower extremity endovascular interventions.

Global Structural and Network Topological Alterations in Long-term Nasopharyngeal Cancer Survivors

Rahul Paul, PhD and Annie W. Chan, M.D.

Department of Radiation Oncology, Massachusetts General Hospital, Harvard Medical School, Boston, Massachusetts

PURPOSE

Radiation and chemotherapy are highly effective treatments for patients with nasopharyngeal carcinoma (NPC), with a cure rate of 80% or higher.

Long-term survivors, despite having normal MRIs, commonly suffer from memory impairment and neurocognitive dysfunction. The purpose of the study were:

- To define and quantify the long-term impact of chemoradiation on brain function using general linear model (GLM) and brain connectivity analyses.
- To identify brain regions which show significant changes after radiation.

METHODS

Dataset

- 26 NPC patients.
- 65% male, 35% female
- Median Age: 51 years.
- High resolution T1-weighted MRI scan.
- Follow-up MRI : minimum 5 years (median 8 years).

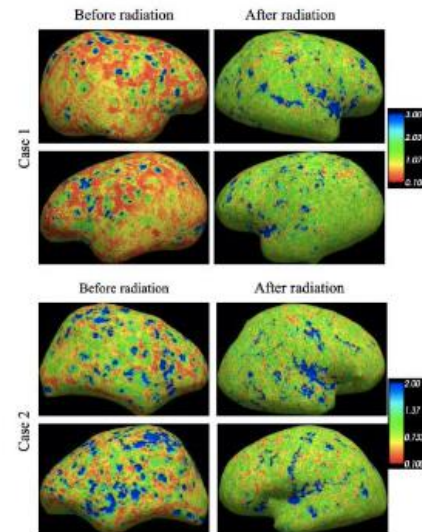


FIGURE 1: Changes in cortical areas before and after radiation

Procedure

- Automated cortical region segmentation : FreeSurfer
- Sixty-eight cortical regions (34 each from left and right brain).
- Cortical cortical areas were analyzed.
- GLM was applied to assess the change in the cortical regions.
- Monte Carlo-simulations were used to correct for multiple comparisons.
- Graph theory-based brain connectome was evaluated to assess the connectivity between different regions of brain.
- Local efficiency and clustering coefficient were used to determine local region connectivity.
- Global efficiency, transitivity, and modularity were used to assess global connectivity.
- Hub regions were identified.
- Age and gender were used as covariates.

RESULTS

GLM Based Analysis

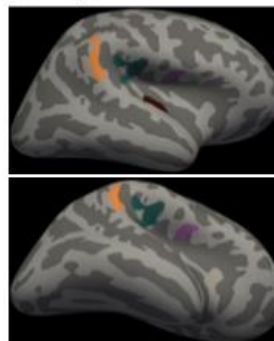


FIGURE 2: Clusters in right brain after multiple corrections

- Four clusters were formed in the right brain: postcentral, supramarginal, transverse/superiotemporal, and precentral
- No clusters in the left brain.

Region-wise Analysis by GLM

- Superiotemporal (average +21 mm² per patient after treatment, p= 0.04)
- Supramarginal (average -87 mm², p= 0.001)
- Postcentral (average -59 mm², p= 0.001)
- Precentral (average -87 mm², p= 0.001)
- Transverse temporal (average +36 mm², p= 0.001)

Brain Connectivity Analysis

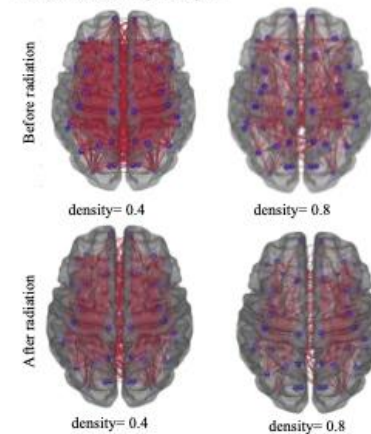


FIGURE 3: Brain Connection before and after radiation with respect to density.

- After radiation, patients presented an abnormal global network topology as reflected by increased modularity and decreased global efficiency and transitivity.

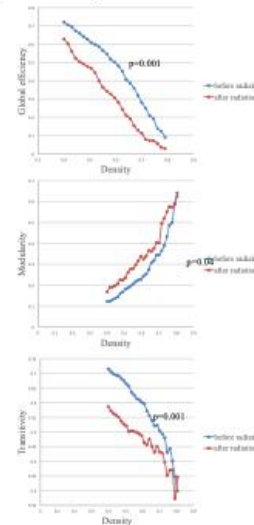


FIGURE 4: Graph measurement plots before and after radiation

Hubs before radiation:

- Right rostral anterior cingulate, right posterior cingulate, right isthmus cingulate, right pericalcarine, right entorhinal.

Hubs post-radiation:

- Left pars opercularis, left caudal anterior cingulate, left insula, left precuneus, left parahippocampal, right parahippocampal.
- Reorganization of hubs after treatment, including the parahippocampal-hippocampus regions, indicating a decline in learning and memory ability.
- Reduced local efficiency and clustering coefficient were observed in the same five brain regions as in the GLM-based analysis (p=0.001).

CONCLUSIONS

- Global and permanent change in cortical areas can be seen after chemoradiation long-term survivors.
- Postcentral, supramarginal, transverse/superiotemporal, and precentral showed the robust change in cortical areas and disrupted connectivity.
- Reorganization of hubs was observed after chemoradiation.

DISCLOSURES

No conflicts of interest, financial or otherwise, are declared by the authors.

FUNDING

The study was supported by Temasek Family Fund.

REFERENCES

- Fischl, B., 2012. FreeSurfer. *NeuroImage*, 62(2), pp.774-781.
- Mijalkov, M., Kakaei, E., Pereira, J.B., Westman, E., Volpe, G. and Alzheimer's Disease Neuroimaging Initiative, 2017. BRAPH: a graph theory software for the analysis of brain connectivity. *PLoS one*, 12(8), p.e0178798.
- Bahrami, N., Seibert, T.M., Kannamuni, R., Bartsch, H., Krishnan, A., Farid, N., Hanangadi-Ghosh, J.A. and McDonald, C.R., 2017. Altered network topology in patients with primary brain tumors after fractionated radiotherapy. *Brain connectivity*, 7(5), pp.299-308.
- Achard, S., Delon-Martin, C., Vértes, P.E., Renard, F., Schenck, M., Schneider, F., Heinrich, C., Kremm, S. and Bullmore, E.T., 2012. Hubs of brain functional networks are radically reorganized in comatose patients. *Proceedings of the National Academy of Sciences*, 109(50), pp.20608-20613.

Mapping Human Cerebellar Development and Connectivity in the First Postnatal Year

Allison R. Chang¹, Hui Wang¹, Jean Augustinack¹, Holly Freeman², Lilla Zöllei¹

¹Laboratory for Computational Neuroscience, Athinoula A. Martinos Center for Biomedical Imaging, Massachusetts General Hospital, ²Department of Neurology, Massachusetts General Hospital



Athinoula A.
Martinos
Center
For Biomedical Imaging



Introduction

Human cerebellar development is critical for the acquisition of multiple motor, language, cognitive, and social skills, as demonstrated by the long-ranging consequences of the perinatal cerebellar injuries seen in up to 19% of infants with birth complications¹.

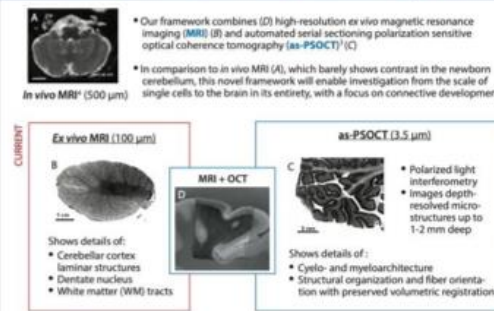
However, current *in vivo* imaging tools have been unable to provide the resolution and sensitivity required to fully assess structural details of the cerebellar cortex, deep cerebellar nuclei (DCN), and connective pathways linking individual cerebellar lobules.

Clinically, this has translated² to the:

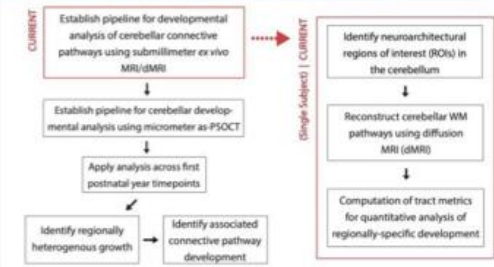
- ① Delayed implementation of interventional procedures for infants with cerebellar injury
- ② Uncertainty on the role of cerebellar lesions in motor and socio-cognitive disorders where contralateral cerebral injury is a substantial confound

We aim to bridge this fundamental gap by developing a multi-scale imaging framework to elucidate the neuroarchitecture and connectivity maps of human cerebellar development in the first year of life.

Novel Cross-Scale Framework for Whole Brain Analysis



Methods: Developing a Next-Generation Cerebellar Reference

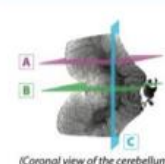


① Neuroarchitectural ROI Characterization in the First-Year Cerebellum

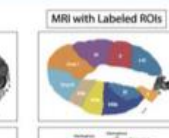
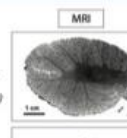
Subject: 7-month-old, born full-term
Imaging: 250 μm isotropic postmortem 3T MR scans

ROI Segmentation Procedure:

- Identify major fissures delineating cerebellar lobules in each hemisphere³
- Subdivide cerebellar lobules into hemisphere and vermis lobules
- Label boundaries of deep cerebellar nuclei⁴

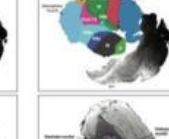


Hemisphere Lobules (Sagittal view)



Left and Right (LH and RH)
Hemisphere Lobules:
I-IV, V, VI, Crus I, Crus II,
VIIb, VIIa, VIIIb, IX, X

Vermis Lobules (Sagittal view)



Vermis Lobules:
VI, Crus I-II, VIIb, VIIIa,
VIIIb, IX, X

Deep Cerebellar Nuclei (DCN) (Axial view)



Left and Right DCN:
Dentate, Interposed, and Fastigial nuclei

② Cerebellar WM Pathway Reconstruction via Deterministic Tractography

Deterministic Tractography Procedure:

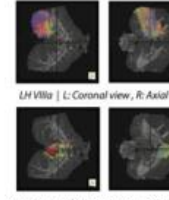
- Resample ROI segmentation volumes via FreeSurfer to align with dMRI (300 μm)
- Individually process ROIs as seed points for tracts in Trackvis
- Constrain pathways to relevant ROI targets
- Reconstruct pathways based on ROI inclusion criteria (excluding insignificant <3mm tracts)

The following 3D white matter (WM) connective pathways were reconstructed in both hemispheres using the manually-labeled cerebellar ROIs:

A Individual Lobular Pathways

Each tract group contains voxels in:

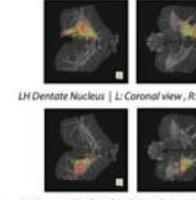
- An individual cerebellar lobe



B Individual DCN Pathways

Each tract group contains voxels in:

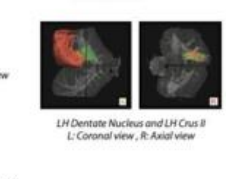
- An individual DCN (dentate nucleus)



C Lobule-DCN Pathways

Each tract group contains voxels in an ROI from both categories:

- Individual cerebellar lobules
- Individual DCN



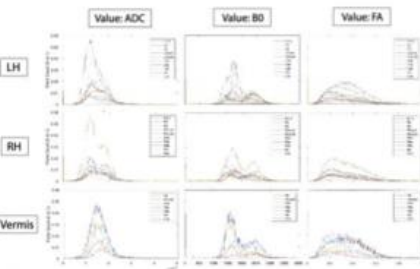
③ Tract Metrics for Quantitative Analysis of Development

• Statistical scalar analysis was conducted along the resulting tracts and ROIs, confirming validity of fiber tract orientation and location obtained from deterministic tractography

• Two sets of quantitative metrics, which will eventually be computed for subjects across time points from the first postnatal year, were obtained to provide a basis for quantitative analysis

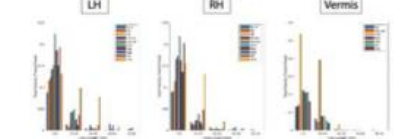
A ADC, BD, and FA Value Analysis

- Average apparent diffusion coefficient (ADC), non-diffusion weighted (BD), and fractional anisotropy (FA) values were computed for all voxels on the tract passing through each lobe
- Graphs show a normalized (0 to 1) proportion of points for each tract group



B Tract Density Analysis

- Tract density was evaluated for each lobe and categorized into one of five groups by tract length: <10, 10-19, 20-29, 30-39, and 40-49 mm



Conclusion

- We established a pipeline for high-resolution *ex vivo* MRI analysis of the infant cerebellum with a focus on neuroarchitecture and connectivity.
- We optimized protocols for ROI characterization of the cerebellar lobules and deep cerebellar nuclei (DCN), as well as tract reconstruction of 3D WM pathways using these ROIs.
- We computed tract metrics via statistical scalar analysis to provide a basis for the future quantitative analysis of cerebellar development across the first year of life.

Future Directions

- ROI characteristics and tract metrics will be collected from additional subjects—potentially by way of an automated process—and used to quantify regionally-heterogeneous changes in pathway development across the first year of cerebellar development.
- Ultimately, this framework will help to create a clinical reference and aid in the development of interventional procedures responding to cerebellar injury in infants.

1. Volpe JJ. *J Child Neurol*. 2009;24(5):585-594.

2. Wang H. *Neuroimage*. 2014;93:58-66.

3. Toga AW. *Neuroimage*. 2013;81(3):414-424.

4. Makrilia E et al. *Neuroimage*. 2015;114:794-794.

We thank the Sunshine Fund for Undergraduate Research and the Harvard College Research Program for funding on this project.



Amblyopia-Related Changes in the Fine-Scale Functional Organization of Human Extrastriate Visual Cortex



Bryan Kennedy¹, Amanda Nabasaliza^{1,4}, Peter Bex³, David Hunter^{4,5}, Roger BH Tootell^{1,2}, Shahin Nasr^{1,2}

1 - Athinoula A. Martinos Center for Biomedical Imaging, Massachusetts General Hospital, Boston, MA

2 - Department of Radiology, Harvard Medical School, Boston, MA

3 - Department of Psychology, Northeastern University, Boston, MA

4 - Department of Ophthalmology, Boston Children's Hospital, Boston, MA

5 - Department of Ophthalmology, Harvard Medical School, Boston, MA

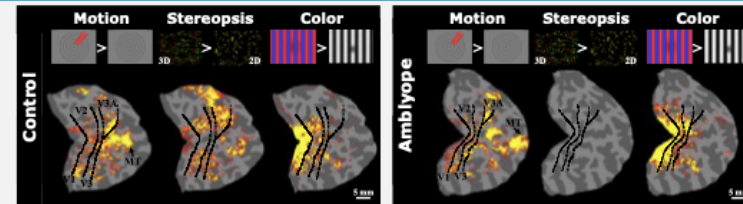
Background

- Amblyopia is a developmental disorder caused by disruption of symmetric binocular visual input early in life.
- Most amblyopic individuals suffer from impairments in stereopsis, spatial vision, and motion perception, especially in the central visual field (McKee et al., 2003).
- However, the underlying neural disorders (e.g. neural degeneration vs. re-organization) have remained mostly unknown.
- This is mainly a result of the small size of the cortical sites in early retinotopic areas that are involved in motion, stereopsis, and color perception compared to the spatial resolution of fMRI techniques used in conventional human studies.
- Here, we studied the impact of strabismus and anisometropia (two major natural causes of amblyopia) on the fine-scale functional organization of specific neuronal structures in human extrastriate visual cortex.

Methods

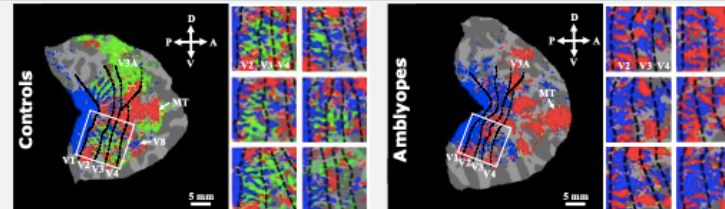
- **Participants:** 25 individuals participated in this study.
 - 11 individuals with amblyopia (7 strabismic and 4 anisometric) participated. Their non-amblyopic eye was equal to or better to 20/20 visual acuity and their stereoaucuity was greater than 250 arc seconds (based on the Randot Stereotest).
 - 14 control individuals with normal or corrected to normal vision and with a stereoaucuity \approx 50 arc seconds participated.
- **Imaging:** We used high-resolution fMRI (1 mm isotropic), collected in a 7T scanner with the following protocol parameter values: TR=3 s; TE=28 ms; flip angle, 78°; BW=1184 Hz/pix; echo-spacing=1 ms; 7/8 phase partial Fourier; 44 oblique-coronal slices; and acceleration factor r=4 with GRAPPA reconstruction and FLEET-ACS with 10° flip angle.
- **Stimuli and procedure:**
 - **Motion-selective** clusters were localized based on the response to moving-vs-stationary gratings (Figure 1 – top left; Tootell and Nasr, 2020).
 - **Stereo-selective** clusters were localized based on the response to 3D-vs-2D random dot stereograms (Figure 1 – top-middle; Nasr and Tootell, 2018).
 - **Color-selective** clusters were also localized in the same subjects, as a control, based on their response to color-vs-luminance varying stimuli (Figure 1 – top-right; Nasr et al., 2016).

Stereo- (but not motion- and color-) selectivity weaken in amblyopes compared to controls



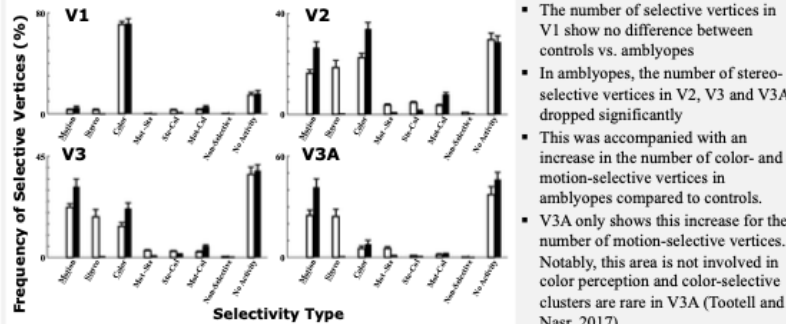
- Each panel shows the significance maps for the activity evoked by the corresponding stimulus contrast.
- In each map red-to-yellow colors indicate a significance from $p<10^{-2}$ to $p<10^{-6}$.
- In most amblyopes, 3D>2D contrast evoked no significant response. Rather, it led to a negative response in subthreshold levels ($p>0.05$).

Interdigitation of motion- and color-selective sites remain intact in amblyopes as in controls



- The figure shows the location of color- (blue), stereo- (green) and motion- (red) selective sites in controls (left) and amblyopes (right). Each panel shows activity from one hemisphere.
- Despite the lack of stereopsis activity in amblyopes, we still see interdigititation of color- and motion-selectivity as in controls.

In absence of stereo-selective sites, motion- and color-selective sites expand in amblyopes compared to controls



- The number of selective vertices in V1 show no difference between controls vs. amblyopes
- In amblyopes, the number of stereoselective vertices in V2, V3 and V3A dropped significantly
- This was accompanied with an increase in the number of color- and motion-selective vertices in amblyopes compared to controls.
- V3A only shows this increase for the number of motion-selective vertices. Notably, this area is not involved in color perception and color-selective clusters are rare in V3A (Tootell and Nasr, 2017).

Summary of Findings

- Our findings indicate that, in the absence of proper binocular input, amblyopia leads to a decrease in the size of stereo-selective sites.
- Interestingly, this effect is accompanied by an increase in the size of motion- and color-selective sites in amblyopes compared to controls.
- Despite this increase in the size of motion-selective sites, the level of motion-selective response, especially in higher speeds and lower coherency levels (around the center of visual field), is weaker in amblyopes compared to controls (not shown here).

Conclusion

- **Consistent with the general idea of brain plasticity, these results suggest that amblyopia leads to functional re-organization of extrastriate cortical sites that are involved in encoding motion and color.**

References

- McKee SP, Levi DM, Movshon JA. The pattern of visual deficits in amblyopia. *Journal of Vision*. 2003;3(5):380-405.
- Nasr S, Tootell RB. Visual field biases for near and far stimuli in disparity selective columns in human visual cortex. *NeuroImage*. 2018;168:358-65.
- Nasr S, Polimeni JR, Tootell RB. Interdigitated Color- and Disparity-Selective Columns within Human Visual Cortical Areas V2 and V3. *J Neurosci*. 2016;36(6):1841-57.
- Tootell RB, Nasr S. Scotopic Vision Is Selectively Processed in Thick-Type Columns in Human Extrastriate Cortex. *Cerebral Cortex*. 2020.
- Tootell RB, Nasr S. Columnar Segregation of Magnocellular and Parvocellular Streams in Human Extrastriate Cortex. *Journal of Neuroscience*. 2017;37(33):8014-32.

Acknowledgments

This work was supported by NIH NEI (grants R01EY026881 and R01EY030434), and by the MGH/HST Athinoula A. Martinos Center for Biomedical Imaging. Crucial resources were made available also by a NIH Shared Instrumentation Grant S10-RR019371.

Investigation of MRI Indices of Cerebral Blood Flow and Venous Oxygenation as Surrogate Markers for Novel Treatments of Sickle Cell Anemia

Erin Hardy^{#1} BS; Iris Chen¹, PhD; Phoebe Chan¹, PhD; James Goodman², PhD; Yi-Fen Yen¹, PhD; Joe Mandeville¹, PhD

1. Athinoula A. Martinos Center for Biomedical Imaging, Department of Radiology, Massachusetts General Hospital

2. Pfizer Inc., Cambridge, Massachusetts

*Email: eehardy@mgh.harvard.edu



Background

- Sickle cell (SC) anemia is an inherited blood disorder affecting hemoglobin
- "Sickle" shaped red blood cells result in hemolysis, low hematocrit (Hct), and reduced oxygen carrying capacity
- Low oxygen from anemia can lead to a wide variety of symptoms and effects on multiple organs
- No treatments currently exist

Introduction

- We investigated the feasibility of using MRI indices of blood flow and oxygenation as markers for novel treatments of SC disease
- Previous report described increased cerebral blood flow (CBF) in SC animals compared to wild type (WT) controls, and evidence of cerebral hypoxia in the SC cohort [Cahill et al. 2017]

Aims:

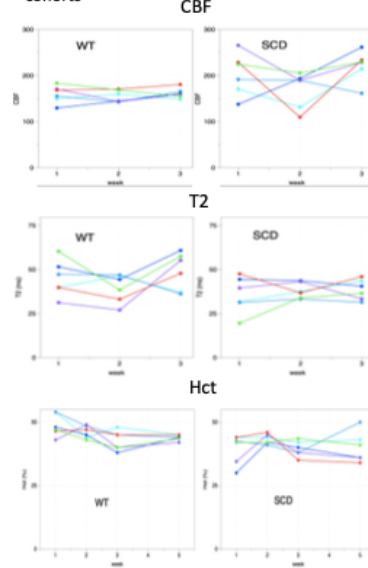
- Determine whether combining measurements of CBF with venous T2 measurements (related to blood oxygenation) yields better differentiation of SC animals compared to CBF alone
- Determine test-retest reproducibility of these measurements.

Methods

- Pseudo-continuous arterial spin labeling (pCASL) sequence to measure CBF [Alsop et al. 2014]
- T2-Relaxation-Under-Spin-Tagging (TRUST) sequence + benchtop hematocrit measurement to estimate blood oxygenation levels (Y_v) [Wei et al. 2014]
- Measurements were performed on 12 mice (6 SC/6 WT) 1x/week for three weeks
- Cohen's D used to quantify differentiation between SC and WT mice
- Mice's body weights were measured and recorded weekly at time of experiments

Results

- Measurements of CBF and venous T2 in the 2 cohorts



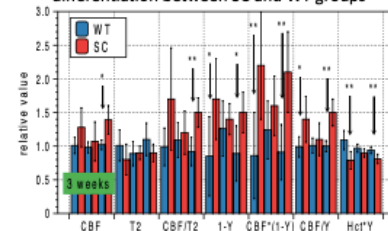
- Test-retest variability was about 20% for MRI measurements of CBF and T2

- All measurements indicated "large" effect sizes ($d > 0.8$). Combining all three measurements yielded the highest degree of differentiation with a Cohen's D value of nearly 3.

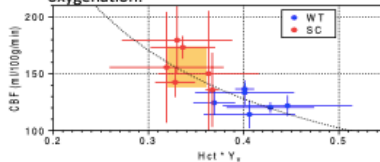
Effect size for SC vs WT

Index	Cohen's d
T2	1.1
CBF	1.3
CBF/T2	1.7
Hct * CBF * (1-Yv)	1.8
CBF/Yv	1.8
Hct	1.9
CBF * (1-Yv)	2.2
CBF/Yv/Hct	2.3
Hct*Yv	2.8

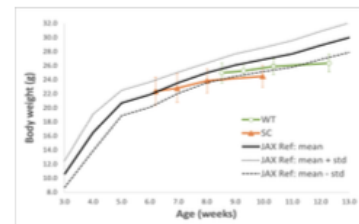
- CBF, Hct, and T2 individual measurements each differed significantly between groups
- CBF*(1-Yv) and Hct*Yv had the greatest differentiation between SC and WT groups



- Average values of CBF vs the product of Hct * Yv showing means and standard deviations across 3 weeks for WT mice and SC mice. Shaded boxes illustrate 95% confidence intervals. The dotted line assumes that CBF is reacting to roughly maintain oxygen delivery in SC mice despite reduced Hct and oxygenation.



- Plot of our animal body weights (both WTs and SCs) as compared to the growth rate published by JAX for the WT



- An animal's body weight is often used to gauge their recovery from blood draws. Both our WT and SC mice are below the JAX figure average WT growth rate (no SC average growth rate was published), which indicated suboptimal recovery from our 1x/week blood draws. For future studies, we will consider drawing blood every two weeks, rather than weekly.

Conclusions

- Combining measurements of CBF, Hct and venous T2 is a valuable surrogate index for oxygen carrying capacity in SC animals that can be used to monitor efficacy of novel treatments
- The information of test-retest reproducibility will be used in power calculations to determine sample size needed in the treatment study.

References

- Cahill LS, Gazdzinski LM, Tsui AK, Zhou YQ, Portnoy S, Liu E, Mazer CD, Hare GM, et al. (2017), Functional and anatomical evidence of cerebral tissue hypoxia in young sickle cell anemia mice. *J Cereb Blood Flow Metab* 37:994-1005.
- Alsop DC, Detre JA, Golay X, Gunther M, Hendrikje J, Hernandez-Garcia L, Lu H, Macintosh BJ, et al. (2014), Recommended implementation of arterial spin-labeled perfusion MRI for clinical applications: A consensus of the ISMRM perfusion study group and the European consortium for ASL in dementia. *Magn Reson Med*.
- Wei Z, Xu J, Liu P, Chen L, Li W, van Zijl P, Lu H (2018), Quantitative assessment of cerebral venous blood T2 in mouse at 11.7T: Implementation, optimization, and age effect. *Magn Reson Med* 80:521-528.



Cortical functional connectomics describe genetic-evolutionary features of the human brain

Elisenda Bueichekú, Jose M. Gonzalez-de-Echavarri, Laura Ortiz-Teran, Victor Montal,

Federico d’Oleire Uquillas, Lola De Marcos, William Orwig, Chanmie Kim, Elena Ortiz-Teran, Silvia Basaia, Ibai Diez, Jorge Sepulcre

Gordon Center for Medical Imaging, Department of Radiology, Massachusetts General Hospital, Harvard Medical School, Boston, USA



Introduction

The relationships between human brain connectomics and its genetic evolutionary traits^[1,2] remain elusive due to the challenges in combining complex associations within the cerebral tissue. Currently, there is a steadily growing interest in generating scientific evidence surrounding our survival as a species and our uniqueness compared to other non-human primates is at the grounds of improving our knowledge about brain functioning. In the present research, we provide new insights about the relationship between cortical connectomics, gene expression and divergent evolutionary pathways that the human brain underwent 5-8 million years ago.

Methods

Unfolding the segregation and integration topological organization of the human connectome

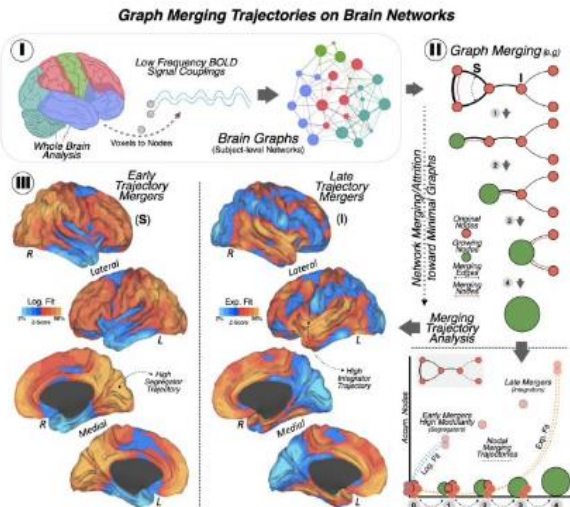
- Resting-state fMRI data from Human Connectome Project [3]
- Link level graph-analytical measures (similar to previous works^[4,5])

Linking the connectome to genetic information

- Spatial similarity approach between connectomics and genetics (Allen Human Brain Atlas [6])
- Gene-cell traits relations (Gene enrichment analysis in Metascape^[7])

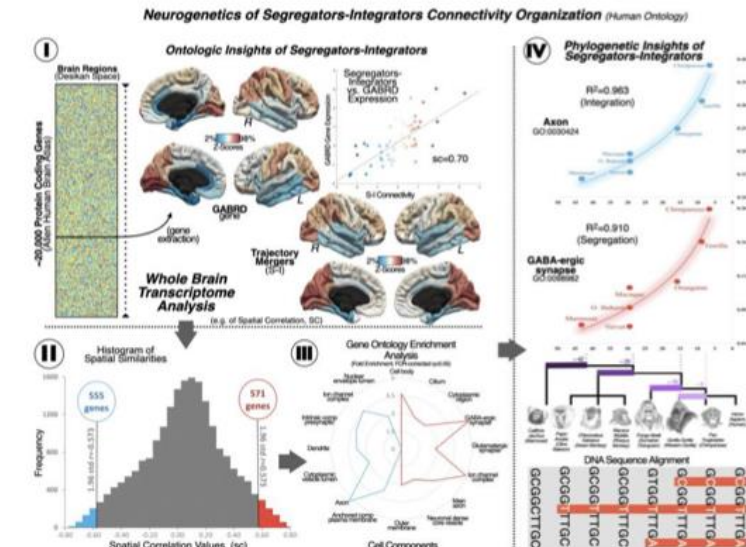
Understanding the relationship between evolution times and connectomic-genetic evidence

- Orthologues comparisons (Ensembl – BioMart [8] and dN/dS ratio [9])
- Humans vs. seven non-human primates



Conclusions

Previous authors have investigated the intersection between genetic expression and evolutionary divergences while trying to understand which specific genetic mutations have led to human cognitive phenotypes [10, 11, 12, 13]. Our approach, which investigated the junctions between cortical connectivity systems and genetic-evolutionary features, led us to conclude that the balance in topological brain architecture and axonal/GABAergic is at the base of specific conserved and diverged key qualities of the human brain evolution.



Results

At the connectomic level, we found that two topologically idiosyncratic networks co-exist: one, with a fast and early merging tendency between connectivity neighborhoods, which supports functional specialization and segregation; and another that shows slow and late merging propensities which is devoted to systems integration. Then, we identified the genetic profiles associated with these networks, as well as their underlying biological gene-cell enrichment patterns: the segregation-based nodes were linked to Axon-related annotations, while the integration-based nodes were related to the GABAergic synapse-related annotations. Finally, we observed that current network organization and functioning of the human brain is traced by positive selection through the *Homo Sapiens* lineage.

References

- Spira, A. M. M., Meyer, K. A., Sutcliffe, G., Golden, F. O., & Soares, N. (2017). *Cell*, 176(2), 226–247. <https://doi.org/10.1016/j.cell.2017.06.056>
- Loktionova, A. A. (2016). *Journal of Anthropological Sciences*, 94, 127–146. <https://doi.org/10.4371/jans.940259>
- Holmes, J., et al. (2015). *Scientific Data*, 2(1), 150031. <https://doi.org/10.1038/sdata.2015.31>
- Bordoli, E., et al. (2020). *Proceedings of the National Academy of Sciences of the United States of America*, 117(12), 6836–6843. <https://doi.org/10.1073/pnas.1912629117>
- Dier, L., & Sopel, J. (2018). *Nature Communications*, 9(1), 1–10. <https://doi.org/10.1038/s41467-018-04700-w>
- Hovsepian, M. J., et al. (2012). *Nature*, 489(7416), 391–399. <https://doi.org/10.1038/nature11493>
- Shots, S. J., & Novotny, J. P. (2010). *Trends in Genetics*, 26(3), 118–119. <https://doi.org/10.1016/j.tig.2009.12.009>
- Yates, J. D., et al. (2001). *Nucleic Acids Research*, 29(1), D482–D488. <https://doi.org/10.1093/nar/29.1.482>
- Krywawych, S., & Plotkin, J. B. (2008). *PLoS Genetics*, 4(2), e1003944. <https://doi.org/10.1371/journal.pgen.1003944>
- Fried, K. N., et al., (2013). *Nature Reviews Genetics*, 14(2), 137–147. <https://doi.org/10.1038/nrg3400>
- Shots, S. J., & Novotny, J. P. (2013). *Nature Reviews Neuroscience*, 14(2), 112–127. <https://doi.org/10.1038/nrn3572>
- Vallender, E. J., Makel-Sobres, N., & Loh, B. T. (2008). *Trends in Neuroscience*, 31(12), 637–644. <https://doi.org/10.1016/j.tins.2008.09.010>

Novel COX-2 PET radiotracer [¹¹C]BRD1158 demonstrates high brain uptake and specific binding in the brain with PET in AAV-COX-2 rat model

Placzek MS ^{1,2,3}, Weiner M ⁴, Riley MM ^{1,2}, Wilton DK ⁵, Reid SE ^{1,2}, Liang C ^{1,2,3}, Decultot L ⁴, Wang JM ^{1,2}, Wagner FF ⁴, Stevens B ^{3,5}, Hooker JM ^{1,2,3}

¹A. A. Martinos Center for Biomedical Imaging, Charlestown, MA, USA.

²Massachusetts General Hospital, Boston, MA, USA.

³Harvard Medical School, Boston, MA, USA.

⁴Stanley Center for Psychiatric Neuroimaging, Broad Institute of MIT and Harvard, 75 Avenue Street, Cambridge, MA, USA.

⁵Department of Neurology, F.M. Kirby Research Center, Boston Children's Hospital, Boston, MA 02115, Massachusetts, USA.

Abstract

COX-2 is implicated in neurodegenerative and neuroinflammatory disease pathogenesis and is the target of numerous therapeutic drugs. We developed and evaluated a novel COX-2 PET radiotracer, [¹¹C]BRD1158, that demonstrates COX-2 specificity and high uptake in the rodent and baboon brain. Our results show that [¹¹C]BRD1158 is an ideal radiotracer for *in vivo* PET imaging of COX-2, and we recommend translation of this tracer to human neuroimaging.

Introduction

Cyclooxygenase-2 (COX-2) is an enzyme that catalyzes the conversion of arachidonic acid to prostaglandins and thromboxanes. In the brain, COX-2 is specifically upregulated in response to inflammatory events, including neurodegenerative diseases (1). In the healthy brain, COX-2 has low basal expression, creating significant challenges for radiotracer evaluation. To circumvent this, others have used LPS administration to induce a general state of neuroinflammation, ultimately driving COX-2 overexpression (2). Unfortunately, this model causes massive disruption of many immune mediators and is nonspecific for COX-2 overexpression. In this work, we incorporated viral vector technology (adeno-associated virus, AAV) to induce localized overexpression of human-COX-2 in the brain of Sprague Dawley rats. We utilized this AAV-COX-2 rat model to evaluate a novel COX-2 PET radiotracer we developed, [¹¹C]BRD1158. BRD1158 has improved COX-2 affinity, plasma free fraction ($f_{1,0,p}$) and faster on-rate (k_{on}) for COX-2 compared to rofecoxib, celecoxib, and MC1. *In vivo* PET studies in healthy rats, AAV-COX-2 rats, and healthy nonhuman primates demonstrate that [¹¹C]BRD1158 warrants translation to humans for imaging COX-2 in the brain.

Acknowledgements

This project was funded by the National Institute of Neurological Disorders and Stroke.

We would like to thank Jonah Weigand-Whittier, Vishal Birar, and Phil Nielson for their assistance.

Methods

[¹¹C]BRD1158 was radiolabeled at the methylsulfone by treating the corresponding thioester precursor with [¹¹C]CH₃I. To evaluate [¹¹C]BRD1158 brain uptake, we measured whole brain SUV in healthy rats and baboons with PET-MR. AAV-COX-2 rat model was developed by injecting rats locally (icv) with AAV-hCOX-2 construct in the right hemisphere (striatum) and AAV-GFP (control) in the contralateral striatum. On day 36, AAV-COX-2 rats underwent dynamic PET with [¹¹C]BRD1158 at baseline followed by a blocking study. In this blocking study, animals were pretreated with a heterologous COX-2 inhibitor, celecoxib (1 mg/kg, i.v.) prior to radiotracer administration and dynamic PET. Regional brain time activity curves for both rat and baboon were generated with PMOD using PxRat atlas and b2k baboon atlas.

Results

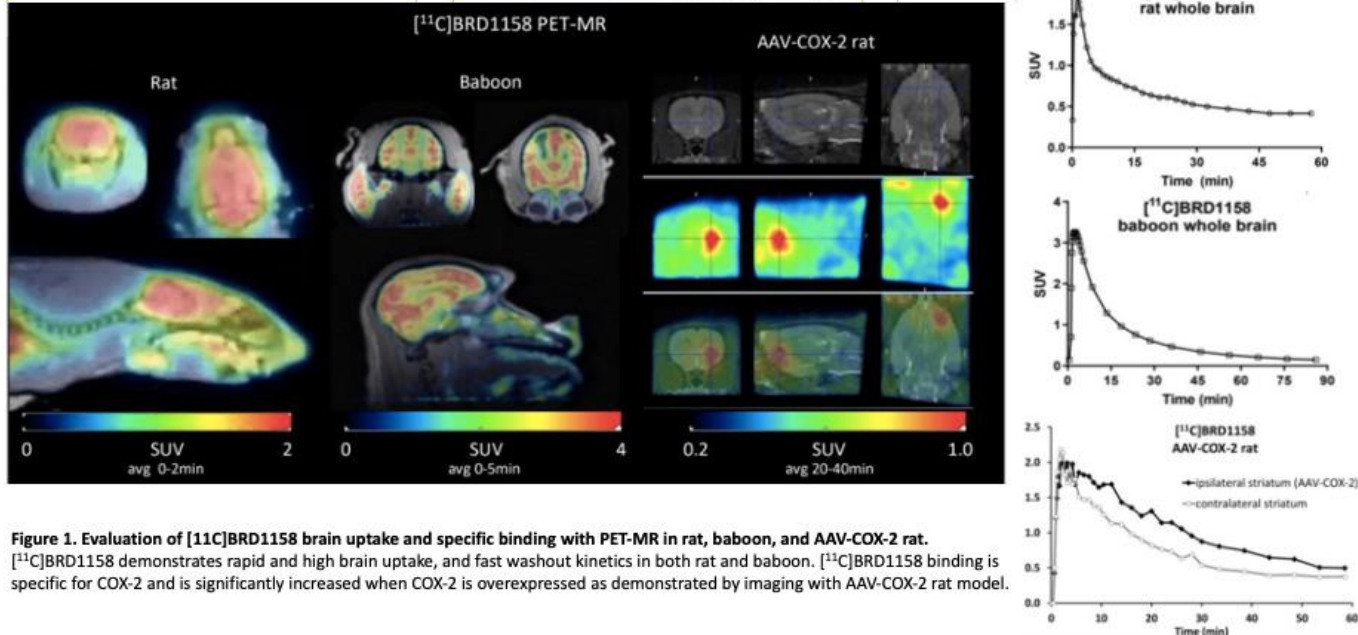
Using an LC-MS-based COX-2 enzymatic assay, BRD1158 was a potent COX-2 inhibitor ($IC_{50}= 20$ nM), compared to rofecoxib (600 nM), and MC1 (43 nM). *In vivo* PET studies showed [¹¹C]BRD1158 has high brain uptake in rat (whole brain SUV $C_{max}= 1.9$) and baboon (whole brain SUV $C_{max}= 3.3$), and favorable washout kinetics for a brain PET radiotracer given the low basal expression of COX-2 (rat $t_{1/2}= 7.8$ min; baboon $t_{1/2}= 17.2$ min). To demonstrate [¹¹C]BRD1158 was specific for COX-2 *in vivo*, AAV-COX-2 rats were imaged with [¹¹C]BRD1158 at baseline (scan 1) and following the COX-2 inhibitor celecoxib (1m/kg, i.v., 5 min pretreat) for scan 2 (consecutive PET scans). Our results show significantly higher uptake in ipsilateral AAV-COX-2 site ($SUV_{30-50\text{ min}}= 0.775$) compared to contralateral striatum ($SUV_{30-50\text{ min}}= 0.493$) or cerebellum ($SUV_{30-50\text{ min}}= 0.406$). The high uptake in ipsilateral striatum was completely blocked by celecoxib pretreatment prior to radiotracer administration ($SUV_{30-50\text{ min}}= 0.412$).

Conclusion

We have identified BRD1158 as a potent and selective COX-2 inhibitor that has improved physicochemical and pharmacological properties compared to existing COX-2 ligands. *In vivo*, [¹¹C]BRD1158 had high brain uptake in both healthy rat and baboon. [¹¹C]BRD1158 PET also demonstrated saturable and specific binding for hCOX-2 in the AAV-COX-2 rat model. Further evaluation is underway to prepare for eIND and first-in-human COX-2 brain PET studies with this radiotracer.

References

- Bartels A, Leenders K. Cyclooxygenase and Neuroinflammation in Parkinson's Disease Neurodegeneration. *Curr Neuropharmacol*. 2010;8(1):62-8.
- Shrestha S, Kim MI, Eldridge M, Lehmann ML, Franklin M, Liow JS, et al. PET measurement of cyclooxygenase-2 using a novel radioligand: Upregulation in primary neuroinflammation and first *in-human* study. *J Neuroinflammation*. 2020;17(1):1-17.



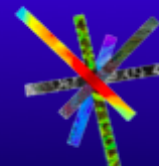
Moving MRI: Imaging a Moving Body with a Moving MRI Magnet

Jingting Yao, PhD;^{1,2} Nikhil Kumar Patel, MS;² Artan Kaso, PhD;^{1,2} Aditi Kulkarni;^{1*} Shizhong Xu;^{1*} Andre van der Kouwe, PhD;^{1,2} Iris Chen, PhD;^{1,2} Jerome L. Ackerman, PhD;^{1,2}

¹Martinos Center for Biomedical Imaging, Department of Radiology, Massachusetts General Hospital; ²Harvard Medical School; *Summer Interns

Csilla Haburcakova, PhD;³ Daniel Merfeld, PhD;⁴ Peter Le, PhD⁵

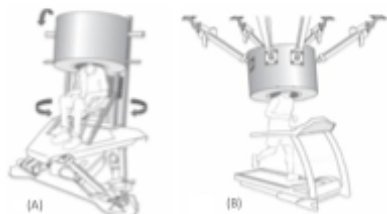
³Massachusetts Eye and Ear Infirmary; ⁴Department of Otolaryngology, Ohio State University College of Medicine; ⁵Naval Medical Research Unit Dayton, Wright Patterson Air Force Base



Moving MRI Concept

The conventional fMRI paradigm is limited to tight, horizontal magnetic bores, and requires the subject to remain stationary with respect to the magnet to minimize motion artifacts.

Moving MRI is a new concept enabling high-resolution anatomic and functional imaging of the brain while the entire head or body is undergoing natural large-scale movement.



Idealized renditions of future human mMRI scanners. (A) Magnet and subject chair rigidly attached to multi-axis motion platform. (B) Active mMRI utilizing compliant robots which dynamically position the magnet to follow the head of a subject engaged in active naturalistic motion. (D. Merfeld).

Broad Impact

Moving MRI would for the first time enable recording of high quality anatomic and functional images in subjects experiencing true motion stimulation.



Vestibular physiology: While unnatural vestibular stimuli tell us something about brain activation during vestibular stimuli, they cannot mimic the rich sensory interactions that occur normally.



Motor control: Conventional fMRI studies of motor control are performed with subjects supine and completely stationary. The moving MRI system will eventually enable us to image the entire brain with the neural modulation normally present for large-scale motion tasks.



Traumatic brain injury: Moving MRI enables measurements of tissue deformation and fluid displacement based on realistic tissue elastic moduli at modest accelerations.

Prototype Development

Cryogen-free conduction-cooled superconducting 1.5T magnet

- The main coil is conduction-cooled by an electrically powered cryocooler, eliminating the need for liquid helium or nitrogen (a.k.a. cryogen-free).
- Internal mechanical structure is robust enough to allow movement and tilting while at field.
- Tested for field stability while in motion (horizontal acceleration, dynamic tilt).



Motion platform

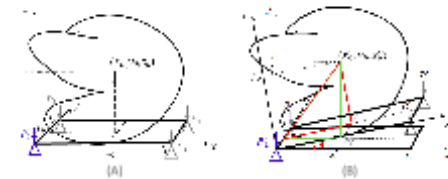
A precisely controlled motion paradigm will be integrated to the scanner system to enable motionless between the magnet and head during movement.

- The magnet will be supported on horizontal axes (~90° pitch) mounted on a turntable (~180° yaw).
- Both axes driven by servomotors.
- Peak rate = 6 RPM (0.1 Hz or 36°/s). For comparison, normal human detection threshold is ~2°/s.
- Compressed gas hoses and electronic cables not shown. [Click for video](#).



Center of gravity

To minimize torques and moments on the magnet assembly, we need to rotate the magnet about its center of gravity. The position of the center of gravity can be found using a multiple-point weighing method with a single strain gauge.

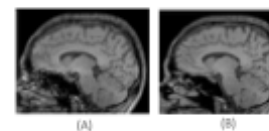


Configuration of measuring center of gravity of a random 3D object. A single strain sensor (symbolically represented in a blue triangle) is placed at each corner when the object is (A) on the floor and (B) elevated by a small angle on one side. Three place-holders at the other three corners allow for even surface contact and force distribution.

Feasibility Validation

Phantom studies

- Create a series of rigid phantoms for quantifying spatial resolution. These phantoms will emulate the mechanical compliance of brain tissue.
- Employ motion artifact correction schemes to suppress residual effects of motion, and validate the use of the cloverleaf navigator in the prototype mMRI system to achieve high performance navigators.



Live animal studies

- Compare static and moving anatomic and functional imaging of awake, behaving rats.
- Prepare rats with a surgically implanted nonmetallic head bolt for restraint within the magnet.
- Acquire resting state functional MRI to map brain activation under various motion paradigms.

Quantitative metrics

Images will be quantitatively characterized for SNR, spatial resolution, and for the stability over repeated scans of positional alignment, SNR and spatial resolution during the motion.

Acknowledgments

This research is supported by National Institutes of Health grant 1R01EB029818 from the National Institute Of Mental Health (NIMH) and the National Institute Of Biomedical Imaging and Bioengineering (NIBIB).

The cryogen-free superconducting magnet was produced by Superconducting Systems, Inc., Billerica, MA under NIH grant 4R44AR065903 (MRI scanner development subcontract to MGH).

References

- Lopez C and Blanke O. Nobel Prize centenary: Robert Bárány and the vestibular system. *Current Biology* 2014, vol. 24, no. 21, p. 1026–1028.
Wang M, Zhang X, Tang W, and Wang J. A Structure for Accurately Determining the Mass and Center of Gravity of Rigid Bodies. *Applied Sciences* 2019, vol. 9, no. 12, p. 35–32.



GROUP 6 – Optical Imaging

BOSTON
UNIVERSITY

A System for Simultaneous BOLD fMRI and Optical Imaging in Awake Mice

Patrick Doran¹, Philipp Mächler¹, Martin Thunemann¹, Ikbal Sencan², Kivilcim Kilic¹, Buyin Fu²,
Yuanyuan Jiang², Xin Yu², Joseph B. Mandeville², Sava Sakadzic², Anna Devor^{1,2}

¹Department of Biomedical Engineering, Boston University, Boston, MA 02215, USA

²Martinos Center for Biomedical Imaging, Department of Radiology, Harvard Medical School, Charlestown, MA 02129, USA



Abstract

Functional magnetic resonance imaging (fMRI) based on the blood oxygenation level dependent (BOLD) contrast is widely used as a non-invasive imaging method. However, the physiological basis for these measurements remain unclear. Combining BOLD fMRI and optical imaging of fluorescent neuronal activity probes in mice can hold the key to understanding the causes of fluctuations in the BOLD signal at the level of neuronal networks. Investigations of large-scale cortical activity patterns are achievable through a clear optical view over the entire dorsal cortical surface. However, magnetic susceptibility artifacts due to the presence of the cranial window present a major challenge for BOLD fMRI. The goal of the present study is to demonstrate the feasibility of simultaneous BOLD fMRI and optical fluorescence imaging. In the present study, we demonstrate that we can achieve high quality BOLD imaging at 9.4 T in mice chronically implanted with large (modified from "Crystal Skull") cranial windows.

Optical Imaging Results

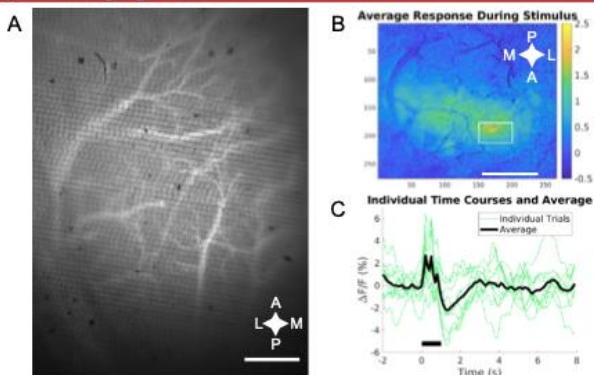


Fig 2. Optical Imaging Results. A) Fluorescence image of cortical vasculature. Scale Bars = 1 mm B) Average whisker airpuff stimulus response in mice expressing GCaMP6f in layer 5 pyramidal neurons. This is an average of (n=10) 1 s stimuli. C) Time course of the GCaMP signal from the white box in (B).

Acknowledgments and References

We would like to acknowledge support from BRAIN initiative grants R01MH111359 and R01DA050159

- Desjardins, M., Kılıç, K., et al. (2019). Awake Mouse Imaging: From Two-Photon Microscopy to Blood Oxygen Level-Dependent Functional Magnetic Resonance Imaging. *Biological Psychiatry: Cognitive Neuroscience and Neuroimaging*, 4(6), 533–542.
- Kim, T. H., et al. (2016). Long-Term Optical Access to an Estimated One Million Neurons in the Live Mouse Cortex. *Cell Reports*, 17(12), 3385–3394.
- Lake, E. M. R., et al. (2020). Simultaneous cortex-wide fluorescence Ca²⁺ imaging and whole-brain fMRI. *Nature Methods*, 17(12), 1262–1271.

* Contact: pdoran@bu.edu

Imaging System Design

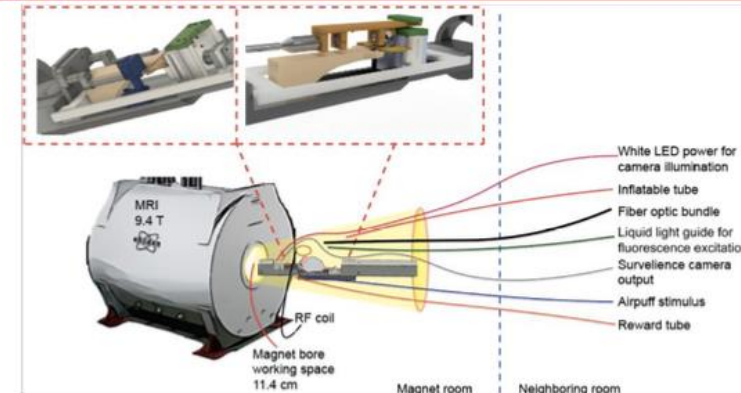


Fig. 1. Design of a system for simultaneous BOLD fMRI and optical imaging. Main schematic shows all connections to the control room next to the scanner. Left inset shows the design of the area where the mouse is head-fixed to the beige block. The right inset shows the collection side of the optical imager.

BOLD fMRI Results

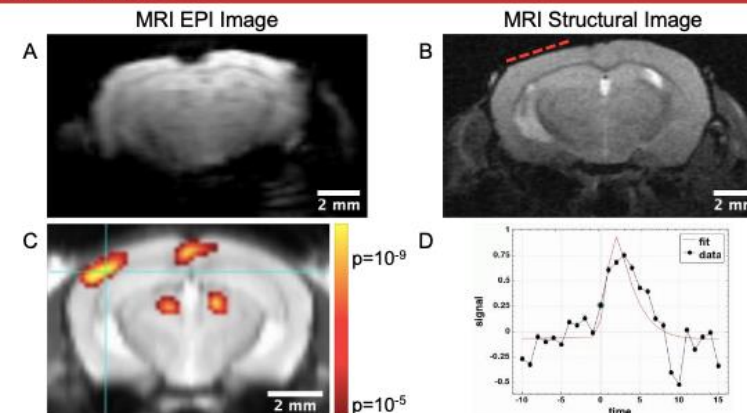
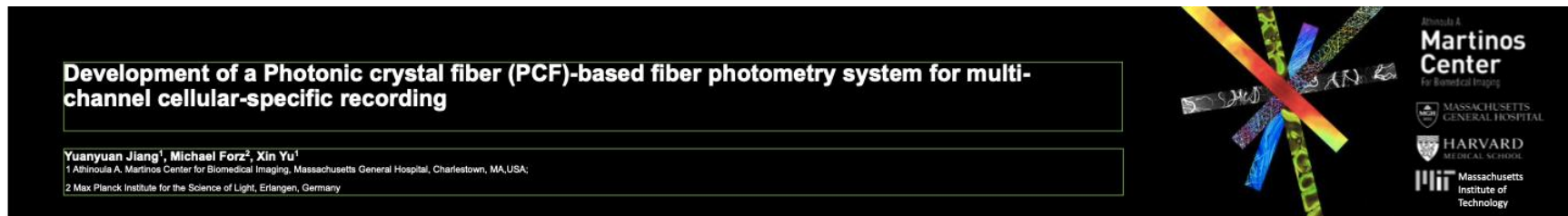


Fig. 3. BOLD fMRI in mice with optical windows. A. MRI image encoded with the pulse sequence (EPI) used for functional imaging. B. Structural MRI Image: Red line shows window. C. fMRI p value map for 40 repetitions of a 2 second airpuff to the right whiskers. D. BOLD time course at the crosshairs in (C) averaged over stimuli.



Introduction

Fiber photometry has been routinely used to record Ca^{2+} signals based on the genetically encoded calcium indicators (GECI) in anesthetized and freely moving animals^{1,2}. Given its MR compatibility and fast sampling of Ca^{2+} transients in the millisecond scale, fiber photometry presents a powerful surrogate of *in vivo* electrophysiological recording when combining with fMRI to decipher the neuro-glio-vascular (NGV) coupling events³. However, it remains challenging to distinguish cellular-specific NGV signaling events at deep brain regions using fiber photometry. Here we developed a photonic crystal fiber (PCF) array-based multi-channel recording system, enabling the detection of cell-specific neuronal signals (GCaMP-based Ca^{2+} or GluSNFR-based Glutamate) from local NGV circuits⁴.



Figure 1. The scheme of fiber recording system with simultaneous fMRI to detect the cell-specific neuronal with vessel-specific signaling in local neuro-glio-vascular (NGV) coupling events.

Methods

The multichannel PCF array has interleaved solid and hollow cores, allowing optical signal transmission through solid cores with little interference from adjacent ones using a specific light path design. Each solid core has a diameter of 8-10 microns, matching the size of the neuronal soma, and the total PCF array tip covers 36 channels for *in vivo* parallel imaging.

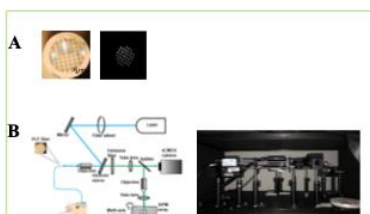


Figure 2. The designed array-based multi-channel recording system. (A) PCF fiber design and its projection imaging on the sCMOS camera. (B) The PCF-based imaging scheme and setup with 36 channels for *in vivo* parallel imaging.

Phantom measurement

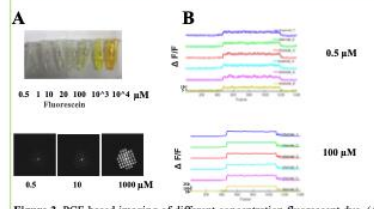


Figure 3. PCF-based imaging of different concentration fluorescent dye. (A) Imaging of different concentration of fluorescent dye from 0.5 μM to 10 mM. (B) Representative signal change of 6 channel when the fiber tip inserted to 0.5 and 100 μM concentration of dye.

Acknowledgments & References

The research was financial supported by NIH Brain Initiative funding (RF1NS113278-01, R01MH111438-01, S10MH124733, R01NS120594).

1. Reichert, J. et al. Fiber optic arrays for simultaneous fluorescence-based calcium recordings and BOLD fMRI in mice. *Nat Protoc.* 13, 846–855, doi:10.1038/nprot.2018.003 (2018).
2. Zeng, W. et al. Fast high-resolution multiway two-photon microscopy for brain imaging in freely behaving mice. *Nat Methods* 14, 713–719, doi:10.1038/nmeth.4507 (2017).
3. Wang, M., He, Y., Sopowicz, T. J. & Yu, X. Brain activity-dependent astrocytic Ca^{2+} signals are coupled to both positive and negative BOLD-fMRI signals. *Proc Natl Acad Sci U S A* 115, E1647–E1656, doi:10.1073/pnas.1711992115 (2018).
4. Jiang, Y., Chen, X., and Yu, X. (2018). Fiber optic mediated extracellular glutamate and intracellular calcium recording with GCaMP8B. *Int. Soc. Magn. Reson. Med.*

Multichannel Glu/Ca Signal Recording

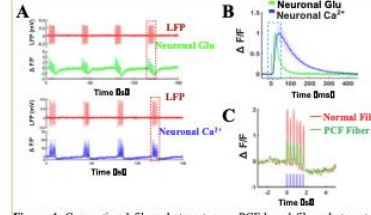


Figure 4. Conventional fiber photometry vs. PCF-based fiber photometry. (A) One representative channel of fiber photometry recording with simultaneous electrophysiological recording for neuronal Ca^{2+} and neuronal glutamate (Glu) signal. (B) The temporal features of evoked neuronal Ca^{2+} and Glu responses. (C) The evoked Glu signals were acquired by either normal fiber or PCF fiber array.

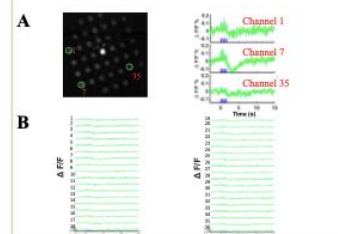


Figure 5. (A) The PCF-based Glu recording with 36 channels. The evoked Glu spikes from three representative channels (1, 7, 35) showed different temporal dynamics. (B) The multi-channel time traces of Glu signals from 36 channels of the PCF array with electrical stimulation of the forepaw (3 Hz, 2 s, 2mA) in rat FP-S1..

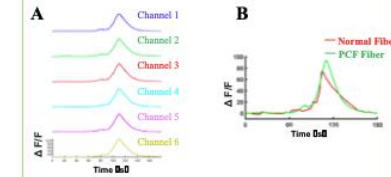
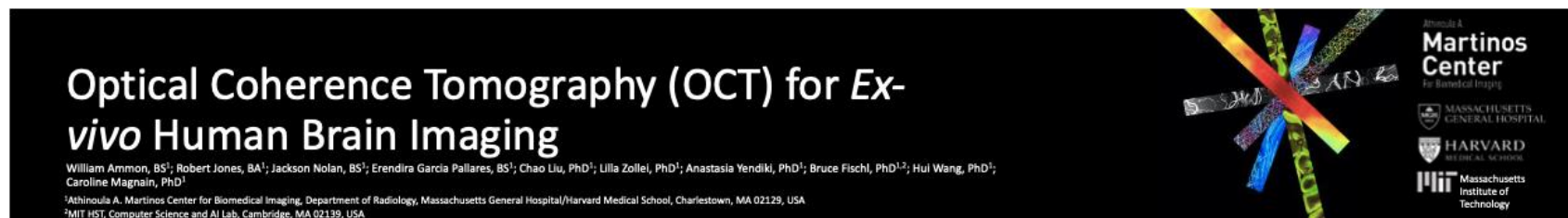


Figure 6. The PCF array detected spreading depression events in different channels (A) in comparison of spreading depression events with conventional fiber (B).

Conclusion & Outlook

The PCF-based multi-channel recording strategy leads to extraordinary properties of the optical waveguide. Different from conventional fiber bundles, the PCF array enables multi-channel ultrafast cellular recording with significantly reduces cross-talk, providing a unique recording device to measure distinct signaling events in the local brain circuit. In the next step,

- we will increase the coverage distance across cortical layers. Detect the layer-specific neuronal Ca^{2+} /Glu signal with simultaneous line-scanning fMRI.
- we will further explore the multi-core optical signal recording with cellular specificity to link the distinct singling events across the neuro-glio-vascular circuit in different brain regions.



Optical Coherence Tomography (OCT) for *Ex-vivo* Human Brain Imaging

William Ammon, BS¹; Robert Jones, BA¹; Jackson Nolan, BS¹; Erendira Garcia Pallares, BS¹; Chao Liu, PhD¹; Lilia Zollei, PhD¹; Anastasia Yendiki, PhD¹; Bruce Fischl, PhD^{1,2}; Hui Wang, PhD¹; Caroline Magnain, PhD¹

¹Athinoula A. Martinos Center for Biomedical Imaging, Department of Radiology, Massachusetts General Hospital/Harvard Medical School, Charlestown, MA 02129, USA
²MIT HST, Computer Science and AI Lab, Cambridge, MA 02139, USA

Background

Optical coherence tomography (OCT) is a non-invasive volumetric imaging technique, primarily used in ophthalmology. We have adapted OCT for use imaging *ex-vivo* brain tissue; we can obtain 3D volumes at higher resolution than MRI and with greater imaging depth than confocal microscopy [1].

Reconstruction of a 3D Volume

Two example tiles of *ex-vivo* brain tissue (A) shown in multiple contrasts. These individual tiles are then stitched together to reconstruct 2D slices. Slices are then stacked to reconstruct a 3D volume (B) where a cross-section perpendicular to the imaging plane can be seen (C) [2]. AIP; average intensity projection. MIP; maximum intensity projection.

System

Collaborators: Chao Liu, Ruopeng Wang, William Kostis

The automatic serial sectioning (as) PS-OCT system is based on the Telesto system from ThorLabs, that we are continually optimizing for human brain imaging.

Infant Brainstem

Tissue Bank:
- 12 whole brains;
- 1m < age < 1.5 years;
- 6 males, 6 females;
- 3 SIDS + 6 brainwars

MR Acquisition:
Structure (T1, 200μm)
Diffusion (DTI, 750μm, 90 directions)

OCT Sectioning:
- 5mm - rostral medulla, caudal medulla, pons, and midbrain

OCT Imaging:
2.5μm lateral resolution isotropic

Registration:
- OCT/MR co-registered
- Create infant brainstem atlas for all datasets

Segmentation:
- Manual
- Smartinterpolation - semi-automated

Histology Validation:
- Nissl Staining (neurons)
Gallyer Staining (fibers)

Sudden Infant Death Syndrome (SIDS) is one of the leading causes of death in postnatal infants. It is hypothesized that the underlying cause of SIDS is found in physiological and developmental abnormalities of the infant brainstem. An atlas is being created from OCT data to detect the anatomical biomarkers in the registered MR data that are associated with SIDS mortality.

Diffusion MRI Validation

Extract *ex vivo* block from hemi
Diffusion MRI 9.4T (0.3 mm)
PSOCT (0.01 mm)
Retardance Orientation
Estimate dMRI fiber orientations
Compare

Diffusion MRI (dMRI) is a valuable tool for mapping brain connectivity but requires validation. We use microscopic fiber orientations measured with PSOCT as a reference for validating mesoscopic dMRI fiber orientation estimates. Using PSOCT as a ground truth allows us to investigate the effect of experimental factors (e.g., spatial resolution, acquisition scheme, reconstruction method) on the accuracy of dMRI fiber orientations [3].

Acknowledgements

This work was supported by the National Institutes of Health (NIH), in part by the BRAIN Initiative Cell Census Network grant (U01MH117023), the National Institute for Biomedical Imaging and Bioengineering (R01EB023993, R01EB030006), the National Institute for Neurological Disorders and Stroke (R01NS119911, R21NS106695), and the Eunice Kennedy Shriver National Institute of Child Health & Human Development (R01HD102616, R21HD095338). Additional support was provided by the Chan Zuckerberg Initiative DAF, an advised fund of the Silicon Valley Community Foundation (2019-198101).

References

- Subhash H.M., Wang R.K. 2013. Optical Coherence Tomography: Technical Aspects. In: Liang R. (eds) Biomedical Optical Imaging Technologies. Biological and Medical Physics, Biomedical Engineering. Springer, Berlin, Heidelberg.
- Wang, H.; Magnain, C.; Wang, R.; Dubb, J.; Varjabedian, A.; Tirrell, L.S.; Stevens, A.; Augustinack, J.C.; Konukoglu, E.; Aganj, I.; Frosch, M.P.; Schmahmann, J.D.; Fischl, B.; Boas, D.A.; 2018. as-PSOCT: Volumetric microscopic imaging of human brain architecture and connectivity. *NeuroImage* 165, 56-68.
- Jones, R.; Grisot, G.; Augustinack, J.; Magnain, C.; Boas, D.A.; Fischl, B.; Wang, H.; Yendiki, A.; 2020. "Insight into the fundamental trade-offs of diffusion MRI from polarization-sensitive optical coherence tomography in *ex vivo* human brain." *NeuroImage* 214: 116704.

Semi-Automated Segmentation of Infant Brainstem with OCT

**Samuel Blackman, **Seoyoon Kim, Erendira Garcia Pallares, † Dr. Caroline Magnain, † Dr. Lilla Zöllei
Laboratory for Computational Neuroimaging, A.A. Martinos Center for Biomedical Imaging, MGH

A.A. Martinos Center
For Biomedical Imaging
MASSACHUSETTS
GENERAL HOSPITAL
HARVARD
MEDICAL SCHOOL
MIT Massachusetts Institute of Technology

1. Background and Motivation

- Sudden infant death syndrome (SIDS) is the leading cause of infant mortality in the US, so identification of its biomarkers are key to investigate its causes.
- The core lesion of SIDS (CLS) is a set of medullar nuclei with abnormalities correlated with SIDS, currently being investigated for their role in homeostatic responses during sleep.
- The Ascending Arousal Network (AAN) modulates cortical awareness circuits.
- The related functions of CLS and AAN in sleep and awareness make them targets for the investigation of SIDS.

In vivo and even ex vivo MRI is insufficient for the identification of many regions, especially in the developing brainstem of infants, where SIDS-specific abnormalities must be found (Fig 1 right). MRI derives its contrast from myelination of axonal tracts, which is incomplete in the first year of life, while the smaller size of the infant brainstem compared to adults is also an obstacle.

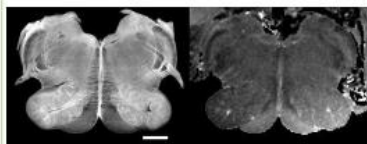
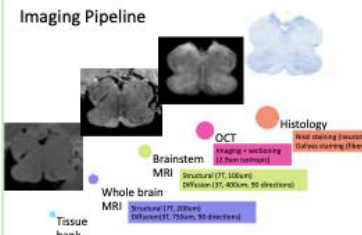


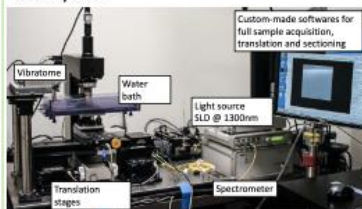
Figure 1: Left) Infant medulla imaged by OCT (2.9 μm lateral resolution), and right) by MRI (100 μm isotropic). Scale bar = 2 mm.

Optical Coherence Tomography (OCT)^[2] offers a powerful method to differentiate regions by how their components, cell bodies and fibers, scatter light, which is more independent of myelination, and leads to higher resolution. We are developing a high-resolution atlas of the infant brainstem, labelling ex vivo OCT volumes via manual segmentation and machine-learning-automated extrapolation^[3].

2. Preparation and Imaging



OCT system



- Image acquisition and sectioning fully automated
- Intrinsic contrast (no stains)
- Minimum deformation (imaging prior to sectioning)
- High resolution
- High contrast

For more detail on OCT and its applications, see the poster : "Optical Coherence Tomography (OCT) for Ex-vivo Human Brain Imaging"

3. Manual Segmentation

- Manual segmentation (Figure 2) of ex vivo OCT images of the infant brainstem was based on the Paxinos Atlas^[4] using FreeView, a visualization tool within FreeSurfer
- We labeled every fourth slice to provide interpolation program sufficient amount of data (Figure 3, top row)

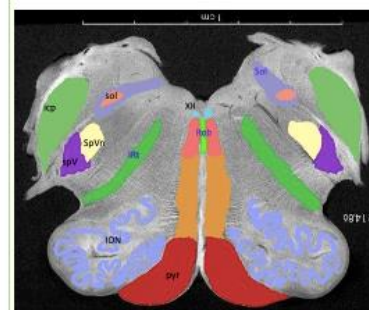


Figure 2: Manual segmentation of the infant medulla. Nuclei of the CLS : pyr (pyramidal tract), IRT (Intermediate Reticular zone), Sol (solitary nucleus) and Rob (Raphé Obscurus). Anatomical landmarks: ION (Inferior Olivary Nucleus), spV (Spinal Trigeminal Tract), SpVN (Spinal Trigeminal Nucleus), icp (Inferior Cerebellar Peduncle), XII (Hypoglossal nucleus).

4. Automated Segmentation: SmartInterpolation

The labelling process was sped up using SmartInterpolation^[4], an algorithm developed to automatically segment unlabeled slices across a volume using deep learning and Multi Atlas Segmentation (MAS) to complete our partially segmented volume (Figure 3, bottom row).

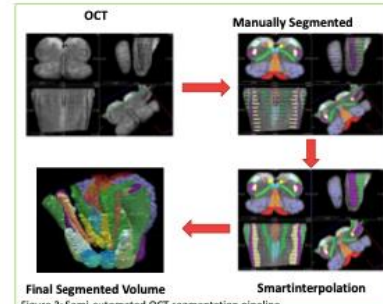


Figure 3: Semi-automated OCT segmentation pipeline

4. Future work: Registration

OCT volumes and their labels will be registered to their corresponding MR volumes for all datasets (Figure 4). We will use these datasets to create statistical brainstem atlases for age groups between 0 and 12 months. The atlases will also be used to create an automated segmentation tool for both *in vivo* and *ex vivo* MRI and will be distributed as part of FreeSurfer.

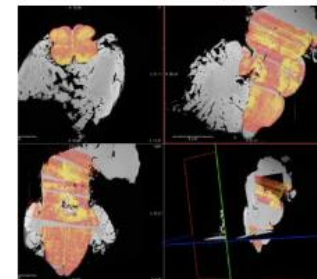


Figure 4: Visualization of a preliminary cross-registration of OCT volume onto the MR volume.

Key References

- [1] Edlow, B.L., et al., "Neuroanatomic connectivity of the human ascending arousal system critical to consciousness and its disorders", *J Neuropathol Exp Neurol*, 2012; 71(6): p. 531-46.
- [2] Huang, D. et al. "Optical Coherence Tomography", *Science* vol. 80, no. 254, pp.1178-1181, 1991.
- [3] Atzeni, Alessia, et al. "A probabilistic model combining deep learning and multi-atlas segmentation for semi-automated labelling of histology", *International Conference on Medical Image Computing and Computer-Assisted Intervention*. Springer, Cham, 2018.
- [4] Paxinos G., Huang X.F., et al., "Organization of Brainstem Nuclei", *The Human Nervous System*, pp. 260-327. Amsterdam: Elsevier Academic Press, 2012.

Acknowledgments

We thank Drs. Hannah Kinney, Robin Haynes and Luiz Fernando Ferraz da Silva for their collaboration. We also thank the National Institutes of Health for their support: the National Institute for Neurological Disorders and Stroke (R21NS106695) and the the Eunice Kennedy Shriver National Institute of Child Health & Human Development (R01HD102616, R21HD095338). Finally, this project has also been made possible in part by grant 2019-198101 from Chan Zuckerberg Initiative DAF, an advised fund of Silicon Valley Community Foundation.



HRMAS ^{13}C -NMR resolves real-time metabolic modulation in *C. difficile*

Aidan Pavao¹, Brintha Girinathan^{1*}, Johann Peltier^{2,3}, Pamela Altamirano Silva⁴, Bruno Dupuy², Leo L. Cheng⁵, Lynn Bry^{1,6}

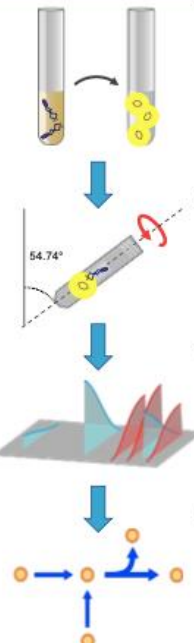


¹Massachusetts Host-Microbiome Center, Brigham & Women's Hospital, Harvard Medical School, Boston, MA; ²Laboratory of the Pathogenesis of Bacterial Anaerobes, CNRS 2001, Institut Pasteur, Université de Paris, F-75015, Paris, France; ³Institute for Integrative Biology of the Cell (IIBC), CEA, CNRS, Université Paris-Saclay, 91198, Gif-sur-Yvette cedex, France; ⁴Centro de Investigación en Enfermedades Tropicales, Facultad de Microbiología, Universidad de Costa Rica, San José, Costa Rica; ⁵Departments of Radiology and Pathology, Massachusetts General Hospital, Harvard Medical School, Boston, MA; ⁶Clinical Microbiology Laboratory, Department of Pathology, Brigham & Women's Hospital, Harvard Medical School, Boston, MA; *Current Address: Ginkgo Bioworks, Cambridge, MA

Introduction

Anaerobic metabolism supports complex host-microbiome interactions that strongly influence human health and disease. Yet, many critical components of anaerobe metabolism remain poorly described, despite their potential to inform clinical interventions. We present a new method to resolve the complex dynamics of anaerobic metabolism using HRMAS ^{13}C -NMR of living obligately anaerobic cells of the pathogen *Clostridioides difficile*. By tracking the time-dependent metabolism of ^{13}C -labeled metabolites, we discover the progression of pathway recruitment and integration of carbohydrate and amino acid metabolism with reactions supporting redox, energy generation and cellular nitrogen balance. Findings have informed new metabolic targets to counter *C. difficile* disease.

Methods



1. Cell and media preparation
 - a. *C. difficile* ATCC43255 ΔPaLoc is grown in BHIS liquid culture
 - b. Cells washed in PBS to prevent carry-over of media components
 - c. 10E5 cells added to defined media containing a ^{13}C -labeled carbon source
2. HRMAS ^{13}C -NMR
 - a. ^1H and ^{13}C NMR spectra of growing cells captured over 48 hours
 - b. $^1\text{H}/^{13}\text{C}$ HSQC, ^1H COSY, and ^{13}C COSY spectra acquired to identify ^{13}C -labeled metabolites
3. Spectral processing
 - a. Spectra subjected to line-broadening, Fourier transform, phase correction, chemical shift calibration, and trimming in NUTS
 - b. Metabolite peak trajectories traced and integrated in MATLAB
4. Metabolic modeling
 - a. Integrated NMR signal converted to concentration estimates
 - b. FBA model solution calculated using the COBRAPy toolbox in python with estimated concentration rates of change as uptake and secretion constraints

HRMAS ^{13}C NMR of U- ^{13}C Glucose

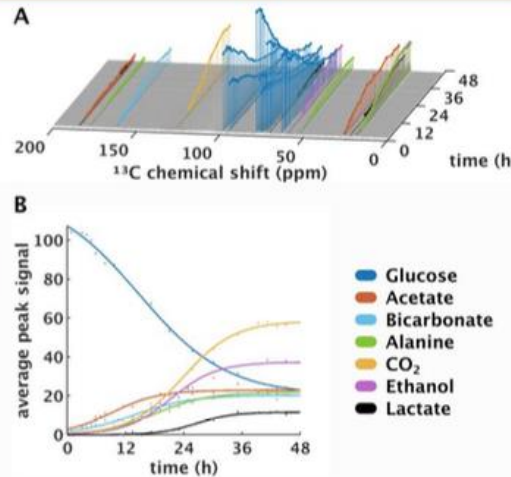


Figure 1—HRMAS ^{13}C NMR resolves real-time metabolism of U- ^{13}C glucose by *C. difficile*. (A) ^{13}C -NMR spectrum time series stack plot. X-axis shows the ^{13}C chemical shift; Y-axis the time in hours, and Z-axis the ^{13}C normalized signal. Inset key indicates the signal for individual carbons within the detected compounds. (B) Average peak signal of detected ^{13}C compounds (Y-axis) over time (X-axis) and logistic curve fit. Individual points were normalized by the number of ^{13}C carbons per compound.

C. difficile Metabolic Network

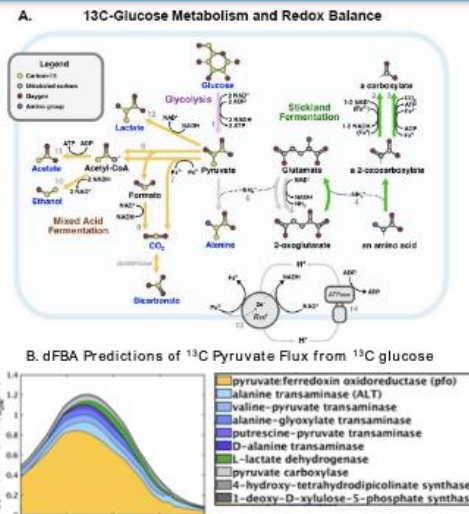


Figure 3—Metabolic pathways of *C. difficile* explain the time-dependent modulation of metabolism observed in HRMAS ^{13}C NMR studies. (A) Glycolytic and mixed-acid fermentation of ^{13}C glucose is redox- and nitrogen-coupled with Stickland amino acid fermentation via alanine production. (B) dFBA predictions of reactions driving pyruvate flux. X-axis shows time in hours, Y-axis shows predicted pyruvate flux in mmol/gram of dry weight biomass/hour. Inset indicates the predicted enzymatic reactions.

HRMAS ^{13}C NMR of U- ^{13}C Proline

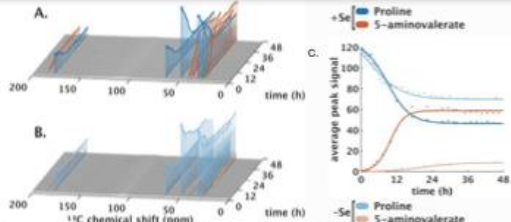


Figure 2—HRMAS ^{13}C NMR reveals dependence of Stickland proline metabolism on selenium concentration. Surface plots of ^{13}C -NMR spectra for reactions containing U- ^{13}C proline with (A) 0.1 μM sodium selenite or (B) in selenium-deficient media. (C) Average peak signals over time of proline and the dominant fermentation metabolite 5-aminovalerate in trace (light) and 0.1 μM sodium selenite (dark) reveal increased proline fermentation to 5-aminovalerate in the presence of selenium, a required metal ion for the proline reductase.

Conclusions

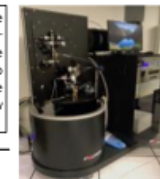
- HRMAS ^{13}C NMR provides a powerful new approach to elaborate the time-dependent progression of anaerobe metabolism, including of reductive and oxidative anaerobic fermentation pathways
- Production of ^{13}C -alanine from ^{13}C -glucose provides an ammonia sink to accommodate amino acid fermentation, serving as a critical integration point between carbohydrate and amino acid metabolism
- Comparative studies of proline fermentation in the presence and absence of selenium demonstrate assessments with defined media formulations
- Findings informed exchange constraints in a metabolic model of *C. difficile*, identifying alanine and electron carrier pools as critical metabolic integration points in energy flow and biomass expansion
- HRMAS NMR resolves complex interactions in anaerobic metabolism and informs new metabolic and gene-level targets to counter *C. difficile* infections

Hyperpolarized Metabolic Imaging by Dissolution Dynamic Nuclear Polarization Technique

David Guarin^{*[1]}, Erin Hardy^[2], Yi-Fen Yen^[3]

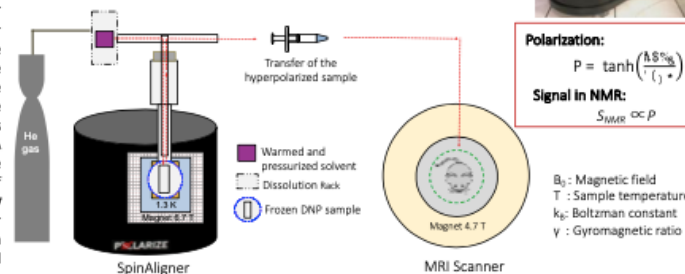
[1] Athinoula A. Martinos Center for Biomedical Imaging, Department of Radiology, Massachusetts General Hospital

*email: dguarinbedoya@mgh.harvard.edu



Abstract: Recent advancement in dissolution Dynamic Nuclear Polarization (d-DNP) technique has enabled a new way to non-invasively image metabolic disorders, cardiac metabolism, and cancer treatment effect. Experiments performed in the Martinos Center with hyperpolarized ¹³C-pyruvate have achieved signal enhancements of approximately 80,000, representing polarizations of above 50 %. With such high polarization, we can obtain metabolic images of different organs in living animals. Other ¹³C-compounds can also be hyperpolarized and used as contrast agents to study different aspects of metabolism *in-vivo*, and to study dynamic processes with ¹³C MRI. Other isotope labels such as ¹⁵N and ³¹P can also be hyperpolarized. We invite collaborators to explore this new research frontier to discover new hyperpolarized contrast agents and new applications.

d-DNP methodology: Dynamic Nuclear Polarization (DNP) is a powerful method for enhancing the polarization of nuclear spins with the aim of boosting weak nuclear magnetic resonance (NMR) signals [3]. In the DNP technique, the sample is cooled down to cryogenic temperatures in the presence of a constant magnetic field. In this condition, electrons polarization is almost 100%. A microwave irradiation is used to transfer the large polarization of unpaired electrons to the nuclei of interest, therefore **increasing the signal intensity by a factor of 10⁴** [4]. When a maximum nuclear polarization is attained, the sample is dissolved in a warmed buffer and transferred to a conventional MRI scanner. This technique is called Dissolution DNP (d-DNP) [3].

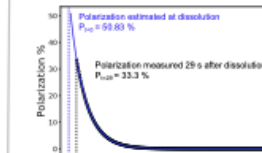
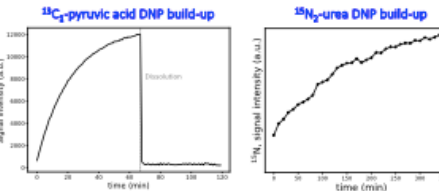


Sample preparation and polarization in solid state: The analyte to be hyperpolarized is formulated with particular compositions optimized for DNP. Some requirements for hyperpolarization to occur are:

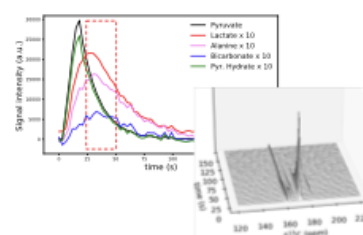
Sample composition for DNP[4]:

- Analyte:** ¹³C-labelled molecules with long T₁ (carbonyl moieties, ketone carbons).
- Radicals:** Molecule or ion with unpaired valence electrons. (Trityl derivatives, Amupol, TEMPOL)
- Glassy-agent:** Required for the sample to solidify as solid glass while frozen (Glycerol, DMSO, Ethanol, etc.)

The hyperpolarization process is monitored with NMR to observe the polarization build-up. Multiple nuclear species (¹³C, ¹⁵N, ³¹P) can be hyperpolarized and monitored in solid state.

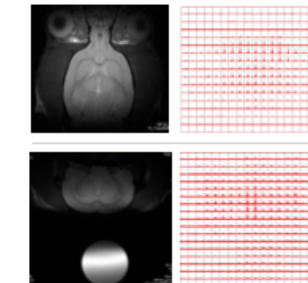


Achievable liquid state polarization: The d-DNP setup was tested on samples containing [1-¹³C]pyruvic acid to assess the liquid-state polarization after transferring to the MRI scanner. Enhancements of ~ 80,000 representing ~ 50 % of polarization at dissolution were obtained with the set-up at the Martinos Center. T₁ relaxation time was 74.9 s at 4.7 T.



In-Vivo dynamic spectroscopy: The first *in-vivo* experiments were performed on living rats by monitoring the signal evolution of the hyperpolarized pyruvate and its downstream metabolic products. A surface coil tuned to ¹³C frequency was positioned on the rat brain to detect the ¹³C signal of the different metabolites. Multiple metabolic products, such as lactate, alanine and bicarbonate, were observed!

In-Vivo metabolic imaging:



References:

- (1) Almgren, A.; Goldman, M., Rep. Prog. Phys. 1978, 41, 395–467.
- (2) Andersen-Jensen, et al. PNAS U. S. A. 2003, 100, 6158–63.
- (3) A. Gram G. Hanson, et al. Nat. Acad. Sc 100, 10158–10163(2003).
- (4) E. M. Webber et al. Angew. Chem. Int. Ed. (2018) 17, 5171 –5175.

Advantages of d-DNP:

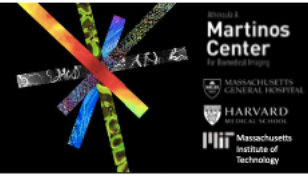
- Increased signal to noise ratio (SNR) allows fast detections of X-nuclei .
- No background signal *in-vivo* (use of nuclear species with low natural abundance)
- Possibility to record images of dynamic processes (metabolism, perfusion, etc.)

Revealing myelin water diffusivity and axon diameter using magnetization transfer, T_2 relaxation, and diffusion tensor imaging (MTT2-DTI)

Hong-Hsi Lee^{1,2}, MD, PhD; Dmitry S Novikov², PhD; Els Fieremans², PhD; Jiangyang Zhang², PhD

¹ Athinoula A. Martinos Center for Biomedical Imaging, Department of Radiology, Massachusetts General Hospital, Charlestown, MA

² Center for Advanced Imaging Innovation and Research (CAI2R), Department of Radiology, New York University School of Medicine, New York, NY



Introduction

- In brain tissues, diffusion MRI (dMRI) signals originate from multiple components, such as axon water (intra-/extra-axonal water) and myelin water (water in-between myelin sheath).
- Measuring myelin water signals, especially its diffusion properties, provides important insights of organization and integrity of myelin but remains challenging as myelin water has shorter T_2 value (<20ms) and contributes less to the overall MR signals than axon water [1,2].
- To robustly estimate diffusion properties of myelin water, we separated myelin water signals from others using a selective short-echo-time acquisition, combining magnetization transfer (MT), T_2 relaxation, and diffusion tensor imaging (DTI).
- We demonstrate the feasibility using data acquired from ex vivo mouse brains and further investigate using myelin water diffusivity to estimate axon size.

Theory: Signal decomposition

- We assumed that MR signals in the brain white matter (WM) come from two components: myelin water and axon water.
 - In MT, T_2 relaxation, and DTI (MTT2-DTI), the diffusion weighted (DW) signal is modeled as
- $$(\pm) = \pm \cdot \exp\left(-\frac{\text{TE}}{T_{2m}}\right) \cdot m() + (1 - \pm) \cdot \exp\left(-\frac{\text{TE}}{T_{2a}}\right) \cdot a(), \quad (1)$$
- where TE is the echo time, T_{2m}/T_{2a} are T_2 values of myelin and axon water, and $S_m(b)/S_a(b)$ are their DW signals. The $x = 0$ and $x = 1$ denote the signal weighting of myelin water with and without MT.
- Incorporating T_2 and MT enables robust decomposition of DW signals in each component using Eq. (1) and estimation of parameters (T_{2m}, T_{2a}, f).
 - Fitting DTI [3] to compartmental DW signals yields compartmental diffusion metrics: axial/radial mean diffusivity (AD/RD/MD) and fractional anisotropy (FA) with subscript "m" and "a" denoting myelin and axon water.

Theory: Axon diameter estimation

- Myelin sheath has a concentric lamellar structure with a radial periodicity ~15 nm in brain [4].
- We simplify the diffusion in-between two adjacent lamellae of myelin sheath as 1-dimensional diffusion around a circle of radius r . The RD due to diffusion of myelin water is given by

$$RD_{m,\perp}() = \frac{1}{2} \cdot \frac{r^2 \tau_{in}^2}{\delta^2(t-\frac{d}{2})} \left[2 \cdot \frac{\delta}{t_{in}} - 2 + 2 \cdot \frac{\frac{d}{2}}{t_{in}} + 2 \cdot \frac{\delta}{t_{in}} - \frac{\frac{d}{2}-\delta}{t_{in}} - \frac{\frac{d}{2}+\delta}{t_{in}} \right], \quad (2)$$

with diffusion time t and gradient pulse width d of pulsed-gradient sequence, correlation time $t_{in} = r^2/D_{m0}$ and intrinsic diffusivity D_{m0} of myelin water.

Approximating $D_{m0} = 3 \mu\text{m}^2/\text{ms}$ and neglecting fiber dispersion, we translate the myelin water RD_m into an axon size estimation r .

Methods: Ex vivo MRI

- To estimate T_{2m} , T_{2a} , and f , we performed short-echo-time spin-echo acquisitions of varying TEAs = 2-82 ms with and without MT preparation in an ex vivo mouse brain on a Bruker 7T scanner, measuring signals $S(x_\perp, \text{TE}, b = 0)$ and $S(x_\perp, \text{TE}, b = 0)$.
- To decompose compartmental DW signals, $S_m(b)$ and $S_a(b)$, we performed diffusion measurements of 4 non-diffusion-weighted-images (non-DWIs, $b = 0$) and 30 DWIs of b-value $b = 0.9 \text{ ms}/\mu\text{m}^2$ using TE₁ = 10 ms or TE₂ = 30 ms with and without MT preparation, measuring signals $S(x_\perp, \text{TE}_1, b)$, $S(x_\perp, \text{TE}_1, b)$, $S(x_\perp, \text{TE}_2, b)$, $S(x_\perp, \text{TE}_2, b)$.
- TR = 2000ms, resolution = $0.125 \times 0.125 \times 1.5 \text{ mm}^3$, radial center-out trajectory.

Results

- Fig. 1 shows the feasibility of MTT2-DTI, which generate separate T_2 maps for axon and myelin water, and myelin water fraction (~20% in WM).
- Using the extra dimension in T_2 and MT contrasts, we de-composed the diffusion metrics in each compartment (Fig. 2).
- The MD and RD is higher in axon water, and the FA is higher in myelin water (Fig. 3).
- In the trigeminal nerve (Fig. 4), the axon diameter estimate ~3 μm shows a gradient pattern (larger in medial part and smaller in lateral part), consistent with histology [5].

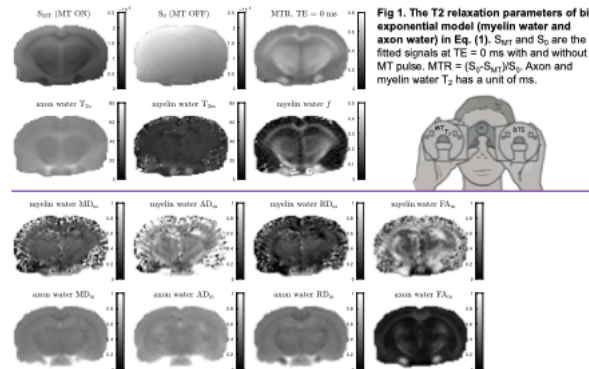


Fig 1. The T_2 relaxation parameters of bi-exponential model (myelin water and axon water) in Eq. (1). S_MT and S_0 are the fitted signals at TE = 0 ms with and without MT pulse. MTR = $(S_0 - S_MT)/S_0$. Axon and myelin water T_2 has a unit of ms.

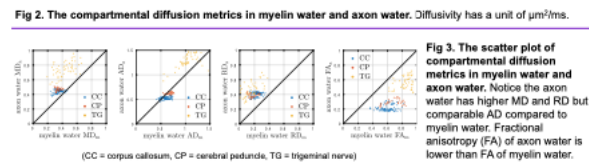


Fig 2. The compartmental diffusion metrics in myelin water and axon water. Diffusivity has a unit of $\mu\text{m}^2/\text{ms}$.

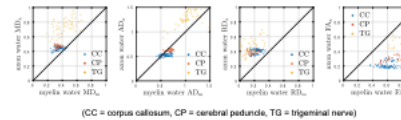


Fig 3. The scatter plot of compartmental diffusion metrics in myelin water and axon water. Notice the axon water has higher MD and RD but comparable AD compared to myelin water. Fractional anisotropy (FA) of axon water is lower than FA of myelin water.

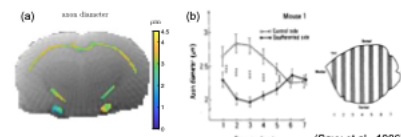


Fig 4. Axon diameter estimation based on radial diffusivity of myelin water and Eq. (2). (a) In the trigeminal nerve, the diameter estimate ~3 μm shows a gradient pattern (larger in medial part and smaller in lateral part), consistent with the (b) histological observation [5]. (Savy et al., 1986)

Discussion and Conclusions

- Combining multiple MR contrasts, we decompose diffusion metrics in myelin and axon water in a mouse brain.
- Compared to previous studies [1,2], the combination of T_2 and MT contrasts with short TE acquisition provides unique advantages in separating myelin water signals from axon water signals.
- The compartmental RD in myelin water offers axon diameter estimates at low b-value, alleviating the need of strong gradient & high slew rate for conventional diameter mapping [6].
- Applying multiple b-values, we can potentially factor out the effect of fiber dispersion on diameter mapping.
- Future work will focus on limitations of MTT2-DTI, including lack of sophisticated modeling of MT effect.

References:

- Andrews, T. J., Osborne, M. T., & Does, M. D. (2006). Magnetic Resonance in Medicine, 56(2), 381-385.
- Avram, A. V., Guidon, A., & Song, A. W. (2010). NeuroImage, 53(1), 132-138.
- Basser, P. J., Mattiello, J., & LeBihan, D. (1994). Journal of Magnetic Resonance, Series B, 103(3), 247-254.
- Raine, C. S. (1984). In Myelin (pp. 1-50). Springer, Boston, MA.
- Savy, C., Margules, S., Solaro, A., Wehrle, R., Verhey, R., & Farkas-Bargeron, E. (1986). International journal of developmental neuroscience, 4(1), 1-12.
- Veraart, J., Nunes, D., Rudrapatna, U., Fieremans, E., Jones, D. K., Novikov, D. S., & Shermesh, N. (2020). eLife, 9, e49855.

The “RF-EEG Cap”: a technological solution for high sensitivity whole-head concurrent TMS/EEG/fMRI experiments at 3T

Lucia Navarro de Lara¹, Padma Sundaram¹, Lena Nohava², Elmar Laistler², Mohammad Daneshzand¹, Jason Stockmann¹, Jyrki Ahveninen¹, Lawrence L. Wald¹ and Aapo Nummenmaa¹

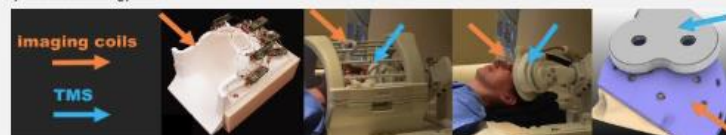
¹Athinoula A. Martinos Center for Biomedical Imaging, Massachusetts General Hospital, Harvard Medical School, Boston, MA; ²High Field MR Center, Center for Medical Physics and Biomedical Engineering, Medical University of Vienna, Vienna, Austria; Department of Psychiatry, Massachusetts General Hospital,



Motivation

Combining TMS/fMRI/EEG offers the next-generation capabilities for causal-functional mapping of the human brain circuits in a non-invasive way. However, the triple combination presents technological challenges especially due to the lack of dedicated hardware (see Fig.1 Column 1-3). Feasibility of concurrent human TMS/EEG/fMRI measurements at 3T has been recently demonstrated^{1,2}.

However, the presented data were acquired either with the body coil (extremely low-sensitivity) or a birdcage coil (Fig.1 column 2). Moreover, no parallel imaging acquisition methods^{3,4,5} were used due to the lack of multichannel RF-coils, limiting the spatiotemporal resolution of the acquisition. Nevertheless, these results rigorously demonstrate the basic feasibility and safety of the technology.



capabilities/coil	32/64-channel head array	birdcage coil	dedicated thin RF coil array	Proposed “RF-EEG Cap”
commercial TMS compatibility	✗	~*	✓	✓
full head coverage	✓	✓	✗	✓
high sensitivity	✓	✗	✓	✓
parallel imaging capabilities	✓	✗	✓	✓
neuronavigation in bore	✗	✗	✓	✓

*limited applicability in some regions

Fig. 1. Summary of available instrumentation for MR acquisitions and its capability for online TMS/fMRI acquisitions.

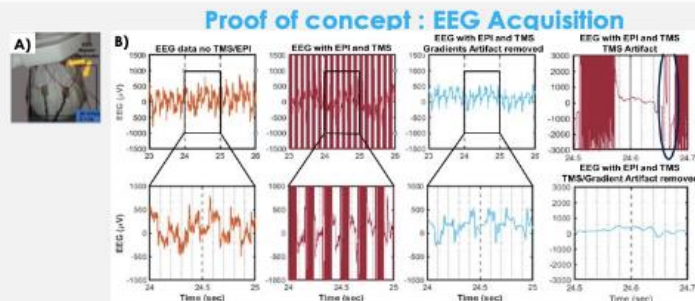


Fig. 4. A) Set up used to produce synthetic EEG signal on the phantom. TMS was applied horizontally over the center of the phantom. B) First column shows acquired synthetic EEG data from the phantom in the bore when no MR imaging and TMS stimulation were performed in an interleaved way. The plots show all artifacts contaminating the EEG signal. Third column shows acquired synthetic EEG data acquired after removing gradient and TMS artifacts. Fourth column shows a more detailed view of the TMS artifact and how it was removed by post-processing.

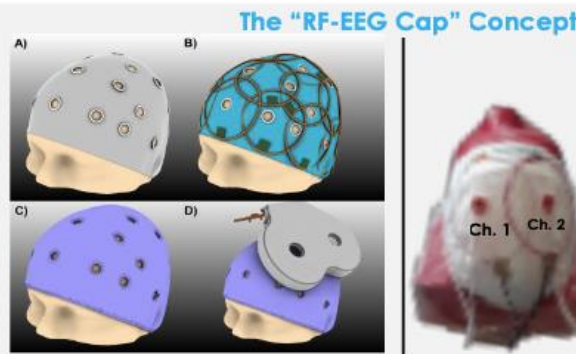
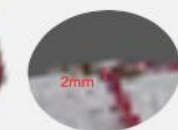


Fig. 2 The proposed RF-EEG Cap (in blue (B)) is thought to be attached to a commercial EEG Cap (above in grey, (A)). We plan to use flexible self-resonant coaxial cables^{6,7} as technology to build the RF loops, having 24 channels. The RF Elements should be covered with another cap (in purple (C and D)) to isolate all components from the subject. The thickness of the whole assembly should be about 5mm.

The “RF-EEG Cap” Concept

Fig. 3. We have built a 2-channel prototype (shown in the picture) to assess the feasibility of the proposal. The prototype consists of two RF channels integrated with 2 bipolar EEG electrodes. The thickness of the RF coil is 2mm determined by the PIN diode (see figure below).



Proof of concept: MR Imaging

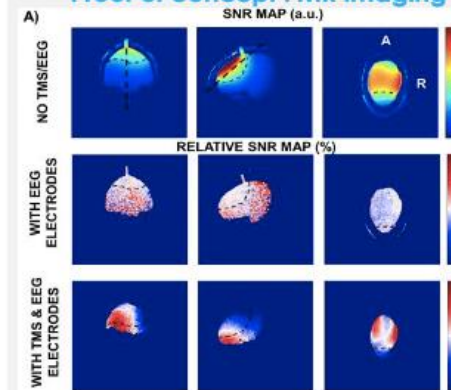


Fig 5. A) Top SNR maps of 3 slices of the phantom using the prototype without EEG electrodes and TMS. The black dashed lines in the coronal slices indicate the position of the transversal slice. Center. Relative change of the SNR in percentage when placing the EEG-electrodes on the prototype. Bottom. Relative change of the SNR in percentage when placing the electrodes and the TMS coil on the prototype. Dashed lines show the region where the built prototype has an acceptable SNR.

References: 1: Peters et al., J. Neurophysiol. 109, 1214–1227 (2013) 2: Peters et al., Commun. Biol. 3, 1–11 (2020); 3: Pruessmann et al., Magn. Reson. Med. 42, 952–62 (1999) 4: Griswold et al., Magn. Reson. Med. 47, 1202–10 (2002) 5: Auerbach et al., Magn. Reson. Med. 69, 1261–7 (2013) 6: Zhang et al. Nat. Biomed. Eng. 2, 570–577 (2018); 7: Rustenberg et al., Magn. Reson. Med. 83 (3), 1135–1146 (2020); 8: Navarro de Lara et al. Magn. Reson. Med. 74, 1492–1501 (2015) Funding: R01MH111829. MGH/Martinos : P41EB015896, S10RR019307, S10RR019254, S10RR023004.

Conclusion

From the results of these experiments and additional ones such as benchmark testing, B0 maps and fMRI timeseries stability (not shown here) we conclude that :

- the flexible coaxial RF technology is a feasible choice to build the proposed “RF-EEG Cap”. The detuning effect of the TMS on the resonance of the RF elements was found to be less than 0.4MHz compared to 4-5MHz when using standard copper wire coils⁸.
- Observed SNR effects are minimal when applying the EEG electrodes and only TMS B_{1+} effect is visible when applying both.

The minimal effects observed on the SNR, B0 maps, EEG quality signal and fMRI volumes and timeseries justify the further development of the “RF-EEG Cap” to enable high quality data acquisition for concurrent TMS/EEG/fMRI experiments.

Manual Quality Control of 5,764 Structural MRI Scans in the Adolescent Brain Cognitive Development Study



MASSACHUSETTS
GENERAL HOSPITAL

Safia Elyounssi¹, Dylan Hughes¹, Keiko Kunitoki^{1,2}, MD, Oren Bazer¹, & Joshua Roffman^{1,2}, MD

¹Massachusetts General Hospital

²Harvard Medical School



Results, cont.

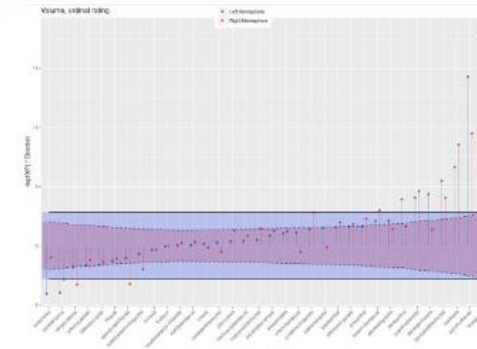


Figure 4. Manhattan plot demonstrating effect of rating on volume. Analyses were covered by age, sex, site, scanner, and ICV. Higher ratings tended to inflate volume. Threshold for multiple comparison are shown in the blue band (Bonferroni) and the purple band (FDR), both set to $p<.05$, corrected.

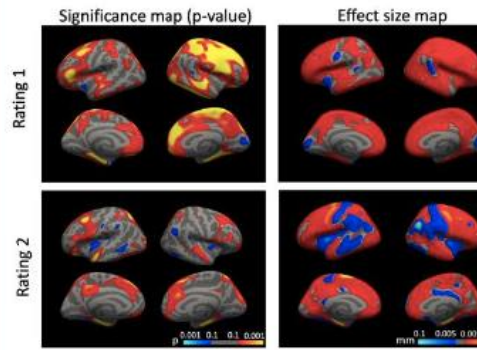


Figure 5. Paired analysis comparing cortical thickness before versus after manual edits. Upper: 55 samples with Rating "1". Lower: 10 samples with Rating "2". Positive values (red) represent areas before>after, and negative values (blue) represent areas after>before.

Conclusion

- ❖ Automated QC methods fail to detect meaningful artifact in most scans obtained at age 9-10, leading to substantial bias.
- ❖ These artifacts influence numerous structural MRI phenotypes across the brain surface and parenchyma. This may result in substantial risk for both type I and II error.
- ❖ Elimination of scans with poor global QC based on visual inspection can substantially improve signal-to-noise, but even so, manual edits – while even more time consuming – provide still more meaningful refinement, even among scans with the best ratings.
- ❖ These findings demonstrate the necessity of manual QC in brain MRI research studies involving children and have relevance for virtually all MRI analyses involving ABCD data.

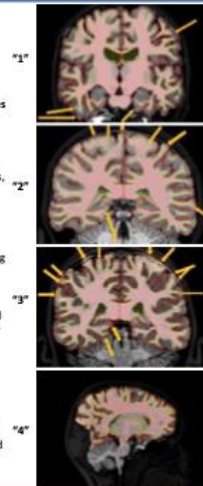
Introduction

- ❖ The Adolescent Brain Cognitive Development (ABCD) Study is a prospective, longitudinal brain imaging study made up of 11,878 children, aged 9-10, enrolled at 21 sites across the US.
- ❖ Participants will receive follow-up scans biennially for 10 years.
- ❖ With such a large cohort, investigators have been relying on automated quality control (QC) measures to filter out scans that could affect analyses.
- ❖ However, automated ratings may be insufficient to account for within-scan motion and other image artifacts commonly seen in studies of children.

Purpose: Conducting an in-depth, manual review of 5,764 structural MRI scans from 9-10-year-olds in the ABCD Study to determine the adequacy of automated QC and the impact of enhanced QC measures that rely on visualization and of cortical edits.

Methods

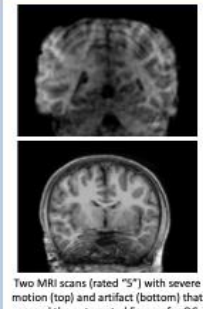
- Part 1:**
- ❖ 5,764 MRI scans that passed automated QC were individually viewed and rated using Freeview version 7.1.1.
 - ❖ Ratings from "1" (minimal artifacts & minimal editing needed) to "4" (very substantial artifacts & significant manual editing needed) were given to all scans [examples shown to the right].
 - ❖ "5" rating was given to scans from one of three categories: (1) unusable scans due to severe motion artifact, a broken image, or other artifact and field of view issues. (2) subjects with noted clinical abnormalities, or (3) subjects with cysts larger than 1mm³.



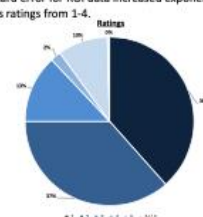
- Part 2:**
- ❖ Mean and standard error were calculated for regions of interest (ROI) (volume, surface area, thickness, and subcortical volume) for each rating group from 1 to 4 using standard Freesurfer parcellations.
 - ❖ Parallel ANOVAs determined effects of rating on ROI phenotypes (152 thickness, 68 area, 68 volume, 68 subcortical), covering for age, sex, site, scanner, and total intracranial volume (ICV). ROI analyses were corrected for multiple comparisons ($n=356$) using the False Discovery Rate. Additionally, effects of rating on ROI phenotype were visualized using vertex-wise linear models.

- Part 3:**
- ❖ 55 randomly selected MRI scans, all with the best rating ("1") were manually edited using FreeSurfer version 7.1.1 and Freeview. Paired t-tests compared mean and standard error for all pre- and post-edit ROI data, using FDR to correct for 356 comparisons.

Results



- ❖ Of the 5,764 scans, 2,215 (38.4%) were rated "1", 2,108 (36.6%) were rated "2", 749 (13.0%) were rated "3", 117 (2.0%) were rated "4", and 551 (9.6%) were rated "5".
- ❖ 24 scans (0.42%) could not be accessed and were not given a rating ("N/A").
- ❖ Standard error for ROI data increased exponentially across ratings from 1-4.



Results, cont.

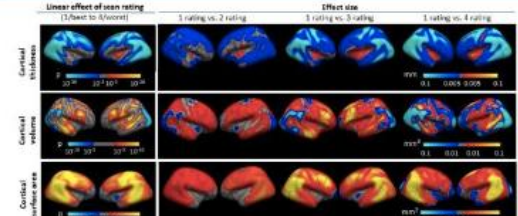


Figure 1. Effects of scan artifacts detected by manual review on structural MRI indices from 5,123 children ages 9-10 in the ABCD Study. Analyses were covaried by age, sex, scanner, and ICV. Of the 356 ANOVAs testing for differences in ROI by ratings, all but 41 demonstrated significant effects of QC ratings ($p<.05$, FDR), with higher ratings tending to deflate cortical thickness and to inflate volume and surface area.

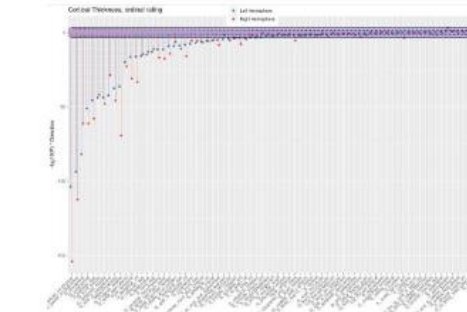


Figure 2. Manhattan plot demonstrating effect of rating on cortical thickness. Analyses were covaried by age, sex, site, scanner, and ICV. Higher ratings tended to deflate cortical thickness. Threshold for multiple comparison are shown in the blue band (Bonferroni) and the purple band (FDR), both set to $p<.05$, corrected.

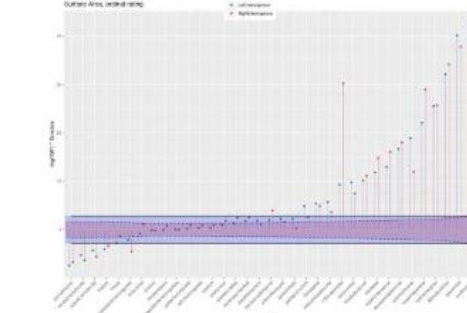


Figure 3. Manhattan plot demonstrating effect of rating on surface area. Analyses were covaried by age, sex, site, scanner, and ICV. Higher ratings tended to inflate surface area. Threshold for multiple comparison are shown in the blue band (Bonferroni) and the purple band (FDR), both set to $p<.05$, corrected.



Do increased arousals impair sleep-dependent memory consolidation in schizophrenia?

Rudra Patel^{1,3}, Dimitris Mylonas^{1,2,3}, Olivia Larson^{1,3}, Lin Zhu^{1,3}, Bryan Baxter^{1,2,3}, Dara S. Manoach^{1,2,3}

¹Department of Psychiatry, Massachusetts General Hospital, Boston, MA; ²Harvard Medical School, Boston, MA; ³A. A. Martinos Center for Biomedical Imaging, Charlestown, MA

Introduction

Sleep spindles are defining oscillations of NREM stage 2 (N2) sleep¹. Extensive research demonstrate that spindles mediate sleep-dependent memory consolidation².

Spindles are also thought to protect against arousals³.

In schizophrenia (SZ), reduced spindle activity correlates with reduced sleep-dependent memory consolidation⁴.

Does this correlation reflect the direct effects of reduced spindles on memory, or that reduced spindles lead to more arousals that disrupt memory consolidation?

To address this question, we examined if SZ patients have increased arousals that correlate with spindle density and sleep-dependent memory consolidation.

Methods

Participants: 26 SZ patients and 29 demographically matched healthy controls (HC) completed two nights of polysomnography (PSG).

	SZ (n=26)	HC (n=29)
M ± SD	M ± SD	
Demographics		
Age (years)	32 ± 8	30 ± 6
Sex	5F/21M	8F/21M
Mean parental education (years)	14 ± 3	15 ± 3
Symptom severity*	69 ± 14	
Sleep Quality[†]		
TST (min)	490 ± 106	499 ± 58
WASO (min)	33 ± 44	34 ± 27
Sleep Efficiency (%)	87 ± 14	90 ± 6

* Total score on PANSS

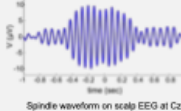
[†] Averaged across baseline and MST night

On the second night, participants were trained on the finger tapping motor sequence task (MST) before bed and tested the following morning. MST consolidation was calculated as the % change in correct sequences from the last 3 training trials to the first 3 test trials.

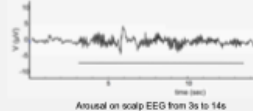


Methods (cont.)

Sleep spindle: Defining feature of N2 sleep seen on the EEG as brief (0.1 s) bursts of synchronous activity in the 12–15 Hz range¹. Identified using an automated spindle detector.



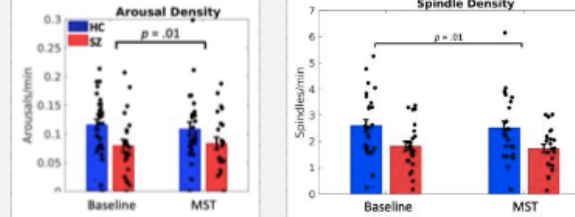
Arousal: An abrupt shift of EEG frequency that lasts at least 3s with at least 10s of stable sleep preceding the change⁵. Hand-scored blind to group using AASM criteria.



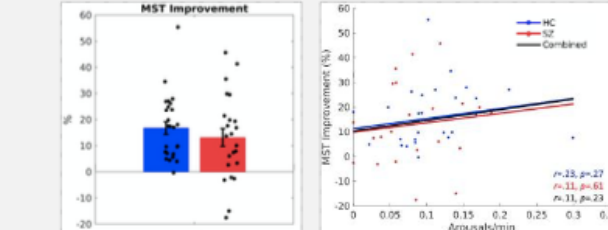
Arousal density was compared between groups using mixed effects models that included Group and Night as fixed effects and Subject as a random effect. To evaluate the relations of spindle density and MST consolidation with arousal density, we used linear regression models.

Results

SZ patients showed reduced arousal density ($p=.01$) and reduced spindle density ($p=.01$) compared to HC.

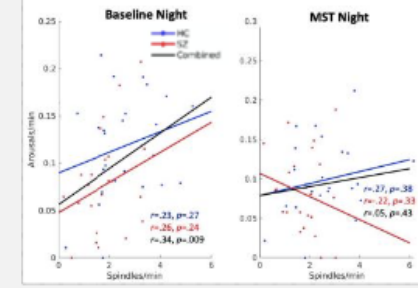


Overnight MST consolidation did not differ by Group, and arousal density did not significantly correlate with MST consolidation.



Results (cont.)

Increased spindle density correlated with increased arousal density in the baseline night ($p=.009$) regardless of group but not in the MST night, and this significant interaction ($p=.001$) was driven by a negative relation of spindles with arousals in SZ.



Conclusions

Summary: SZ patients did not show reduced sleep quality or increased arousals. Our findings do not support the hypothesis that arousals are related to overnight memory consolidation in SZ. The relations of spindle density with arousal density are consistent with a protective role of spindles for preserving sleep.

Future Directions: We plan to analyze data from a previous study in which SZ patients showed a significant deficit in sleep-dependent memory of MST consolidation to further exclude the possibility that increased arousals are culpable.

References

- Rechtschaffen, A., & Kales, A. (1968). A manual of standardized terminology, techniques and scoring system for sleep stages of human subjects.
- Gais et al. (2002). Learning-dependent increases in sleep spindle density. *Journal of Neuroscience*, 22(15), 6830-6834.
- de Gennaro, L., & Ferrara, M. (2003). Sleep spindles: an overview. *Sleep Medicine Reviews*, 7(5), 423-440.
- Wamsley et al. (2012). Reduced sleep spindles and spindle coherence in schizophrenia: mechanisms of impaired memory consolidation? *Biological Psychiatry*, 71, 154-161.
- Berry et al (2020). *The AASM Manual for the scoring of sleep and associated events: Rules, terminology and technical specifications*.

Neuroinflammation in Human Immunodeficiency Virus-Related Neuropathic Pain

Minhae Kim^{1,†}, Akila Weerasekera¹, Kelly Castro-Blanco¹, Yang Lin¹, Zeynab Alshelh¹, Angel Torrado-Carvajal^{1,2}, Shibani S. Mukerji³, Rajesh Gandhi⁴, Lauren Pollak⁵, Oluwaseun Akeju⁶, Burel Goodin⁷, Atreyi Saha¹, Vitaly Napadow¹, Robert R Edwards⁶, Eva-Maria Ratai¹, & Marco L Loggia¹

¹Department of Radiology, Athinoula A. Martinos Center for Biomedical Imaging, Massachusetts General Hospital (MGH), Harvard Medical School (HMS), Boston, MA, USA,

²Universidad Rey Juan Carlos, Madrid, Spain, ³Department of Neurology, MGH, HMS, Boston, MA, USA, ⁴Division of Infectious Diseases, MGH, HMS, Boston, MA, USA,

⁵Psychology Assessment Center, MGH, HMS, Boston, MA, USA, ⁶Department of Anesthesia, Critical Care and Pain Medicine, MGH, HMS, Boston, MA, USA,

⁷Department of Psychology, University of Alabama at Birmingham, Birmingham, AL, USA.

Introduction

BACKGROUND

Approximately 38 million people worldwide live with human immunodeficiency virus (HIV).

- HIV-associated sensory neuropathy (HIV-SN) is a common neurological complication of HIV and its treatment in people living with HIV (PLHIV).
- Neuropathic pain is a highly prevalent and debilitating symptom among PLHIV.
- Our group has previously provided evidence in support of a role of neuroinflammation in human chronic pain. We observed:
 - Elevations in the thalamic levels of the 18kDa translocator protein (TSPO), a neuroinflammatory marker, in chronic low back pain, using [¹¹C]-PBR28 positron emission tomography (PET)¹,
 - Elevations in the glial marker, myo-inositol (mIns), in patients with knee osteoarthritis, using ¹H magnetic resonance spectroscopy (MRS).²

STUDY AIM

In this study, we used simultaneous [¹¹C]-PBR28 PET/¹H-MRS to test the hypothesis that HIV-related neuropathic pain is also accompanied by elevations of TSPO and neuroinflammation.

Methods

SUBJECT SELECTION

- 9 PLHIV without neuropathic pain (PLHIV_{no pain});
- 11 PLHIV with neuropathic pain (PLHIV_{pain}; 6 on opioids, 5 not on opioids);
- 8 healthy volunteers (HC).

All PLHIV were on stable antiretroviral therapy and virally suppressed (plasma HIV RNA <200 copies/mL at screening).

Methods (cont.)

All participants were genotyped for the Ala147Thr polymorphism in the TSPO gene, which predicts binding affinity to [¹¹C]-PBR28.

All participants provided written informed consent, and the study was approved by the Mass General Brigham Institutional Review Board.

QUANTITATIVE SENSORY TESTING

A cuff was applied to the participants' right calf and its pressure gradually increased until reaching moderate pain (~40/100).

- Cuff pain ratings:** Average ratings obtained every 30 seconds during the 2-minute cuff application.
- Painful aftersensation ratings:** Average ratings obtained 15- and 30-seconds post-cuff removal.

IMAGING DATA ACQUISITION & PROCESSING

PET: Standardized uptake values normalized by whole brain signal (SUVR) were computed from 60-90 min post-[¹¹C]-PBR28-injection data, spatially smoothed (FWHM=8mm) and normalized to the MNI template. A T1-weighted volume (MEMPRAGE; TR/TE1/TE2/TE3/TE4 = 2530/1.64/3.5/3.36/7.22ms, flip angle=7°, voxel size=1x1x1mm³) was used for attenuation correction of PET data and spatial normalization to the MNI space.

MRS: ¹H-MRS data were collected using a PRESS sequence (TE/TR=30/1700ms, voxel size=20x20x20mm³) from the left thalamus and left insula, and metabolites were quantified using LCModel. Results are reported relative to the non-suppressed water signal.

Results

PET: Widespread TSPO signal in PLHIV vs. HC and elevated thalamic TSPO signal in PLHIV with neuropathic pain.

MRS: Insula mIns level difference in PLHIV_{pain} vs. HC.



Figure 1 (above). a) A cluster-corrected whole-brain voxel-wise analysis in PLHIV vs. HC (threshold: $z=2.3$). b) PLHIV_{pain} vs. PLHIV_{no pain} (threshold: $z=2$).

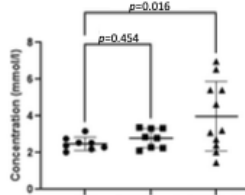


Figure 2 (left). Insula mIns level difference in the three cohorts (ANOVA; $p=0.037$). Post-hoc pairwise comparisons (Dunnett's test) showed the effect in HC vs. PLHIV_{pain} but not in HC vs. PLHIV_{no pain} ($p=0.016$ vs. 0.454, respectively).

CORRELATIONS IN PLHIV: Using TSPO genotype as a covariate, we observed positive correlations in 1) right thalamic SUVR & cuff pain ratings ($R^2=0.25$, $p=0.033$; ns in left), correcting for moderate pain threshold; 2) insula choline & left thalamic SUVR ($R^2=0.23$, $p=0.042$; ns in right); and 3) insula mIns & painful aftersensation ratings ($R^2=0.34$, $p=0.033$). Thalamic metabolites were not significantly correlated with thalamic SUVR (right $p\geq 0.629$, left $p\geq 0.524$).

Conclusion

Our findings suggest an association between HIV and widespread neuroinflammation, and between HIV-associated neuropathic pain and elevated thalamic TSPO signal and insula mIns levels. Further work in a larger sample size is necessary to corroborate these observations.

References

¹Loggia ML et al. 2015 Brain, ²Weerasekera A et al. 2021 Pain



SPAUING
REHABILITATION HOSPITAL



HARVARD
MEDICAL SCHOOL

ASSOCIATION BETWEEN TRIGEMINAL NERVE MICROSTRUCTURE AND CLINICAL CHARACTERISTICS IN MIGRAINE: AN ULTRA-HIGH FIELD 7 TESLA DIFFUSION TENSOR IMAGING STUDY

Tohyama S^{1,2}, Datko M^{1,2,3}, Brusafeiri L^{1,2}, Hyman M², Round K^{2,3}, Housman H², Le V⁴, Garcia RG^{1,2,5}, Gollub RL^{1,2,5}, Edwards RR^{1,6}, Rosen BR^{1,2}, Hadjikhani N^{1,2}, Cheng HT^{1,4}, Schuman-Olivier Z^{1,3}, Loggia ML^{1,2}, Napadow V^{1,2,6}

¹Harvard Medical School, Boston, MA, ²Martinos Center for Biomedical Imaging, Dept. of Radiology, Massachusetts General Hospital, Charlestown, MA,

³Center for Mindfulness and Compassion, Dept. of Psychiatry, Cambridge Health Alliance, Cambridge, MA, ⁴Dept. of Neurology, ⁵Dept. of Psychiatry, Massachusetts General Hospital, Harvard Medical School, Boston MA,

⁶Dept. of Anesthesiology, Perioperative and Pain Medicine, Brigham and Women's Hospital, Harvard Medical School, Boston MA



@SarasaTohyama

stohyama@mgh.harvard.edu

Introduction

Migraine, a highly prevalent chronic pain disorder, involves sensitization of the trigeminal nerve system.¹ Diffusion tensor imaging (DTI) studies have demonstrated microstructural alterations at the trigeminal nerve root in chronic pain conditions such as trigeminal neuralgia and temporomandibular disorder.^{2,3} However, the trigeminal nerve microstructure in migraine has not yet been adequately explored. We used ultra-high field (7 Tesla) DTI, allowing for improved spatial resolution, to evaluate the association between trigeminal nerve microstructural properties and clinical characteristics in episodic migraine.

Methods

Participants: We enrolled 16 patients with episodic migraine (15F, mean age \pm SD: 38.1 ± 13.5 years) diagnosed according to the latest ICHD-3.¹

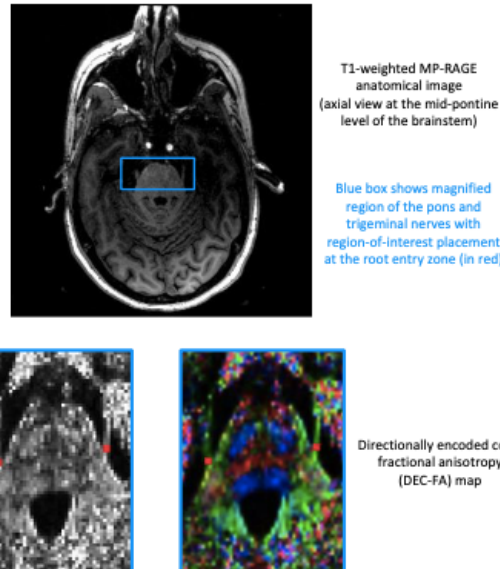
Clinical characteristics: All patients self-reported clinical characteristics of their condition, including migraine disease duration (years), number of headache days per month, average headache duration (hours), average headache pain intensity (0-10: no pain (0) to most intense pain imaginable (10)), and interictal phase (0-100: timing of DTI assessment relative to preceding (0) versus subsequent (100) attacks).

Image acquisition & processing: Each patient underwent a 7T diffusion-weighted imaging scan (64 directions, $b=1,000$, 1mm isotropic voxels). Images were corrected for susceptibility, eddy current, and motion-induced distortions, followed by diffusion tensor estimation and scalar map calculation in FSL.⁴

Trigeminal nerve root analysis: DTI metrics of fractional anisotropy, axial, radial, and mean diffusivity were manually extracted from the root entry zone of both trigeminal nerves (at the mid-pontine level of the brainstem) in 3D Slicer. Spearman's rank-order correlations were performed to determine the association between each DTI metric and clinical measure.

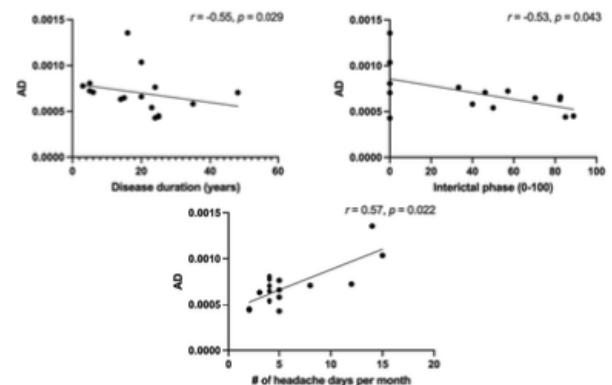
Trigeminal Nerve Visualization

Ultra-high field 7T DTI delineates the small-scale structure of the trigeminal nerve roots



Results

Axial diffusivity (AD) is significantly correlated with disease duration, interictal phase, and the number of headache days per month



Conclusions

Trigeminal nerve root AD, a metric of axonal integrity, is correlated with disease duration, interictal phase, and the number of headache days per month. These preliminary results suggest both trait-like (i.e. disease duration, severity) and state-like (i.e. interictal phase) links to trigeminal nerve microstructure. Trigeminal nerve root remodeling may be an important aspect of the dynamics underlying migraine pathophysiology.

Supported by the National Institutes of Health, National Center for Complementary and Integrative Health (P01-AT009965) and the Canadian Institutes of Health Research (MFE176554).

National Center for
Complementary and
Integrative Health

CIHR IRSC
Canadian Institutes of Health Research

References

- [1] ICHD-3. 2018. Cephalgic Disorders [1]-[23]; [2] DeBouta et al. 2014. *Pain* 155 [1]:37-44;
[3] Moseley et al. 2012. *Pain* 153 [7]:1467-1477; [4] Jenkins et al. 2012. *NeuroImage* 62 [2]:1785-1790.

EEG hyperscanning in patient-clinician dyads during pain treatment

Anzolin A¹, Grahl A¹, Isenburg K¹, Toppi J⁵, Ciaramidaro A⁶, Barton Zuckerman M¹, Yücel M⁷, Ellingsen DM^{1,2}, Astolfi L⁵, Kapchuk TJ⁴, Napadow V^{1,3}
¹Martinos Center for Biomedical Imaging, Department of Radiology, Massachusetts General Hospital, ²Department of Psychology, University of Oslo, Norway, ³Pain Management Center, Department of Anesthesiology, Brigham and Women's Hospital, ⁴Program in Placebo Studies, Beth Israel Deaconess Medical Center, Harvard Medical School, ⁵Sapienza University of Rome, ⁶University of Modena and Reggio Emilia, ⁷Boston University

Contact:
 anzolin@mcg.harvard.edu
 @ale_anzolin

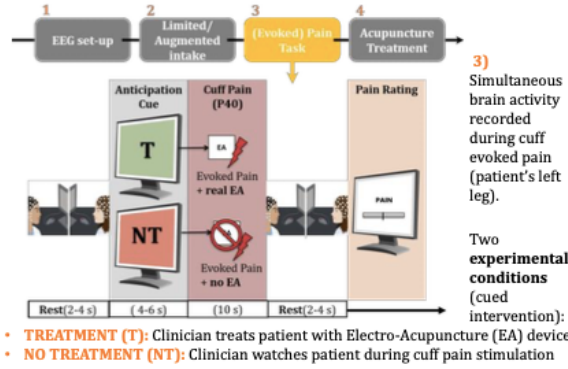



1. Background

- Social Interactions can significantly impact the perception and experience of pain
- The therapeutic alliance within the clinician-patient relationship is a key aspect of therapy in clinical pain populations
- Brain mechanisms underlying therapeutic alliance requires two person methods in an ecologically valid context EEG/fMRI hyperscanning
- Hypothesis: the interaction style between chronic pain patients and clinicians modulates neural activity and synchrony, influencing effectiveness of the clinical treatment, pain relief and placebo analgesia

2. Experimental Design

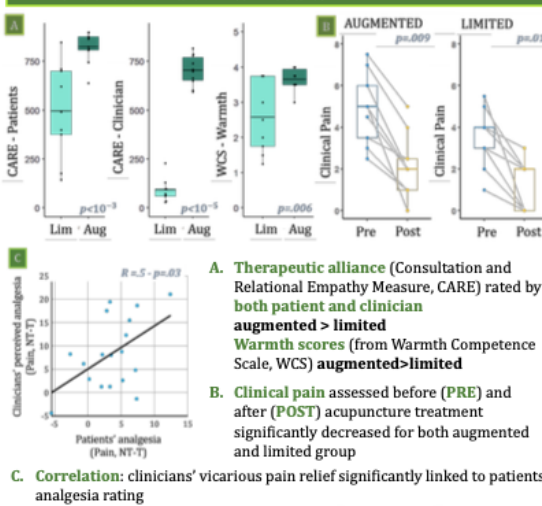
- 64-channel EEG net placed on the head of the clinician and the patient
- Clinician was trained to follow an intake protocol during interaction with the patient that was either AUGMENTED (friendly and attentive relationship with active listening and personalized content) or LIMITED (neutral and impersonal, with an intentionally narrowly-focused clinician)



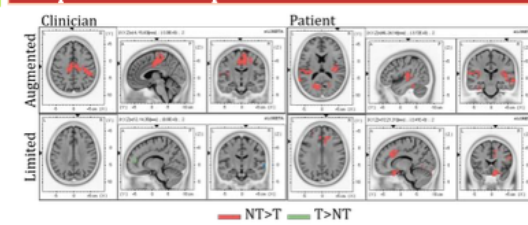
7. Conclusion

- Brain and behavioral mechanisms across the patient-clinician dyad are significantly affected by interaction style. AUGMENTED context characterized by i) reduction in low back pain; ii) increased therapeutic alliance and perceived warmth; iii) stronger insula and mid-cingulate Θ power during observed vs. treated pain, suggesting increased empathy processing when withholding treatment.
- EEG hyperscanning is an ecologically valid approach to identify inter-brain networks whose density and directionality within the dyad is altered by treatment and clinical context, highlighting new brain mechanisms linking therapeutic alliance, placebo analgesia and chronic pain therapy.

4. Behavioral and clinical results



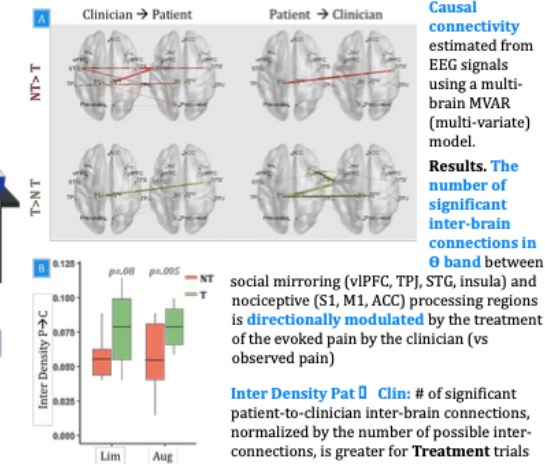
5. Spectral Brain Maps



Brain EEG power in Θ band during cuff pain interval

AUG → insula and mid-cingulate → stronger empathy context (both clin. and pat.)
 LIM → middle frontal gyrus, precuneus, insula, mid-cingulate (in pat. only) → greater nociception for NT?

6. Brain-to-Brain connectivity



Computational targeting and dosing in navigated multichannel TMS arrays

Mohammad Daneshzand¹, Sergey N. Makarov^{1,2}, Lucia I. Navarro de Lara¹, William A. Wartman², Tommi Raji¹, and Aapo Nummenmaa¹

¹Athinoula A. Martinos Center for Biomedical Imaging, Dept. of Radiology, Harvard Medical School, Massachusetts General Hospital, Charlestown, MA, USA.
²Department of Electrical and Computer Engineering, Worcester Polytechnic Institute, Worcester, MA, USA.



Multichannel TMS

Multichannel TMS technology^{1,2} allows stimulation of multiple target sites without physical movement of the coils under electronic control.

Key features on the computational targeting and dosing of stimulation using a multichannel TMS array approach:

- The impact of TMS coil element types
- Head movements
- Neuronavigation tracking errors

Here we interfaced our real-time computational engine³ with a commercial neuronavigation system to demonstrate practical applicability of the multichannel TMS method.

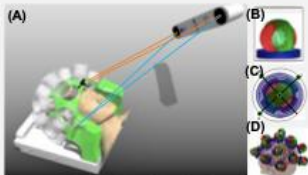


Fig.1. (A) A schematic illustration of the multichannel TMS/MRI system neuronavigation. (B,C,D) A computational model of 3-axis array surrounding the subject's head.

Accuracy metrics



Fig.2. (A) A 4x4 TMS array on a sphere model allows for fast and flexible E-field shaping without the need for manual or robotic repositioning of the coils. Adjusting the coils current intensities and polarities allows for generation of any desired E-field pattern and orientation. (B,C) The accuracy metrics are defined on 20000 target locations with three different angles.

The induced E-field of the multichannel TMS system was calculated on a 2-layer sphere model with inner and outer sphere radii of 8 and 10 cm respectively. The coils array was placed at the outer sphere surface while the E-field was measured at the inner sphere boundary.

- Localization error:** the Euclidean distance between the desired target and the location of the maximum of the induced E-field from the multichannel array.
- Orientation error:** the angle between the target and the induced E-field directions.
- Longitudinal and Transverse Focalities:** the orthogonal distances along the area S_0 in which the E-field intensity is higher than 75% of the maximum E-field. The *Longitudinal* and *Transverse focalities* were then selected as the first and second largest distances on the S_0 using principal component analysis.
- Targeting Efficiency:** the E-field intensity on the target location.

Targeting efficiency and accuracy in multichannel arrays

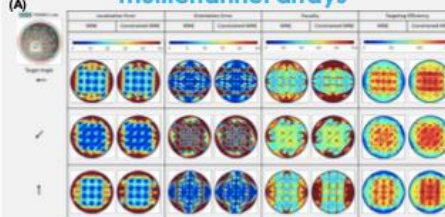
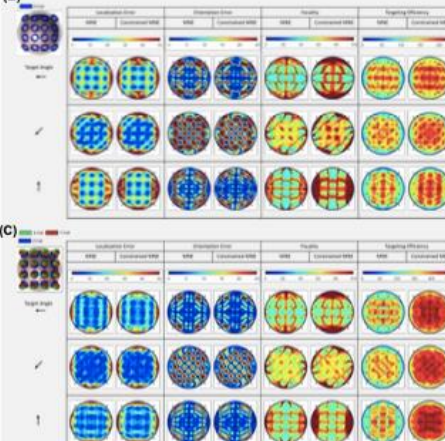


Fig.3. Evaluation of multichannel accuracy metrics for small vs large diameter coils (A,B) and the 3-axis coils array (C)



We can define a linear combination of all coils induced E-fields to replicate the desired target pattern on a surface area S by Minimum Norm Estimate (MNE) method.

The targeting efficiency and accuracy of the multichannel array depends on the coil geometry with smaller coils offering more accuracy at cost of reduced efficiency (A) and (B). The accuracy vs. efficiency trade-off can be resolved by using the three-axis coil elements² offering higher flexibility in E-field shaping while being more efficient than circular coils (C).

The three individual elements of the three axis coils (C) grant higher flexibility in E-field shaping while being more efficient than circular coils (here maximum E-field of 255 V/m was achieved). The localization error is significantly reduced as the X and Y elements additionally provide orthogonal fields to match the target. Moreover, combination of the X and Y elements lessens the orientation error by generating a 45-degree field at the center of Z element, lastly the fociality error of three axis coils array is reduced for the orthogonal target angle compared to the Z element array (B).

Coil movements error evaluation

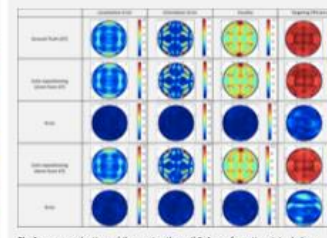


Fig.4. error evaluation while moving the coil 2-4 mm from its original place

Here we moved the coil 2 and 4mm with respect to the ground truth position and evaluated the accuracy metrics for these new coil positions (rows 2 and 4). The error values in comparison to ground truth are shown in rows 3 and 5. The results show that 2-4 mm coil movements led to small overall errors in the E-field pattern (3% - 6%).

The spatial accuracy is defined as the distance between the measured and true locations. The spatial accuracy of the neuronavigation system relies on several factors such as:

- The method used for optical tracking of the coils and the head
- Subject's head movement during the stimulation
- Any unwanted coil movements
- The characteristics of the tissue on which the E-field is calculated
- The registration accuracy of the subject's head to the MR data.

Fast multichannel TMS array targeting and navigation

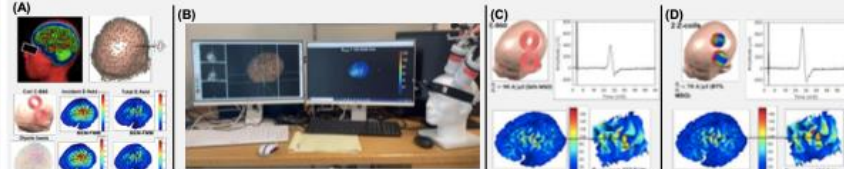


Fig. 5. (A) Top panel: Anatomically realistic high-resolution head model generated from individualized MRI data (left) and a set of basis functions comprising of three orthogonal dipoles at each location (right). Bottom panel: Comparison of the electric field (E-field) distribution obtained from the global basis function set defining the Magnetic Stimulation Profile (MSP) of the subject using the BEM-FM solver as the ground truth. (B) Real-time E-field guided neuronavigation of a physical 2x3 TMS coil array using a phantom. (C) Top panel: The commercial C-B60 coil (MagVenture, Denmark) used to determine intensity 105% of resting Motor Threshold (MT) in a neuroimaging experiment with coil position and a suprathreshold electromyographic (EMG) responses (right). Bottom panel: Distribution of the cortical E-field intensity estimated by using anatomically realistic head modeling approach (left) with a zoomed-in view of the 'hot spot' at the motor cortex. (D) Corresponding information for the 3-axis coils when two Z-elements are driven as a figure-of-eight coil.

Our computational multichannel TMS neuronavigation system allowed rendering the E-fields of individual 3-axis coils and synthesizing the 'hot spot' using the array approach with speed and accuracy suitable for human studies.

- Fast computational E-field modeling (A):** By using individual head modeling in conjunction with a global three-axis dipole basis set the intracranial E-fields of an arbitrary moving TMS coil can be rapidly approximated in less than 100 msec. The fundamental dipole basis set solution obtained by the BEM-FMM method is called the **Magnetic Stimulation Profile (MSP)** as it needs to be computed only once and it fully characterizes TMS-induced E-fields of the subject³.
- E-field guided real-time neuronavigation for 3-axis coil array (B):** The MSP approach can be interfaced with a commercial neuronavigator (Locality, Germany) to perform E-field guided real-time neuronavigation with TMS coil arrays.
- Comparison of intracranial E-field distributions of two coils (C and D):** Commercially available figure-of-eight coil (C-B60, MagVenture, Denmark) vs. two Z-elements driven as a figure-of-eight coil. Suprathreshold activations were obtained by both coil types. Differences in coil inductance cause the stimulator output and current rate-of-change values to be different.. The estimated cortical E-field intensities at motor cortex agree within 10% between the two coils and shows the validity of the computational navigation system for multichannel TMS with 3-axis coils.

Discussion

We showed that the multichannel TMS array approach can be used for steering the target area for accurate and efficient stimulation with interactive fast E-field computation and visualization. In future, we aim to utilize the MSP based method for nTMS motor mapping by stimulating the subject with multiple coil positions /intensities and computing the correlation metrics between the E-fields and the EMG responses.

References: 1. Ruohonen, J., and R. J. Ilmoniemi, "Focusing and targeting of magnetic brain stimulation using multiple coils," *Medical and Biological Engineering and Computing* 36.3 (1998): 297-301. 2. de Lara, Lucia I. Navarro, et al. "A 3-axis coil design for multichannel TMS arrays." *Neuroimage* 224 (2021): 117355. 3. Daneshzand, Mohammad, et al. "Rapid computation of TMS-induced E-fields using a dipole-based magnetic stimulation profile approach." *Neuroimage* 237 (2021): 118097.

Funding: R01EB0215445, R01MH111829, P41EB030006, R21MH116484, and SRO2NS104585 and the Rapaport Foundation.

Special thanks: Locality (M. Blublat), and Worcester Polytechnic Institute (S. Makarov & W. Wartman)

Continuous Monitoring of Cerebral Oxygen Perfusion for Intraventricular Hemorrhage Detection via Diffuse Correlation Spectroscopy in Extremely Premature Infants

Alyssa Martin¹, John Sunwoo¹, Alexander I. Zavriev¹, Kultu Kaya¹, Zachary Starkweather¹,
Tina Steele², Deborah Cudyer², Terrie Inder²,
Maria Angela Franceschini¹ and Mohamed El-Dib¹

¹Athinoula A. Martinos Center for Biomedical Imaging, Massachusetts General Hospital, Harvard Medical School, Charlestown, MA, USA.
²Department of Pediatric Newborn Medicine, Brigham and Women's Hospital, Harvard Medical School, Boston, MA, USA.



amartin46@mgh.harvard.edu

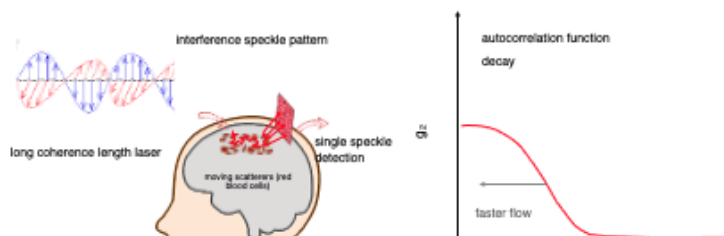
MOTIVATION

To date, there are no continuous, non-invasive monitoring devices that give an index of cerebral blood flow in Neonatal Intensive Care Units. Continuous, non-invasive monitoring of cerebral oxygen perfusion is imperative, as changes in cerebral blood flow may result in Intraventricular Hemorrhage (IVH). In this study, we hypothesized that continuous monitoring of cerebral oxygen perfusion via Diffuse Correlation Spectroscopy in extremely low gestational age (ELGA) infants (defined as < 29 weeks gestational age), monitored for the first few days of life, provides a method to potentially predict and determine the occurrence of IVH.

DIFFUSE CORRELATION SPECTROSCOPY

Diffuse Correlation Spectroscopy (DCS) is based on the principle that as long coherent length light diffuses through the tissue; it has a distinct scattering pattern created by photons colliding with dynamic red blood cells.

- Light is detected at a short (5 mm) and a long separation (20 mm) by very sensitive photon counting detectors
- A graphical user interface developed in-house estimates the autocorrelation of the temporal intensity fluctuations in real-time.
- The decay of this autocorrelation function is proportional to an index of the blood flow to the skin (short separation detector) and brain (long separation detector).



OPTICAL PROBE



CEREBRAL AUTOREGULATION

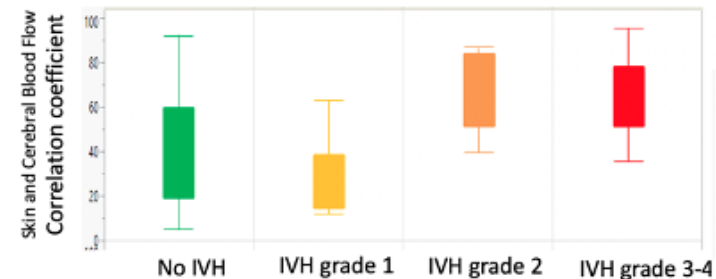
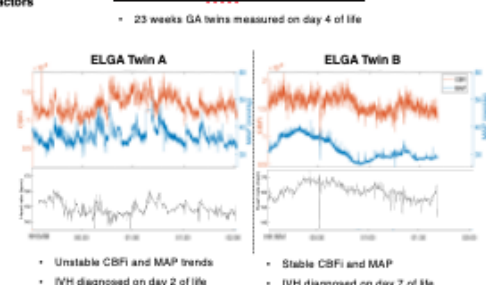
This study is ongoing at the Brigham and Women's Hospital Neonatal Intensive Care Unit

- 21 ELGA infants were continuously monitored using an optical probe connected to a DCS device, in 6-8-hour periods for three consecutive days.
- Quantified cerebral autoregulation by cross-correlating the blood flow to the skin with the blood flow to the brain and compared the results in different infant groups by IVH grades ranging from 0 (no IVH) - 4 (severe intraparenchymal extension).

Correlation between skin and cerebral blood flow, IVH Grade, and other factors that could affect cerebral autoregulation in twin ELGA infants A and B

Indices	A	B
Correlation between skin and cerebral blood flow (%)	87	26
Day of life diagnosed with IVH	2	7
Final IVH grade	2	2
Caffeine	Yes	Yes
Dopamine	No	Yes
Morphine	No	Yes
HCT	42.2	39.7
PDA	Yes	Yes
APGAR 1 min	5	5
APGAR 5 mins	7	6
Birthweight (g)	560	585

Two hours of CBFI in relation to MAP



DISCUSSION AND FUTURE WORK

Preliminary results suggest that a high correlation between skin and cerebral blood flow are indicative of IVH onset. However, a few infants in the 0/ no IVH group also demonstrated an elevated correlation between skin and cerebral blood flow.

Further research is needed to rule out other factors that might affect this correlation, such as medications or treatments that modulate blood pressure, heart rate, blood viscosity, hematocrit, or conditions such as anemia, hypotension, hypocarbia, and patent ductus arteriosus¹.

Future work: At present, there are no treatments for IVH. However, the increase in diagnostic technology capable of detecting the blood flow instability precursor of IVH could lead to a research initiative to discover treatments that prevent or mitigate the severity of IVH.

¹Walsh, B.H., Inder, T.E., Volpe, J.J., 2017. Intraventricular Hemorrhage in the Neonate, in: Fetal and Neonatal Physiology. Elsevier, pp. 1333-1349.e6. <https://doi.org/10.1016/B978-0-323-35214-7.00134-72>.

Characterizing the effects of sex and vascular risk factors on cerebral hemodynamics in the oldest-old from the Human Connectome Project-Aging data

Ezgi Yetim Arsava, MD, Allison E. Lovely, BA; Randa Almaktoum, BSc; Kathryn M. Yochim, BA; David H. Salat, PhD; Meher R. Juttukonda, PhD
Brain Aging and Dementia Lab ,Athinoula A. Martinos Center for Biomedical Imaging, MGH, Charlestown, MA

Introduction

Previous studies using various imaging techniques have found evidence of decreased global cerebral perfusion with advancing age. On the other hand, cerebral hemodynamic aspects of successful aging within the oldest-old population still remain unclear. Arterial spin labeling (ASL) magnetic resonance imaging (MRI) is a popular approach for studying cerebral hemodynamics in normal aging as well as in a range of neuropsychiatric disorders. However, studying white matter hemodynamics with ASL is challenging due to longer arterial blood arrival times. In this study, we aimed to investigate the sex effect on ASL measured derived using a novel approach and evaluate its association with vascular risk factor profile in the oldest-old population from the Human Connectome Project-Aging (HCP-A).

Methods

Typically aging adults (n=48) older than 80 years were enrolled as part of HCP-A. A novel cross-correlation approach was used on the ASL data to calculate cerebral blood flow (CBF) and arterial transit times (ATT) in gray and white matter. Univariate and multivariate analyses were performed to determine the effect of sex and vascular risk factors on the age-dependent changes in cerebral hemodynamics.

Aging data

Results

The median (IQR) age of the population (25 female and 23 male) was 85 (82-87) years. Females had higher CBF (50 ± 10 vs. 42 ± 11 ml/100gr/min; $p=0.011$) primarily in the gray matter and shorter ATT measures in both the gray (1.58 ± 0.18 vs. 1.69 ± 0.19 sec; $p=0.045$) and white (1.77 ± 0.10 vs. 1.83 ± 0.09 sec; $p=0.052$) matter compartments.

Hypertension was the most common vascular risk factor (79.2%) followed by hyperlipidemia (60%) and diabetes (10%).

Nineteen percent of the population had at least one Apolipoprotein E (ApoE) e4 allele, which was closely associated with cerebral perfusion metrics; individuals harboring ApoE e4 allele had lower CBF and longer ATT in the gray and white matter.

The presence of hypertension was associated with longer ATT values in the gray and white matter while hyperlipidemia was related to lower CBF values. There was a trend for the number of vascular risk factors to be negatively correlated with CBF and positively correlated with ATT (Figure 1).

CBF gray matter

	yes	no	p
Age			r=0.007
Female	54.28 (47.13 - 60.25)	44.24 (39.3 - 53.4)	.008
Hypertension	48.45 (40.59 - 57.45)	49.52 (45.33 - 60.55)	.322
Diabetes Mellitus	57.21 (45.97 - 60.7)	47.41 (42.1 - 57.57)	.316
Hyperlipidemia	65.39 (59.7 - 55.75)	55.18 (47.1 - 61.34)	.026
Obesity	51.03 (45.3 - 55.35)	47.18 (41.74 - 59.05)	.575
APOE e4 allele	43.29 (40.5 - 50.05)	52.83 (44.16 - 60.05)	.001
Number of vascular risk factors			r=-.226
			.122

ATT gray matter

	yes	no	p
Age			r=.004
Female	1.44 (1.37 - 1.56)	1.6 (1.46 - 1.75)	.005
Hypertension	1.56 (1.4 - 1.7)	1.43 (1.38 - 1.48)	.022
Diabetes Mellitus	1.32 (1.3 - 1.57)	1.5 (1.4 - 1.68)	.125
Hyperlipidemia	1.51 (1.4 - 1.68)	1.48 (1.37 - 1.61)	.495
Obesity	1.54 (1.38 - 1.65)	1.5 (1.39 - 1.68)	.550
APOE e4 allele	1.6 (1.52 - 1.67)	1.48 (1.37 - 1.68)	.104
Number of vascular risk factors			r=.169
			.251

CBF White matter

	yes	no	p
Age			r=-.088
Female	23.35 (22.37 - 25.36)	21.68 (20.01 - 25.58)	.078
Hypertension	23.56 (20.82 - 25.52)	25.7 (23.7 - 26.9)	.110
Diabetes Mellitus	23.5 (21.29 - 27.7)	23.67 (21.23 - 23.9)	.387
Hyperlipidemia	23.69 (20.76 - 25.53)	23.86 (22.83 - 28.61)	.696
Obesity	24.09 (22.41 - 25.13)	23.63 (21.1 - 26.49)	.501
APOE e4 allele	23.18 (19.51 - 26.21)	23.67 (21.27 - 25.9)	.335
Number of vascular risk factors			r=-.270
			.064

ATT white matter

	yes	no	p
Age			r=.028
Female	1.76 (1.69 - 1.82)	1.88 (1.74 - 1.93)	.019
Hypertension	1.83 (1.73 - 1.92)	1.75 (1.68 - 1.77)	.016
Diabetes Mellitus	1.78 (1.72 - 1.88)	1.8 (1.72 - 1.9)	.306
Hyperlipidemia	1.81 (1.79 - 1.93)	1.78 (1.71 - 1.87)	.548
Obesity	1.84 (1.76 - 1.89)	1.78 (1.7 - 1.81)	.493
APOE e4 allele	1.93 (1.87 - 1.94)	1.76 (1.7 - 1.87)	.006
Number of vascular risk factors			r=.270
			.064

Table 1.

Bivariate relationships of cerebral hemodynamic parameters and demographic features and vascular risk factors

Discussion

This study shows a sex effect on CBF and ATT of the cerebral gray matter in the oldest-old, while hypertension has an age-independent significant impact on ATT values in both gray and white matter.

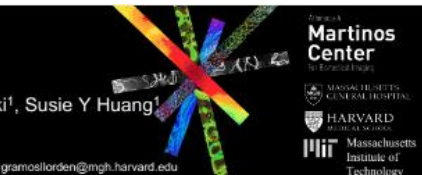
Ex-vivo whole human brain high b-value diffusion MRI at 550 micron isotropic resolution using a 3T Connectom scanner

Gabriel Ramos Llorden¹, Chiara Maffei¹, Qiyuan Tian¹, Alina Scholz³, Berkin Bilgic¹, Jean Augustinack¹, Thomas Witzel², Boris Keil³, Anastasia Yendiki¹, Susie Y Huang¹

¹ Athinoula A. Martinos Center for Biomedical Imaging, Massachusetts General Hospital, Massachusetts General Hospital, Harvard Medical School, Boston, MA, United States

² Q Bio Inc, San Carlos, CA, United States

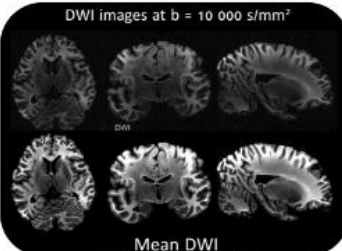
³ Institute for Medical Physics and Radiation Protection, TH Mittelhessen – Univ. of Applied Sciences, Germany



Introduction

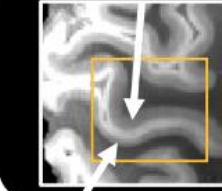
Diffusion MRI (dMRI) holds the most promise among noninvasive imaging methods for probing cellular structure in the human brain.

Multi-scale validation is key
Using *in vivo* and **ex vivo** diffusion MRI of human brain tissue and comparing against measurements at finer scales with micro CT and serial EM.



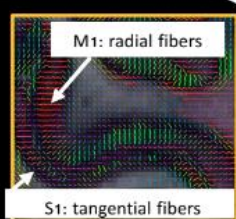
Axial, coronal, and sagittal slices of 550-micron DWI volume at $b = 10\ 000\ \text{s/mm}^2$

Primary Motor cortex (M1)

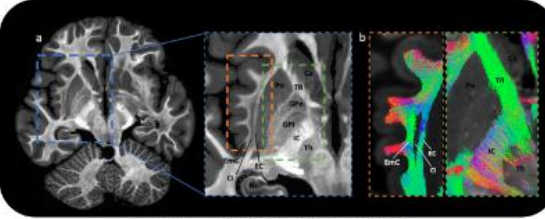


Anisotropic diffusion in M1/S1 cortex

Results



S1: tangential fibers



a) Mean Kurtosis map
b) Probabilistic tractography EC and EmC (left)

thalamic connectivity (right). Ca: caudate.

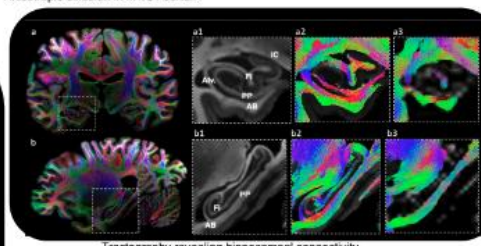
Cl: claustrum.

EC: external capsule.

Emc: extreme capsule. IC: internal capsule.

GPI/GPe: internal/external globus pallidus.

Th: thalamus. Pu: putamen. TR: thalamic radiation.

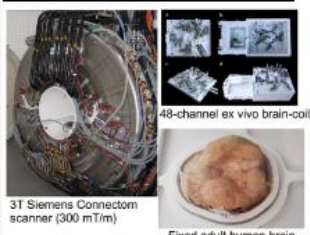


a-b) CSD-based directionally-encoded color maps showing coronal and sagittal views of the hippocampus.

a-b1,2,3: higher magnifications of the boxes shown in a-b. 1) CSD-based maps (0-th order SH) showing main hippocampal formation structures. 2) probabilistic tractography showing internal hippocampal connectivity. 3) lower spatial resolution data (downsampling factor = 3, 1.65 mm).

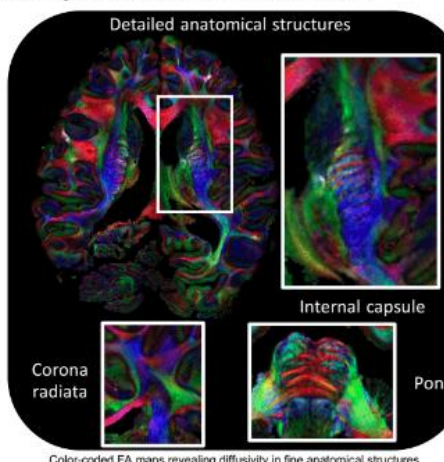
AB: angular bundle. Alv.: Alvear path. Fi: fimbria. IC: internal capsule. PP: perforant pathway.

Methods



3T Siemens Connectom scanner (300 mT/m)

Fixed adult human brain



Color-coded FA maps revealing diffusivity in fine anatomical structures

3T Connectom scanner

Ultra-high gradient strength

3D segmented EPI DW-spin echo sequence: High SNR, reduced geometric distortions

Conclusions

Future analysis with ex-vivo diffusion imaging will help bridge the gap between macroscale connectivity and **human brain microstructure** through comparison with micro-CT or electron microscopy.

Acknowledgements: NIH U01EB026996, R01NS119911, R01NS118187, R01EB021265, and P41EB030006.



Incidence and Cognitive Correlates of Strangulation in Intimate-Partner Violence

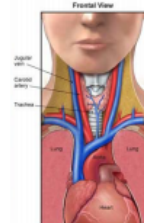
Annie-Lori Joseph¹, Nathalia Quiroz², Julia Daugherty⁴, Olivia Scott⁵, Howard Berenbaum⁶, Eve Valera^{1,3}

¹Department of Psychiatry, Massachusetts General Hospital, Boston, MA; ²Universidad del Norte, Colombia; ³Department of Psychiatry, Harvard Medical School, Boston, MA; ⁴Universidad de Granada, Spain; ⁵Harvard College, Cambridge, MA; ⁶University of Illinois at Urbana Champaign, Urbana, IL



Introduction

- Intimate partner violence (IPV) is experienced by approximately 1 in 3 women globally.¹
- 80-90% of injuries reported due to IPV are to the neck and higher, and includes fatal and non-fatal strangulation (NFS).²
- Strangulation can cause an acquired brain injury if an alteration in consciousness (AIC; dizziness, feeling disoriented, "seeing stars or spots", losing consciousness, etc.) occurs.³
- Women who have experienced NFS by their partner have been shown to have a seven-fold increase of becoming homicide victims⁴.
- Rates of strangulation-induced AICs or related cognitive sequelae have not been previously evaluated in IPV.



Strangulation
A form of asphyxia from external pressure placed upon the neck, obstructing: 1) blood flow either from or to the brain, and/or 2) the airway

Methods

Participants

- 99 women who reported experiencing at least 1 physically abusive incident from a past or current partner
- 53 women were included for cognitive analyses after exclusion criteria (e.g. neurological disorders, psychiatric history, substance abuse, etc.)

Instruments



Brain Injury Severity Assessment (BISA)

- A semi-structured interview that examines history of any partner- or non-partner-related AICs. For example:
- "After anything that your partner has ever done to you, have you ever lost consciousness or blacked out?"
(If Yes) Can you please describe what happened?

Conflict Tactics Scale (CTS)

- Self-report measure of partner abuse severity
- Has your partner ever choked you?

California Verbal Learning Test (CVLT)

- Assessment of verbal learning and memory

Analyses



- Analyses of variance (ANOVA) and analyses of covariance (ANCOVA) were performed.

Results

Demographic characteristics

	M	SD
Age	32.0	9.3
Year of education	12.3	2.1
Race (%)		
Caucasian	59	
African American	34	
Other	7	
Employment status	51	
Residing in a shelter	69	

1) Rates of strangulation are high, but depend on how strangulation is assessed.

CTS Item

"Did your partner ever choke you?"

82% report at least 1 event

22% reported more than 25 events

BISA Interview

"After anything your partner ever did to you did you ever lose consciousness, feel dizzy, feel dazed/confused, etc.?"

25% reported at least 1 strangulation

12% reported repetitive strangulations

2) Number of strangulation-induced AICs was associated with a woman's ability to learn a list of words that were read to her five times.

- This association was not accounted for by other brain injuries the woman may have sustained via her abuse

Discussion

- This is the first report to assess strangulation in this manner and demonstrate a link to cognitive functioning.
- These data contribute to our knowledge of the prevalence of non-fatal strangulation and the cognitive effects in women who have experienced IPV.

References

- Black, M., et al. *The National Intimate Partner and Sexual Violence Survey (NISVS): 2010 Summary Report*. C.I.D.C.a.P. National Center for Injury Prevention and Control, Editor. 2011: Atlanta, GA.
- Wu, V., H. Huff, and M. Bhandari, Patterns of physical injury associated with intimate partner violence in women presenting to the emergency department: a systematic review and meta-analysis. *Trauma Violence Abuse*, 2010. 11(1-2): p. 71-89.
- Vilay, E., and A. Sayay, A. (2017). Brain injury in women experiencing intimate partner violence: neural mechanistic evidence of an "invisible" trauma. *Brain Imaging and Behavior*, 11(6), 1664-1677. <https://doi.org/10.1007/s11682-016-9643-1>
- Glass, N., Campbell, J., Mansoor, G., Talaliferro, E. (2008) Non-fatal strangulation is an important risk factor for homicide of women. *Journal of Emergency Medicine*, 35(3); 329-335.